Titan's Anomalous Atmosphere from Top to Turf

Erin Elise Flowers

A Dissertation
Presented to the Faculty
of Princeton University
in Candidacy for the Degree
of Doctor of Philosophy

Recommended for Acceptance
by the Department of
Astrophysical Sciences
Adviser: Professor Christopher F. Chyba

April 2023

Abstract

Titan, Saturn's largest moon, is the only moon with a substantial atmosphere. Its primary constituents are 94.2% N_2, 5.65% CH_4, 0.1% H_2, and smaller amounts of nitriles, hydrocarbons, and other organics. Though there had been several flybys and ground-based observations of Titan since its discovery in 1659, the Cassini-Huygens mission revealed a world unlike any other. Titan is the only place in the solar system, other than the Earth, to have stable liquid on its surface. Instead of water, Titan has methane lakes and seas, and a methane cycle analogous to the Earth's water cycle. The Cassini-Huygens mission also revealed many interesting phenomena, such as a spectacular detached haze layer, superrotating jets, a large dune desert, and more. Since the finale of the Cassini-Huygens mission, there have been many initiatives to try to understand the mechanisms behind the dynamic and chemical processes taking place on Titan using a combination of computational and observational methods. In recent years there has been an intensification of these efforts as the NASA Dragonfly mission prepares to embark.

This thesis is an exploration of Titan's atmosphere, from the thermopause at roughly 1400 km to the surface. I combine a variety of computational techniques with observational input to model various dynamic and chemical processes with the goal of furthering the field's understanding of Titan. I present results from four studies, starting with particle-atmosphere interactions and finishing with troposphere-surface interactions. I also include a review on the current Titan General Circulation models (of which there are very few) to summarize the current computational state of the field, highlighting successes, and discussing the many areas that require improvement, before describing the GCM that I work with and the improvements I have made. To conclude, I summarize each chapter and discuss a few future projects that are currently or soon to be in progress.

Acknowledgements

WHEW!! It's been 23 years, 4 states, and 2 countries of schooling, but I'm finally DONE. Before you ask, I'm drinking a Last Word as I write this. Seemed apt.

First and foremost I must thank my family: to my parents for all the time, energy, and effort they put into my education. Who knew all those hours forcing me to learn to read as a toddler would result in a lifelong love of learning and sci-fi? I didn't get all the toys I wanted growing up, but I definitely got all the books I wanted, which I think is the better deal. I couldn't be where I am today without you two teaching me how to live, learn, and love, and I look up to you both above all others. There are people in the world I love with all my heart, but you *are* my heart. "Thank you" doesn't begin capture the sentiment.

To my brother Ian, who always asked me questions and was one of the first people to make me feel smart, and who as we got older has become a pretty chill dude I can rely on. Let's keep on vibin'. To my grandmothers, who cared for me, drove me around to all the after-school activities, watched me in the summers, and made sure I never stopped learning, even on vacation. One day I'll write that book Gran'ma Gloria, and Gran'ma Miriam, if anyone could figure out how to become a ghost, it would be you, so if someone feels a cold spot in the auditorium during my defense... To Gran'pa who definitely is one of my biggest fans and who always makes sure that my successes go celebrated. Make sure you put "Dr." in front of my name when you text and call everyone! And to my many aunts, uncles, and cousins who have showered me with love and support over the years - I could've been born into any family, but I'm so glad it was ours. Thank you, thank you, thank you.

To Erica and Kimmie, my very oldest, bestest friends. Who knew that we could be so lucky, that 17 years after I switched on the second day of 6th grade from choir to band that we would still be spending hours and hours on the regular talking about books and shows and politics and philosophy and goofy shit. I love you both with all of my heart, and I know my life would be much, much worse without you both in it. ... Does this mean I'm finally pickled?

To Alé and Amari - I think every phase of life you should be part of a trio, and I'm so glad we found ours during our 20s! OG Mardi Gras forever. Y'all are my ride or dies, you know that right? I am in awe of your successes and how you both bring your authentic self to everything you do, and you both inspire me endlessly to be a better woman. I hope that when we're old and rich and crusty we're still having bougie food adventures and drinking box wine on a weeknight together.

To Goni and Mackenzie and Lachlan and Brianna and Erin and Zack and Vassilis and Luke and Kris and Amy and Roohi and Sam and Rodrigo - y'all are so dope!! Goni, you know you're the dopest so I'm gonna save you for last, but I'm going to thank all of my friends in the astrophysics department in my cohort plus/minus a year because you made this whole PhD thing fun and bearable. Thank you for sharing your knowledge and expertise over the years, for being the best office mates (for like 5 years Lachlan and Vassilis!), for indulging my love of DnD (I *swear* we will finish the campaign), for watching Ciaran and Sophie and Mavis, for all that you do to make

the department better simply by existing and caring - seriously, if I had to go back and choose a grad school all over again, I would choose to be wherever you guys are.

Goni - I don't think there's anyone else in the world I admire as much as I do you. You astound me with the poetry of your grace. Your thoughtfulness in all that you do and the relish you take in life's simple pleasures is an inspiration to all that your light falls upon. You inspire me to be a better person in all ways - in my relationships with others, in my work, and in my spirit. I love you with all my heart, and thank you so much for being my friend.

To the many, many friends I have had the fortune and honor of collecting over the years, thank you! You kept my life fun, showed me new horizons, and challenged my thinking in exciting and thoughtful ways.

To the Access, Divesity and Inclusion team and the Prison Teaching Initiative - especially all of the folks I've fellowed with over the years - thank you for being so much fun and helping me to grow in ways I wouldn't have otherwise. I hope that what we've done together continues to grow and improve the lives of other graduate students and justice-impacted students in New Jersey.

To all of the teachers and professors and mentors I've had along the way, thank you for always supporting and believing in my intellect, and for never treating me as your token Black girl.

To Chris, my biggest cheerleader and advocate at Princeton. I'm pretty sure I hit the lottery with advisors. I'll fight anyone who says they have a better one. Or maybe just take all of their coffee. You always have treated me as a colleague and a human, never as a subordinate. I can't put into words how much I appreciate all that you do, for me, for the department, for the university, and for the world.

And finally to Adam. Where to begin? You are all that is bright and beautiful. Loving you has been the easiest, most joyful part of my life. You are hands-down my biggest cheerleader, and you have been since the moment we met. I cherish your intellect, your curiosity, your creativity, your intense love of art and food and music and cocktails and learning and books, and *especially* your love for me and your friends and family. You have the biggest heart of anyone I know, and how lucky am I to be in it? Thank you, with all of my heart and soul, for making sure that at the end of every long, frustrating day of "sciencing", I go to sleep laughing.

To my family and friends, who didn't always understand what I was doing or why I was doing it, but who still enthusiastically talked about space with me.

Contents

List of Tables

List of Figures

Chapter 1

Introduction

1.1 Welcome to Titan

Saturn's moon Titan is a fascinating and unique celestial body - the most interesting body in the solar system. With a diameter of 5150 kilometers, it is the second largest moon in the solar system (after Jupiter's moon Ganymede) and is larger than the planet Mercury. It is also the only moon with a thick atmosphere, which is composed primarily of nitrogen and methane, and stable surface liquid reservoirs. One of the most interesting aspects of Titan is the presence of stable bodies of liquid on its surface. These include methane and ethane lakes and seas, which are similar to Earth's oceans, lakes, seas, etc, making it the only celestial body in our solar system other than Earth known to have stable liquid reservoirs. Titan is of great scientific interest because its atmosphere and liquid reservoirs may provide clues about the early Earth's atmosphere and the conditions that led to the development of life on our planet. The existence of an atmosphere and liquid bodies on Titan suggests that there may be the potential for some form of life to exist on the moon. While it is unlikely that life as we know it could exist on Titan due to the extreme cold temperatures and the lack of liquid water, it is possible that other forms of life could exist that are adapted to the unique conditions on the moon.

Titan was discovered by Christiaan Huygens on March 25, 1655. Huygens was a Dutch mathematician, astronomer, and inventor, who improved design of Galileo's telescope so that it might resolve more distant objects. His improvements included increasing the focal length of the telescope, and there was an era in the 17th and 18th centuries of the very long tubed telescope, although eventually (after the discovery of Titan) Huygens and his brother Constantijn eventually invented a tubeless "aerial" telescope that connected the eyepiece and objective lens using a taught string (Huygens, 1684). With the improved telescope, Huygens was able to resolve Saturn's rings for the first time, and while studying the rings he noticed a "little star" whose motions he catalogued over the course of a couple weeks. He determined that it must be a moon in orbit around Saturn, and initially called it *Saturni Luna* ("Moon of Saturn"). He determined the moon's orbital period of about 16 days, and he published his observations in *Systema Saturnium* (see Figure 1.1) (Huygens, 1659). Huygens's

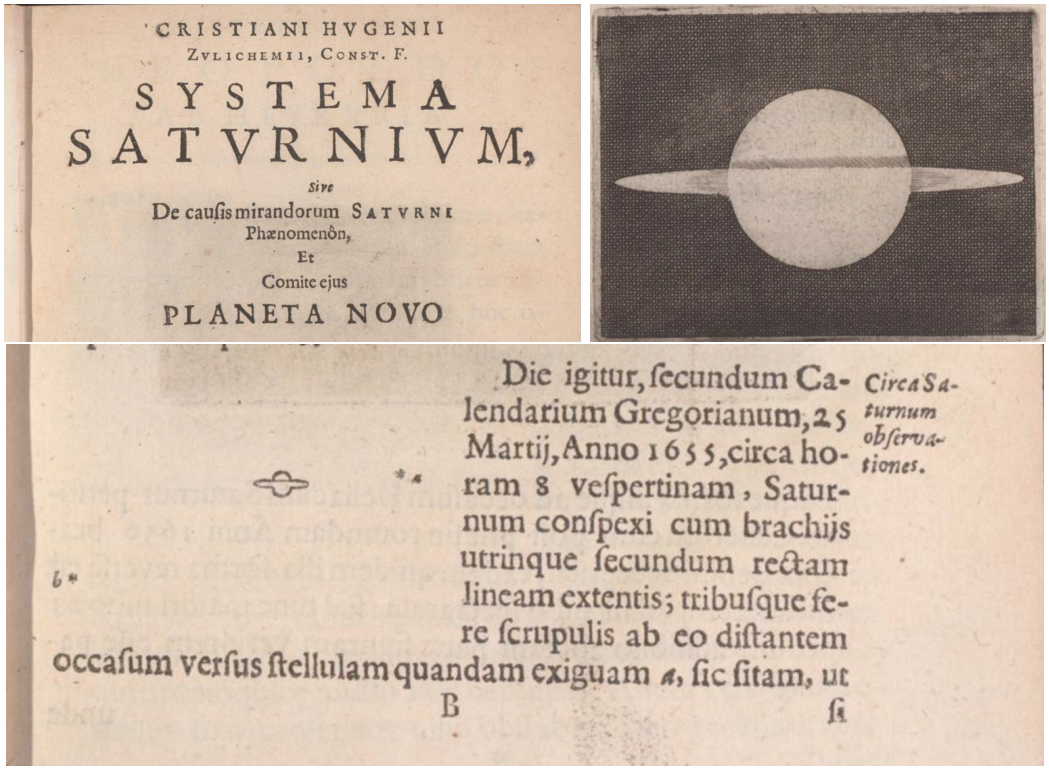

Figure 1.1: Top: Title page (left) and drawing of Saturn (right) from *Systema Saturnium*, Huygens's publication on his observations of Saturn. Bottom: Entry detailing the discovery and observation of Titan, a "stellulam quandum" or "little star" denoted "a" in the drawing, from Huygens's *Systema Saturnium* (Huygens, 1659).

findings only reinforced what Galileo's observations of Jupiter's moons confirmed - that the Earth is not the center of the universe, and the planets in our solar system host complex systems of their own.

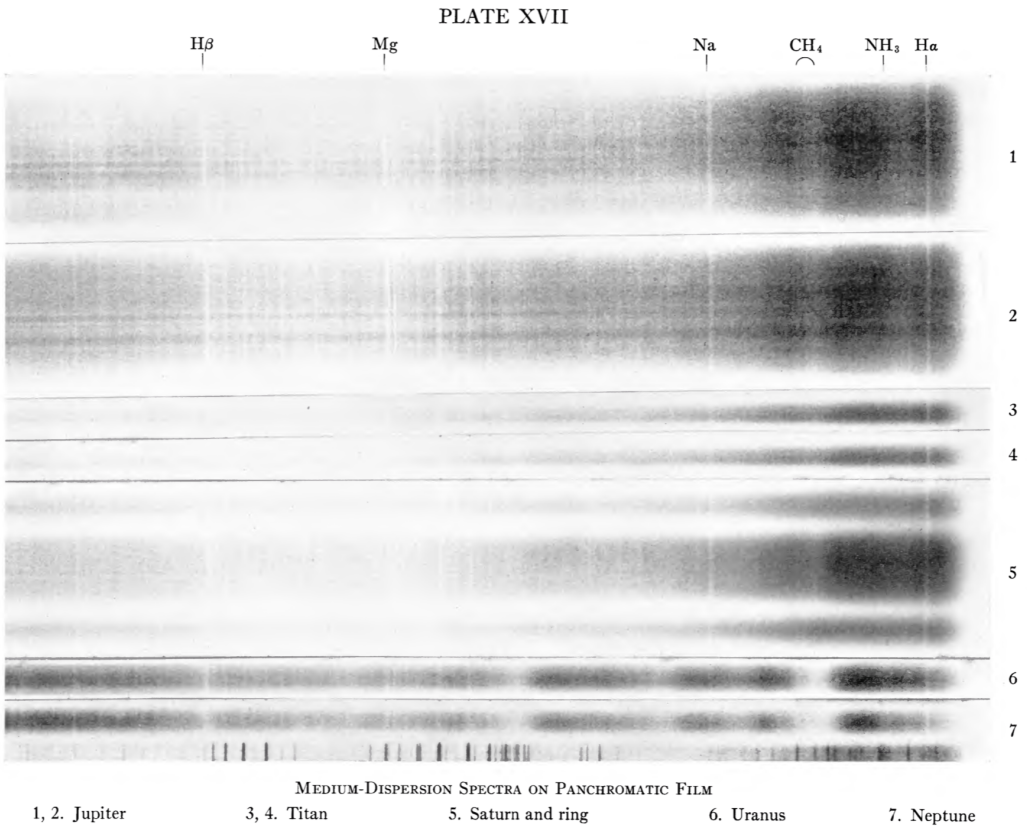

Figure 1.2: Kuiper's observations of the gas giants and Titan (rows 3 and 4 in the image). The bands that correspond to Hα, Hβ, magnesium, sodium, methane, and NH_2 are marked along the top. Looking closely at the Titan spectra, one can see bands for methane present in Kuiper's observations (Kuiper, 1944).

After its discovery, Gerard Kuiper made the next important finding when he detected an atmosphere around Titan in 1944. When observing the outer gas giants at McDonald Observatory the winter of 1943-1944, Kuiper also took spectra of the largest moons in each system. He was surprised to find bands of methane when he observed Titan (see Figure 1.2) , writing "The presence of gases rich in hydrogen atoms on a small body like Titan is surprising and indicates that the atmosphere was formed after Titan had cooled off" (Kuiper, 1944).

Over the course of the next several decades, there would be ground-based and space-based observations of Titan, though there would not be a dedicated mission to the Saturnian system until the 21st century. Most notable were the Pioneer and Voyager flybys. These two missions collected some of the earliest data on Titan's atmosphere after the initial discovery in 1944. Pioneer 11, launched in 1973, had the task of surveying the asteroid belt, Jupiter, and Saturn. It was the first spacecraft to ever study Saturn when it reached it in 1979. Voyager I and II were already en route to Saturn, and so Pioneer 11's flyby was considered a "test route" for the two probes. At closest approach, Pioneer 11 was roughly 360,000 km from Titan. It was able to measure a surface temperature for Titan (84 $\pm$ 2 K), the Bond albedo (A

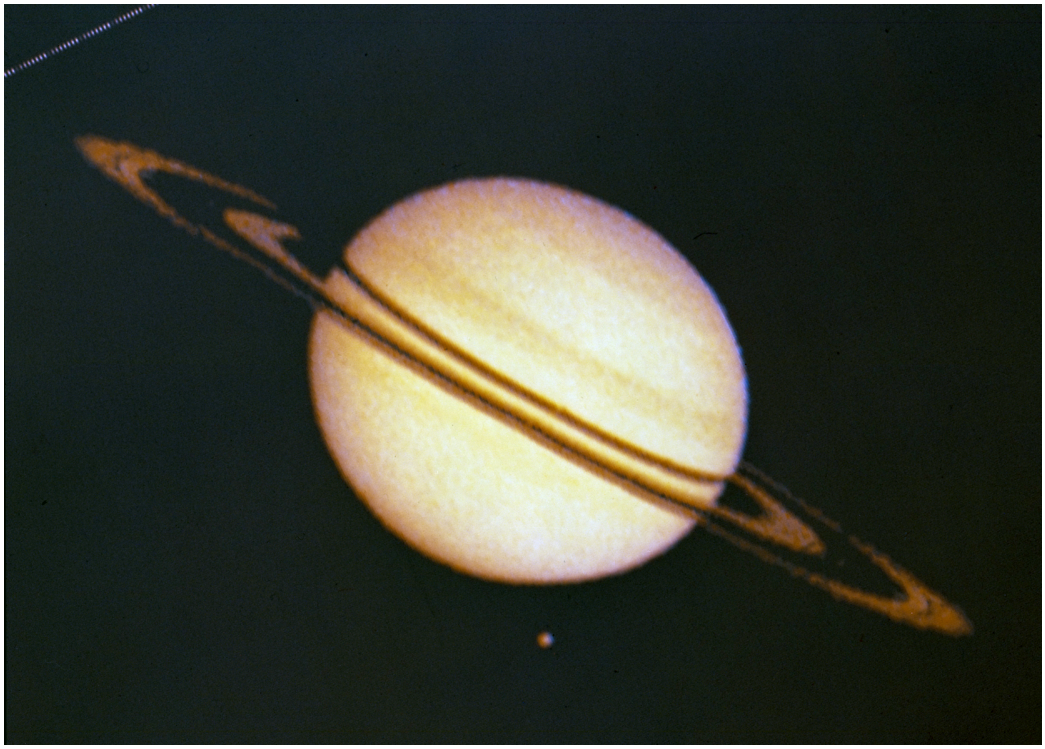

Figure 1.3: Pioneer 11's image of Saturn and Titan. Source: NASA Ames

≈ 0.21), and the major chemical components of Titan's atmosphere after N_2 (CH_4, C_2H_6, C_2H_4, and C_2H_2) (Tomasko, 1980; Trafton, 1981). After the flyby there were still many unknowns, such as the composition and distribution of the aerosols present in the atmosphere, the thermal structure, and seasonal variations.

The Voyager mission that soon followed would take measurements addressing many of these open questions. Launched in 1977, Voyager I and II studied Jupiter, Saturn, Uranus, Neptune, and the outer solar system, and they continue to send back data from interstellar space as of this writing. Their primary mission was to study the space environment, atmospheres, and satellites of the gas giants, as well as to study the conditions of the edge of the solar system and beyond. At closest approach, Voyager I was nearly 6500 km and Voyager II was nearly 666,000 km from Titan. The flybys confirmed that the bulk of Titan's atmosphere was made of N_2, which was first suggested to be the case in 1971 (Lewis, 1971), and spectra of the atmosphere confirmed the presence of many hydrocarbons (e.g. Hanel et al. (1981); Kunde et al. (1981); Maguire et al. (1981)). They also were able to measure a temperature-pressure profile (updating the surface temperature measurement to 93 K) (Lindal et al., 1983), average density and solid radius (Smith, 1980), and the presence of a polar hood and an asymmetry in the haze (Smith et al., 1981, 1982). In Figure 1.4, the asymmetry in the haze's brightness can be clearly seen in images from both Voyager I and II, while the polar hood is more apparent in the image from Voyager II. As often happens, with this new knowledge came new questions, and it would take another mission to begin answering them.

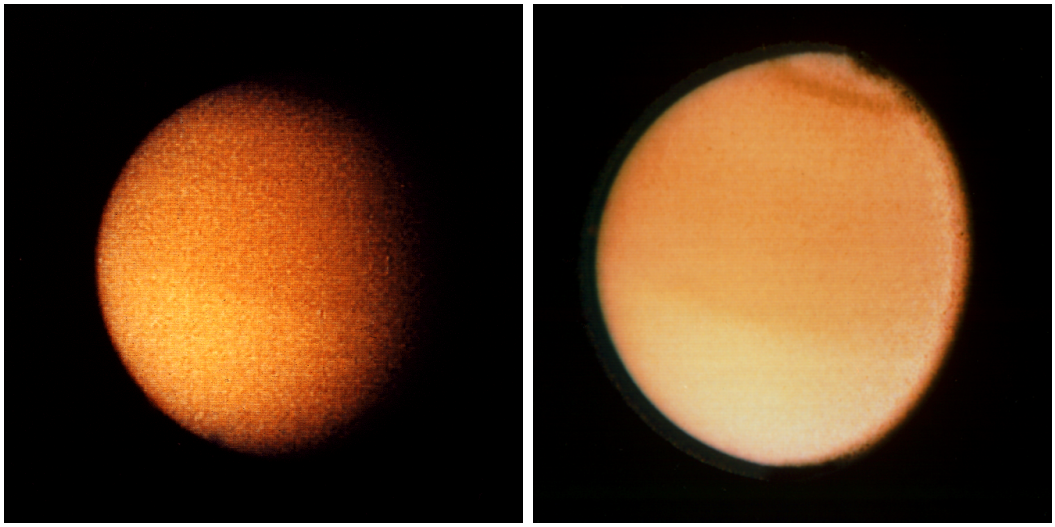

Figure 1.4: Images of Titan from Voyager 1 (left) and Voyager 2 (right) (Smith et al., 1981, 1982). Source: NASA GSFC

1.2 The Cassini-Huygens Mission

Although Titan has been observed by several space missions, the Cassini-Huygens mission was the only dedicated, in situ craft to study Saturn and its moons. A joint venture between NASA, the European Space Agency, and the Italian Space Agency, Cassini-Huygens was launched in 1997, arrived at Saturn in 2004, and the mission ended in 2017. It comprised the Cassini orbiter and the Huygens lander, the first and so far only man-made object to land on an outer solar system body. The goals of the mission, relevant to Titan, were (from the "Final Mission Report" (Cassini Collaboration, 2019)):

1. Interdisciplinary study of the atmospheres of Titan and Saturn
2. Interdisciplinary study of aeronomy in the Titan and Saturn atmospheres
3. Multispectral imaging of Saturn, Titan, rings, and the icy satellites to observe their properties
4. Radar imaging, altimetry, and passive radiometry of Titan's surface
5. In situ study of clouds and aerosols in the Titan atmosphere
6. Temperature and images of Titan's atmospheric aerosols and surface
7. Study of winds from their effect on the (Huygens) *Probe* during the Titan descent
8. In situ measurements of chemical composition of gases and aerosols in Titan's atmosphere

9. In situ study of Titan's atmospheric physical and electrical properties
10. Interdisciplinary study of Titan's atmosphere-surface interactions
11. Interdisciplinary study of Titan's chemistry and exobiology
12. Measurement of the physical properties of Titan's surface

There were also many other goals related to the Saturnian system's environment (such as measuring the particle distribution and extent of Saturn's magnetic field) that studied Titan's interaction with its surroundings. In order to achieve these goals, the orbiter and lander had a suite of instruments to take measurements of Titan's environment in orbit around Saturn, its atmosphere, and its surface. The instruments on Cassini include (also see Figure 1.5):

- Cassini Plasma Spectrometer (CAPS) (Young et al., 2004)
- Cosmic Dust Analyzer (CDA) (Srama et al., 2004)
- Composite Infrared Spectrometer (CIRS) (Flasar et al., 2004)
- Ion and Neutral Mass Spectrometer (INMS) (Waite et al., 2004)
- Imaging Science Subsystem (ISS) (Porco et al., 2004a)
- Dual Technique Magnetometer (MAG) (Dougherty et al., 2004)
- Magnetospheric Imaging Instrument (MIMI) (Krimigis et al., 2004b)
- Titan Radar Mapper (RADAR) (Elachi et al., 2004)
- Radio and Plasma Wave Spectrometer (RPWS) (Gurnett et al., 2004)
- Radio Science Subsystem (RSS) (Kliore et al., 2004)
- Ultraviolet Imaging Spectrograph (UVIS) (Esposito et al., 2004)
- Visible and Infrared Mapping Spectrometer (VIMS) (Brown et al., 2004)

And the instruments on Huygens include (also see Figure 1.6):

- Aerosol Collector Pyrolyser (ACP) (Israel et al., 2002)
- Descent Imager and Spectral Radiometer (DISR) (Tomasko et al., 2002)
- Doppler Wind Experiment (DWE) (Bird et al., 2002)
- Gas Chromatograph and Mass Spectrometer (GCMS) (Niemann et al., 2002)
- Huygens Atmospheric Structure Instrument (HASI) (Fulchignoni et al., 2002)
- Surface Science Package (SSP) (Zarnecki et al., 2002)

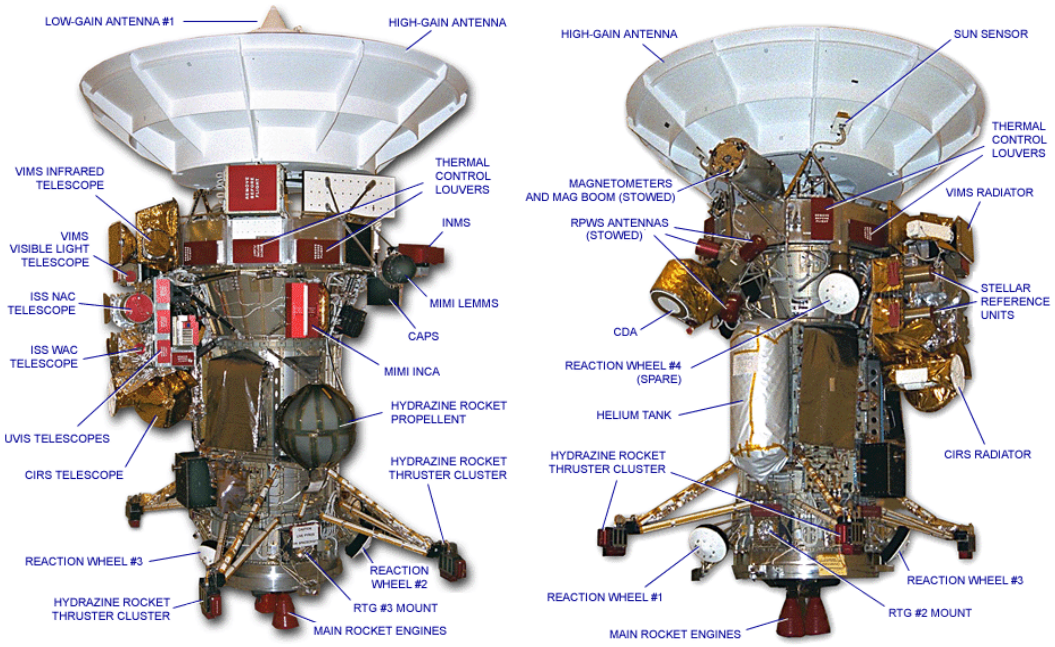

Figure 1.5: Schematic of the Cassini spacecraft and its instruments, from NASA Basics of Spaceflight Cassini page

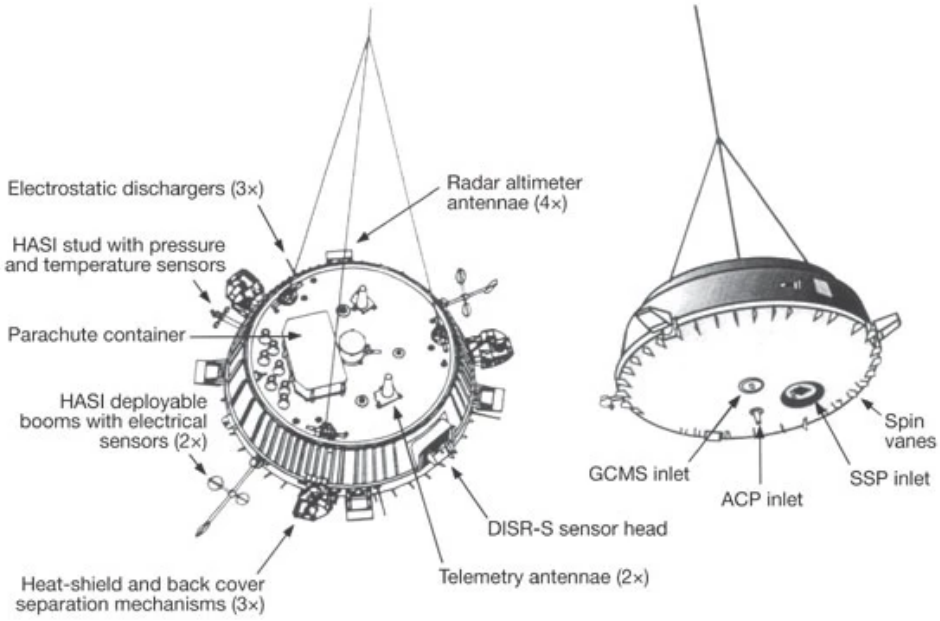

Figure 1.6: Schematic of the Huygens lander and its instruments. The Doppler Wind Experiment (DWE) is not pictured here, as it did not require direct access to or a direct field of view of the atmosphere. Instead, it comprised two ultra-stable oscillators within the probe.

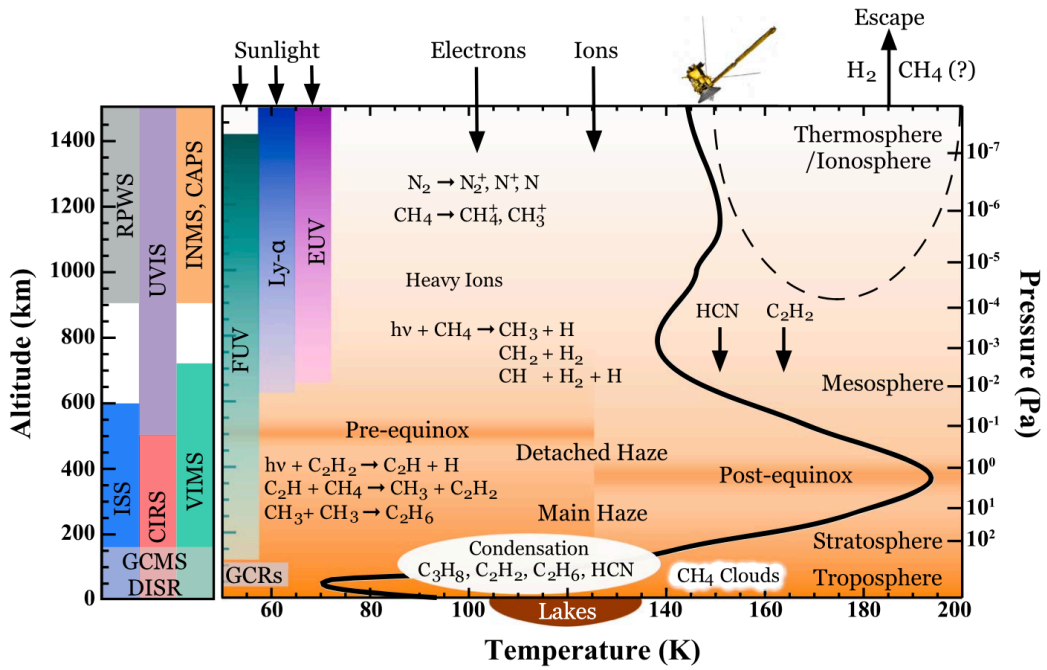

Figure 1.7: Titan's temperature-pressure profile, atmospheric layers, haze altitudes (pre- and post-equinox), and approximate locations of key chemical reactions with rough probe-depths of each of Cassini's instruments and penetration depths of solar radiation. Figure 1 from Hörst (2017).

This suite of instruments provided the best and so far only in-situ data we have to date, and over the course of my thesis I used data from many of them either as model inputs or comparison points. Figure 1.7 from Hörst (2017) is a summary of Titan's atmosphere (conditions pre- and post-equinox) and how the different instruments measured it. This thesis incorporates data from several instruments on the Cassini Orbiter and Huygens Lander, either as model inputs or comparison points for model output.

The Cassini-Huygens mission revealed a Titan we had not previously known. For a long time, Titan was a distant, hazy world that refused to give up its secrets, but the for the first time we had access to its surface. Cassini-Huygens was able to peer below the haze, and it discovered clouds, lakes, rivers - a whole methane cycle analogous to our water cycle! As I mentioned at the beginning of this introduction, the fact that Titan has liquid on its surface opens up a world of possibilities for habitability studies within our solar system. While the Cassini-Huygens mission answered many questions about Saturn's largest moon, it also revealed many anomalies that have yet to be fully explained. In the next two sections, I will briefly summarize some of the key findings from the Cassini-Huygens mission and the open questions they led to, split into the categories of "Chemistry" and "Dynamics."

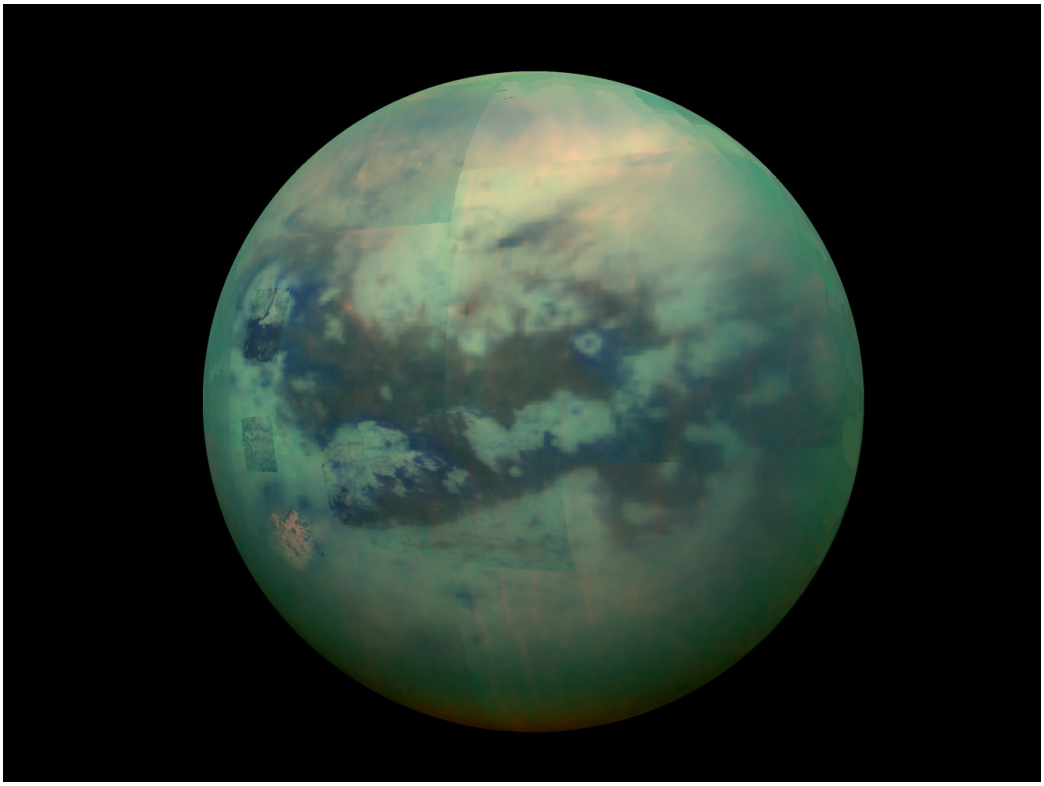

Figure 1.8: Composite image of Titan's surface taken with the VIMS instrument in false color.

1.3 Chemistry Discoveries & Questions

Previous flybys and ground-based observations of Titan provided preliminary measurements of the bulk atmospheric composition, so by the time Cassini reached Titan it was known that its atmosphere was primarily nitrogen and methane, with small amounts of hydrocarbons mixed in. Additional species were theorized to be present, the natural consequence of photochemistry with the known species, but they had not been detected yet. Cassini was able to constrain the methane abundance and profile (Niemann et al., 2005), as well as the abundances of several known molecular species (e.g. Cui et al. (2009); Coustenis et al. (2010); Koskinen et al. (2011)). It detected ^{36,40}Ar (Niemann et al., 2005) (suggesting interactions between the surface and atmosphere since these isotopes of argon are the product of outgassing rock), C_3H_6 (propene) (Nixon et al., 2013), several nitrogen-bearing species (Vuitton et al., 2007), and heavy ions (e.g. Coates et al. (2007); Waite et al. (2007); Crary et al. (2009)) for the very first time. These latter two discoveries were particularly exciting because they pointed to complex chemistry taking place in the atmosphere where nitrogen plays a starring role, while also opening up new questions about haze formation and composition on Titan.

One of the most outstanding questions about Titan is "what is replenishing the methane?" The full methane cycle was observed on Titan (rain (Turtle et al., 2009,

2011), cloud formation (Rodriguez et al., 2009), and collection in polar lakes and seas (Stofan et al., 2007; Turtle et al., 2011)), and this along with the measured profile from GCMS suggest a robust abundance of methane on Titan. The issue is, when taking the atmospheric escape rate of methane (which, granted, is not an entirely agreed upon value; see Yelle et al. (2008); Strobel (2008); Krasnopolsky (2009)) and the photodissociation rate of methane, Titan's methane would only last for order 10 million years (Yung et al., 1984a; Sotin et al., 2012). So are we only seeing a specific snapshot in time? Did Titan have a higher methane abundance in the past? Or is some unknown source replenishing it? How old is Titan's current atmosphere?

And what does Titan's methane abundance mean for its ethane abundance? Ethane was frustratingly not detected in lakes or seas in large amounts, even though it is a photochemical product of methane. Yung et al. (1984a) predicted that there should be sizable ethane lakes and seas, but Sotin et al. (2012) only detected hydrocarbon reservoirs that would account for roughly 75,000 years of photochemistry. It is possible that the ethane has sunk into the ground, pulled into clathrates (Mousis et al., 2016), but sampling of the ground near the lakes would be necessary to confirm or refute this hypothesis.

Beyond the smaller hydrocarbons, the identity and abundance of larger organic molecules in the hazes, lakes and seas, and on the surface remains to be determined. Large molecules were detected, but to know how and where they are formed, and the specific identities of many require additional study. The size and distribution of the haze particles (Tomasko et al., 2008; Courtin et al., 2015) and preliminary chemical composition determinations (Kim et al., 2011; Sim et al., 2013; Kim & Courtin, 2013) were measured, but much remains unknown about the evolution of haze particles. Related, how these large molecules evolve when they reach the surface is completely unknown. Given the fact that very little sunlight reaches the surface of Titan (only about 11%), it was difficult to chemically characterize the surface from orbit, and the SSP was not able to sample the ground (Tomasko et al., 2005). From the bulk density and DISR data, it is likely that the surface is covered in fine particles that are a combination of water ice and organic ices (e.g. Tomasko et al. (2005); McCord et al. (2006); Clark et al. (2010)), but a mission that can analyze samples would be necessary to definitively characterize the surface.

1.4 Dynamics Discoveries & Questions

The Cassini-Huygens mission allowed us to see through Titan's thick haze for the first time, and the length of the mission meant that Cassini was able to observe multiple seasons. It arrived in Titan's winter (October 2002 - August 2009) and observed all of the spring (like the Earth, Saturn is titled on its rotational axis [27° relative to the sun, and Titan orbits in this tilted plane] and thus experiences seasons). During this time, several bulk features exhibited seasonal variability. One such feature was a detached haze layer that Cassini observed for the first time (see Figure 1.9). The altitude of the detached haze layer dropped from 500 km in the winter to 380 km in the spring (West et al., 2011). The formation mechanism behind the detached haze layer

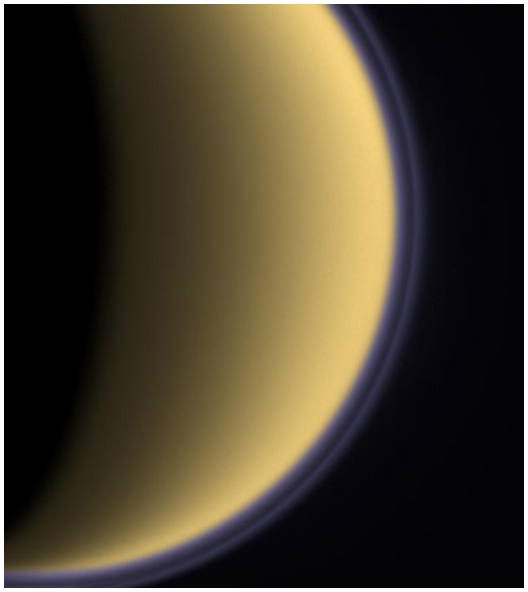

Figure 1.9: Titan's detached haze layer is a thin ring of bluish-purple around the main haze that is yellow in color. Source: NASA/JPL/Space Science Institute

is poorly understood, and the detached layer itself is not always present. A dynamic process is likely responsible for its variability, but what that process is is unknown. Other features of the main haze also were observed to have seasonal variability. The north-south asymmetry observed by Voyager (see Figure 1.4) appeared to flip in the time between the Voyager observations in the late '70s and Hubble observations in the '90s (Lorenz et al., 1997). The polar hood, also visible in Figure 1.4, is only present on the winter pole. It was seen on the north pole by Voyager, and it was observed to disappear from the south pole by Hubble (Lorenz et al., 2006a). In the case of the polar hood's variability, it is hypothesized that it is formed from haze particles being transported from the mid-latitudes and downwelling on the poles during winter months (Rannou et al., 2004a; Lorenz et al., 2006a).

Cassini-Huygens also observed stratospheric superrotating winds (Luz et al., 2006; Achterberg et al., 2008) that have also been observed from ground-based telescopes (e.g. Cordiner et al. (2020b)) moving at speeds as high as 200 km/s. It has been a challenge to reproduce these winds in computational models. Some models are able to generate superrotation at slower speeds (e.g. Newman et al. (2011)), others can reproduce the observed superrotation but not sustain it for long in the model (e.g. Newman et al. (2011); Lebonnois et al. (2012); Lora et al. (2015)), and others still do not reproduce it at all (Friedson et al., 2009; Larson et al., 2014). These winds are generated from a process where excess angular momentum is transported by eddies from the equatorial region and dumped into stratospheric zonal winds at higher latitudes. The growth of the superrotational jets depends on the mean meridional circulation, which in turn depends on a confluence of factors including solar radiation, Titan's rotation rate, and radiation transport. The radiation transport in particular

will depend on the haze and cloud physics. Coupling all of these factors in a realistic model to generate observed superrotation has proven extremely difficult.

The difficulties in creating realistic models only increase when we approach the surface. Since Cassini-Huygens was designed to study Titan's atmosphere, little is known about the surface. There are many features that are similar to the Earth's - rivers, lakes and seas that flow with methane instead of water (Stofan et al., 2007); large desert regions with dunes that reach 150 m high and are between 30 - 50 km long (Lorenz et al., 2006b); mountains (Radebaugh et al., 2007) and a few craters (Elachi et al., 2006; Wood et al., 2010). The lack of craters suggests that Titan's surface is relatively young, which would imply a rapid erosion and/or burial process (Lorenz et al., 2007). Many questions remain about how the atmosphere shapes the surface, and how the surface liquid reservoirs impact atmospheric dynamics. There is some evidence that the equatorial regions once had larger amounts of liquid CH_4 (Tomasko et al., 2005). Does Titan go through cycles where its surface has more liquid cover, or is it steadily losing liquid methane? Regarding Titan's dunes, it was originally predicted that Titan would not be a favorable location for dune formation (Lorenz et al., 1995), and so it is an open mystery how the dunes formed and what their composition is. There have been a couple of proposed mechanisms, but nothing that has been supported by computational modeling (Barnes et al., 2015). Although these dynamical questions would benefit from additional in situ study, comparison studies between the Earth and Titan have also been used to try to understand the physical processes that shape the surface (e.g., Rubin & Hesp (2009); Kok et al. (2012)) and computational modeling methods have also been steadily improved over the years (e.g., Newman et al. (2013)).

1.5 The Dragonfly Mission

In the years since Cassini's Grand Finale, work has been done to interpret the data and there have been follow-up ground-based observations, but what is really needed is another dedicated space mission. Fortunately, NASA's Dragonfly mission is apparent on the horizon. Dragonfly will be a spacecraft unlike any other - a large "rotocopter" that will be able to fly around Titan's surface, taking samples in 5-mile intervals. Given the density of Titan's atmosphere and low surface gravity (1/7th the Earth's), it is relatively easy to have a flying rover. The low surface temperature also makes it easy to store samples at cryogenic temperatures, which increases the mass allocation that might be used for cooling apparatuses that would be necessary on warmer worlds.

Set to launch in 2027 and arrive at Titan in 2034, Dragonfly will sample Titan's equatorial region for roughly three years with three categories of science objectives that can be split into several goals each (from Barnes et al. 2021):

1. Prebiotic chemistry
   (a) Measure compositions of materials in different geologic settings
   (b) Determine presence and abundance of key molecules for Earth-like life

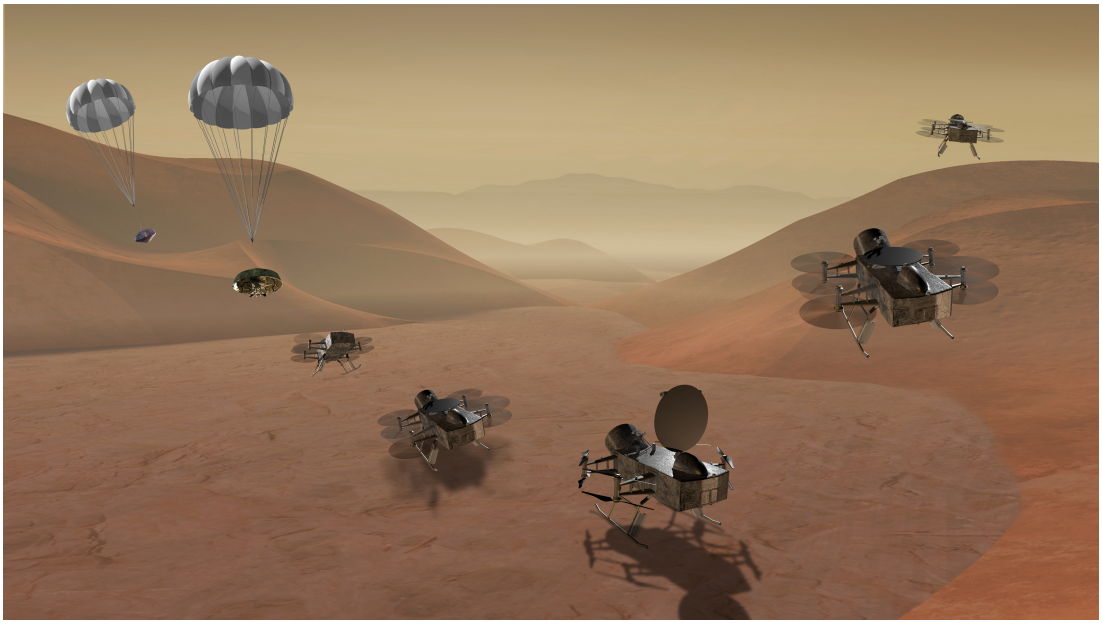

Figure 1.10: Dragonfly's entry, descent, landing, and takeoff

2. Habitable environments
   (a) Constrain the atmospheric methane moisture budget
   (b) Determine the abundance of stored liquid methane
   (c) Study the history of Titan's atmospheric methane
   (d) Determine conditions for aeolian transport
   (e) Determine the transport mode and history of clastic materials
   (f) Determine the geologic context of sampled materials
   (g) Measure current lithospheric activity and constrain past processes
   (h) Constrain the depth to Titan's liquid-water ocean
   (i) Determine the availability of water ice
3. Search for biosignatures
   (a) Determine enantiomeric abundance of chiral molecules
   (b) Determine if patterns exist in molecular masses and distribution
   (c) Determine if metabolic processes are active on the surface

Titan's surface and subsurface liquid stores could contain all of the necessary ingredients for life. Dragonfly's task will be to measure the amounts of those ingredients, how they are interacting with each other and the environment chemically and physically, and whether or not they have come together to form a rudimentary form of life.

Dragonfly will have five instrument packages to achieve these goals (see Figure 1.11) (Lorenz et al., 2018):

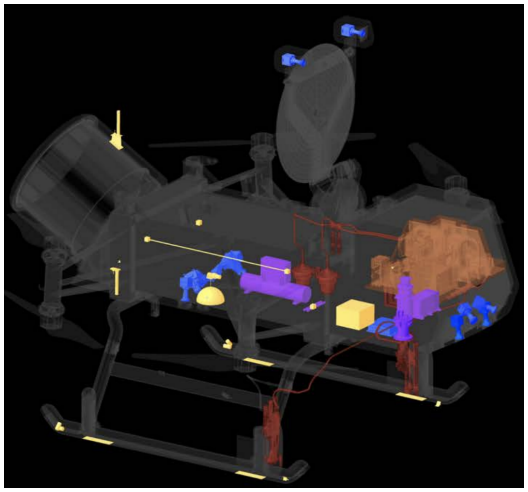

Figure 1.11: Schematic of Dragonfly's instrument packages: DraMS (orange, near the front of the rotocraft), DrACO (dark red, distributed behind DraMS and down to the legs), DraGMet (yellow, distributed throughout the rotocraft chassis and legs), DragonCam (blue, at the top of the rotocraft circular antenna and at the bottom of the rotocraft chassis), and DraGNS (purple, in the middle of the rotocraft chassis).

- DraMS: Mass spectrometer
- DrACO: Drill for Acquisition of Complex Organics
- DraGMet: Geophysics and Meteorology Package
- DragonCam: Camera suite
- DraGNS: Gamma-ray Neutron Spectrometer

Characterizations of the surface and subsurface composition are not complete as mentioned in Section 1.3, but with DraMS and DrACO, Dragonfly will be able to fill in the gaps in our understanding. One of the big questions that ties all three goals together is "what is the boundary between prebiotic and biotic chemistry?" How does the environment cause that particular switch to flip?

It should be noted that Dragonfly will land in Titan's equatorial region which is characterized by dunes as opposed to one of the polar regions where the lakes and seas are. This is largely due to communications and landing physics constraints. Dragonfly must land on Titan's day side in order to communicate with Earth at entry, which excludes the north pole. It also cannot approach at too steep or too shallow an angle or else it risks crashing or missing Titan entirely, excluding the south pole. Figure 1.12 from Lorenz et al. (2021) shows a map of Titan's accessible and inaccessible regions for Dragonfly.

All of this is to say, Dragonfly will not be landing where one would expect to search for prebiotic chemistry and/or signs of life, but the dune fields do contain organic sands. The Selk impact crater where Dragonfly will specifically land was observed with ISS, RADAR, and VIMS to classify the terrain and to make a rudimentary

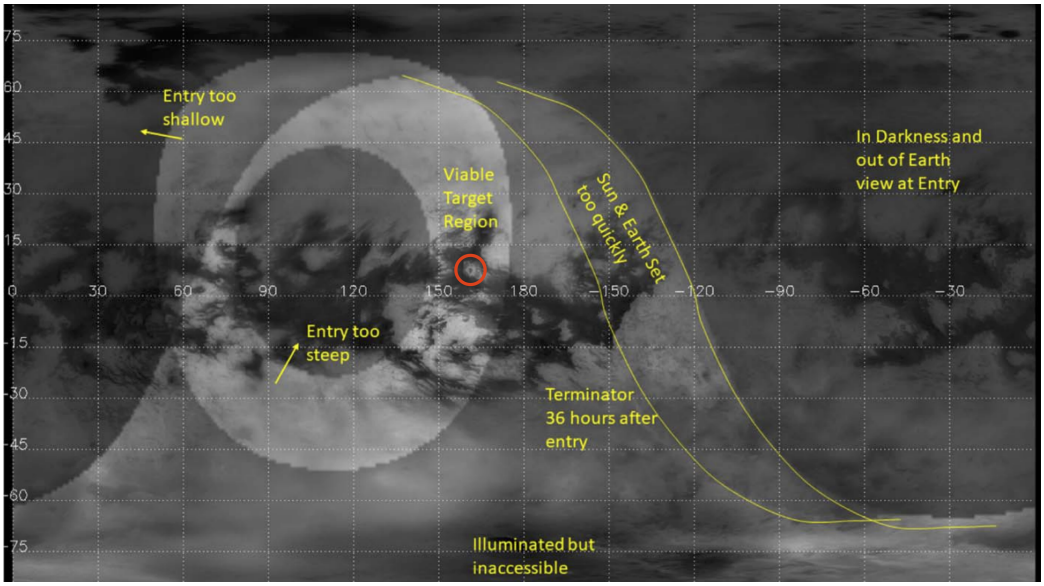

Figure 1.12: Map of Titan's surface with landing constraints from Lorenz et al. (2021). Dragonfly must land on Titan's day side and at an angle that is not too shallow or too steep in order to safely land and communicate with Earth on entry. Dragonfly will thus land in the Selk impact crater (circled in red) in Titan's equatorial region.

characterization of the sand's composition, which largely comprises organic material and water ice. On Earth, life exists in desert dune regions, and so Dragonfly's landing site will still be of astrobiological interest, especially if there's evidence that liquid water interacted with the organic molecules at the time of impact. In laboratory experiments, organic molecules identified in Titan's haze can form amino acids when mixed with water (Neish et al., 2010; Ramírez et al., 2010; Cleaves et al., 2014) - is it possible for something similar to occur on Titan's surface? Although Dragonfly will not be studying the lake regions as part of its main mission, it will have access to a variety of landscapes that host prebiotic chemistry and possibly life.

Dragonfly will land on Titan one Saturn-year after Huygens's landmark descent. In the interim there are studies to interpret the data from Cassini-Huygens and follow-up observations from ground- and space-based telescopes (Cordiner et al., 2020b; Coy et al., 2021) including the James Webb Space Telescope (Nixon et al., 2016, 2021). There is still *a lot* of work to be done, and only recently have the astronomical community's eyes turned towards Titan.

1.6 Thesis Roadmap

As we can see, Titan is a fascinating object of study from an astrobiological perspective. The Cassini-Huygens mission provided the best in situ data we have to date on Titan, and while it answered some questions, we were left with many more at the end of the mission. We hope that Dragonfly will definitively answer these questions, but there is still plenty of work that needs to be done before its launch. This thesis

studies the questions "how is methane produced and replenished on Titan?", "how does Titan's particle environment interact with its atmosphere?", and "how does Titan's atmosphere shape its surface, particularly in the region where Dragonfly will operate?". I use a combination of observational data (space-based and ground-based) and computational modeling to attempt to answer these questions.

This thesis is structured as a "descent" through Titan's atmosphere - starting with its particle environment in orbit around Saturn, moving down through its atmospheric layers, and terminating at the surface. Chapters 2 and 3 describe the interplanetary dust and meteoroid distribution in Titan's orbit, how these objects fall through Titan's atmosphere depositing energy and material, and resulting shock chemistry from larger objects. Chapters 4 and 5 are about the TitanWRF General Circulation Model (GCM) and the observed superrotating jet in Titan's atmosphere. Specifically, Chapter 4 is a brief review of Titan GCMs to date and a in-depth description and analysis of the TitanWRF GCM. Chapter 5 is about my improvements on this model, how it reproduces the superrotating jet, and how this compares to ALMA observations. Chapter 6 is then about how this GCM output can then be used to predict dune orientations on Titan's surface. For the sake of concision and organization, all variables and numerical constants mentioned in each chapter will be summarized in tables in appendices at the end of every chapter. Finally, in Chapter 7 I summarize this thesis's work and discuss future work that naturally arises from these projects.

Chapter 2

Meteoroid Model

2.1 Introduction

There is an abundance of interplanetary material, and determining the composition and distribution of this material is a scientific objective of many missions in the inner and outer solar system. Objects larger than $\sim$ 1cm in radius can be observed from Earth, while particles smaller than 100 μm in radius can be measured by dust analyzers on probes. Interplanetary material with radii between these limits is particularly difficult to study, because they are too large for dust detectors but too small to be optically imaged. Material of all sizes though fall onto the planets and moons, delivering energy and material to their atmospheres. As such, understanding their composition, spatial distribution, and dynamics is important for understanding how they contribute to atmospheric processes on planets and moons with robust atmospheres.

The smallest class of objects is the micrometeoroid, or interplanetary dust, which has a diameter smaller than 30 μm (Koschny & Borovicka, 2017). Their composition depends on their location within the solar system. Particles throughout the solar system, especially in the interior, tend to be "stony" in composition - carbonaceous chondrites (Flynn, 2004; Macke et al., 2011), which are aggregates of different silicate, oxide, and sulfide minerals that were left over after the formation of the solar system. These particles have a range of densities between 2.5 - 4 g/cm^3, depending on the exact proportions of metals, water, and organic compounds within them. Another class of "stony" micrometeoroids is made of iron-nickel alloy, though unlike carbonaceous chondritic particles, they are not of primordial origin. Iron micrometeoroids are debris leftover from the destruction of asteroids and planetesimals (Bottke et al., 2006). Finally, there are "icy" interplanetary dust particles, found beyond the frost line ($\sim$ 3 AU), that are made of water ice and/or other frozen volatiles. Many of these particles are of cometary origin, which will be discussed later in this chapter. There have been many attempts to model the distribution micrometeoroids (Grün et al., 1985; Divine, 1993; Nesvorný et al., 2010), as well as in situ measurements (Love & Brownlee, 1993; Hillier et al., 2007; Poppe et al., 2011), and ground-based

observations (Hauser et al., 1984; Hahn et al., 2002; Janches et al., 2006) for the inner solar system.

The next class of objects is the meteoroid, which the International Astronomical Union (IAU) defines as objects between 30μm and 1m in size, though larger objects that cause a meteor can also be meteoroids (Koschny & Borovicka, 2017). Like micrometeoroids, they are stony, ferric, or some combination of the two in composition. Most rocky meteoroids are found in the asteroid belt and Edgeworth-Kuiper Belt, though there was recently an observation of a rocky body originating from the Oort Cloud reported, resulting in a predicted flux of Oort Cloud meteoroids into the inner solar system (Vida et al., 2023). Meteoroids are large enough that, if they enter a dense atmosphere, they can shock and produce visual phenomena (becoming meteors) and potentially reach the ground before completely evaporating and ablating (becoming meteorites). There have been many studies of meteorites on Earth that have provided crucial information on the composition of inner solar system meteoroids (e.g. Elkins-Tanton et al. (2020); Ferus et al. (2020); Britt & Consolmagno (2003); Buchwald (1975)).

Larger than meteoroids are asteroids, with sizes between 1 m and 1000 km (Koschny & Borovicka, 2017). They are classified according to their composition as determined by spectral emissions: silicate-rich (S-type), carbon-rich (C-type), and metal-rich (M-type). It is difficult to know though if an asteroid is the same composition all the way through without additional observations. Like meteoroids, asteroids are typically confined to the asteroid belt, though there are "trojan" asteroids in orbit around other planets.

The final type of object is the comet. The nuclei have a range of sizes, with the largest observed having a diameter of nearly 130 km in diameter (Hui et al., 2022). Comets are composed primarily of water ice, with some frozen volatiles like ammonia and carbon dioxide, and rocky carbonaceous materials (Fink, 2009; Bockelée-Morvan, 2011; Cochran et al., 2015). They are in orbit around the sun beyond the frost line, and are categorized according to their orbits. Short-period comets (orbital periods $\sim$ 20 years) are those in orbit around Jupiter (Jupiter family comets) or on similar orbits to Haley's comet (Haley-type comets). Long-period comets (orbital periods greater than 200 years) are in orbits originating in the Edgeworth-Kuiper Belt or even the Oort Cloud (Hills, 1981; Stern, 2003). As comets outgas in the vicinity of the sun, the organic molecules that they are made of become part of the particle environment in the orbits of planets.

There have been many studies to determine the precise composition, spatial distribution, and orbital dynamics of all of these interplanetary objects. In addition to ground-based optical and radar observations of the inner solar system (Ostro et al., 2000; Magri et al., 2007; Busch et al., 2011; Shepard et al., 2017), meteorites are often collected for lab analysis (Dell'Aglio et al., 2010; Izawa et al., 2010; Galimov et al., 2013; Elkins-Tanton et al., 2020; Ferus et al., 2020). The Hubble Space Telescope has been used to observe larger objects (Storrs et al., 1999), and small solar system objects have been targets in missions like Kepler (Ryan et al., 2017), the Transiting Exoplanet Survey Satellite (TESS) (Pál et al., 2020), and Gaia (Spoto et al., 2018). The distribution of interplanetary dust has been studied by probes such as Pioneer 10

(Brace et al., 1988), Parker Solar Probe (Szalay et al., 2020), New Horizons (Horanyi et al., 2009), and Cassini (Altobelli et al., 2003; Srama et al., 2004). There is still a lot of work to be done though to constrain the properties of mid-sized meteors, though a combination of observations and computational modeling has been closing this gap over the last several years (Tiscareno et al., 2013).

As one can see, there are many objects with a diverse range of sizes and compositions that can potentially contribute to Titan's atmospheric chemistry. In this chapter (which contains model set up from Flowers & Chyba (in final review)) I will describe Titan's particle environment (Section 2.2), the model framework I use for a study on shock chemistry (Section 2.3), and a discovery of a historical error in how the field has often treated meteoroid dynamics (Section 2.4).

2.2 Particle Environment

Titan's orbit is a rich particle environment, with material originating from Jupiter family comets (Levison & Duncan, 1997; Nesvorný et al., 2010), Halley-type comets (Levison et al., 2006a; Nesvorný et al., 2010), the Edgeworth-Kuiper Belt (Levison & Duncan, 1997; Landgraf et al., 2002; Petit et al., 2011), the Oort Cloud (Nesvorný et al., 2010), Saturn's E-ring (Srama et al., 2006, 2011), and Enceladus's plumes (Hansen et al., 2006; Waite et al., 2006; Spencer et al., 2006; Hartle et al., 2006). Determining how this particle environment affects Titan's atmospheric chemistry requires a combination of in situ and remote observations with dynamical and chemical models. Pioneer 10 took early measurements of the dust distribution in the outer solar system (Han et al., 2011; Levison et al., 2006b; Humes, 1980), and Voyager 1 and 2 measurements of impact-produced plasma were used to infer a dust density for grains with masses of order 10^{-11} g (Gurnett et al., 1997). The New Horizons and Cassini-Huygens missions had improved dust detection systems, and Cassini in particular was able to take direct dust density measurements in the Saturnian system. Figure 2.1 shows dust density data from the CDA on board Cassini (Srama et al., 2004) in addition to the derived distributions from this data as a function distance from Saturn.

The distribution of particles from specific interplanetary sources in the outer solar system is still being studied, though several papers by Poppe *et al.* summarize the current knowledge and model the dust fluxes as a function of heliocentric distance for each source (Poppe et al., 2010; Poppe & Horányi, 2012; Poppe, 2016; Poppe et al., 2019). Edgeworth-Kuiper belt particles with sizes between 0.5 - 5μm have the highest flux into Saturn's orbit (Poppe et al., 2019), but when extending that range to 100μm, Oort Cloud comets and Jupiter Family comets contribute more (Poppe, 2016). These models for the particle flux into the Saturnian system are specifically for dust though, and it is difficult to determine a flux of larger objects. Detectors on probes cannot measure larger particles without risking damage to the instruments, and generally the mass fluxes decrease significantly with size of object.

Although several of the sources mentioned are from comet families, it is likely that they do not contain ice by the time they enter Titan's orbit. Comet-originating

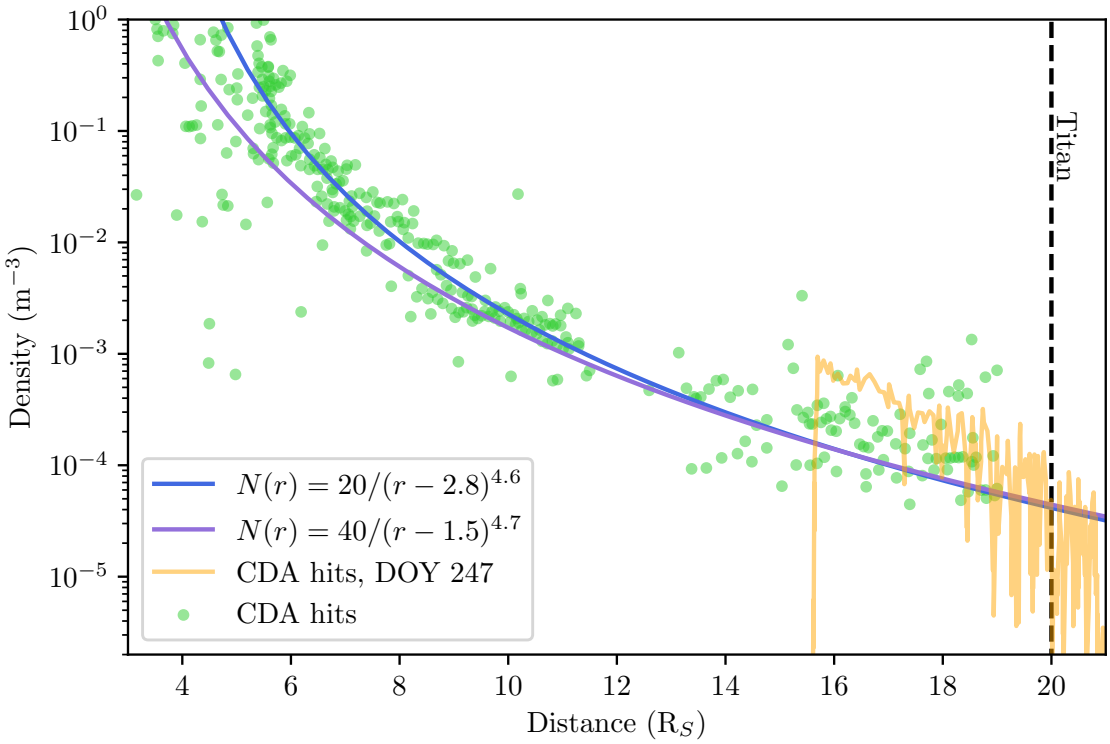

Figure 2.1: E-ring particle density measurements from the Cassini Dust Analyzer (CDA) (points and yellow line) and derived dust number density power laws (blue and purple lines; r is in units of Saturnian radii R_S). This is a recreation and combination of Figures 11 and 12 in Srama et al. (2011), with a line marked at $R_S = 20$ for the approximate location of Titan's orbit. Dust number densities ρ were derived from the dust particle impact rates n_r (s $^{-1}$) upon the detector and the relative dust impact speeds v (m s^{-1}) with the equation $\rho = n_r/(Av)$ where A is the cross-sectional area of the detector.

dust even at 1 AU will be substantially devolatilized. This seems likely to be true at Saturn's heliocentric distance as well. Grigorieva et al. (2007) initially theorized that UV radiation would cause substantial sputtering in addition to sublimation of volatile ices on the surfaces of IDPs in the β Pic system and 11 other systems. The timescales for volatile survival vary (according to particle size) between 10 and 1000 years at 9 AU for a debris disk in orbit around β Pic. This is consistent with the CDA detection and chemical characterization of two IDPs, which finds them to be of stony composition (Flynn, 2004; Hillier et al., 2007; Macke et al., 2011; Gainsforth et al., 2015) . We therefore assume that particles of interplanetary origin at Titan are stony and largely devolitalized.

There is a possible source of water ice though from Enceladus's plumes. In 2005, Cassini observed plumes of water ejected from a hot spot at the south pole (Hansen et al., 2006). It has been hotly debated whether or not this water, ejected into Saturn's E-ring, can reach the orbit of Titan. The detection of a flow of O^+ ions onto

Titan (Hartle et al., 2006), the amount of CO measured (Hörst et al., 2008), and the presence of certain oxygen isotopes on both Titan and Enceladus (Waite et al., 2009; Serigano et al., 2016) suggests that there is "gardening" of Enceladus plume material on Titan. Water ice from Saturn's E-ring also likely impacts Titan's atmosphere, given that the E-ring does extend to Titan's orbit (Srama et al., 2011).

2.3 Equations of Motion and Energy

I use an RK4 method to solve the equations of meteor motion and ablation from Bronshten (1983) and Campbell-Brown & Koschny (2004), converting from a time step to an altitude step and using data from the Huygens lander's HASI instrument for atmospheric density at a given altitude (Fulchignoni et al., 2005). We solve from the top of the atmosphere (defined here to be at z = 1500 km) to the surface.

The energy equation is (Campbell-Brown & Koschny, 2004):

$$\frac{dT}{dz} = \frac{1}{Cmv\cos\theta}\left[\frac{\Lambda\rho v^3}{2}A\left(\frac{m}{\delta}\right)^{2/3} - 4\sigma\epsilon\left(T^4 - T_a^4\right)A\left(\frac{m}{\delta}\right)^{2/3} - L\frac{dm}{dz}\right] \tag{2.1}$$

where C is the specific heat, m is the mass of the particle, v is its velocity, θ is the angle of its trajectory with respect to the vertical, Λ is the heat transfer coefficient, ρ is the atmospheric density at the altitude step, δ is the meteoroid density, σ is the Stefan-Boltzmann constant, ϵ is the emissivity of the particle, T is its temperature, T_a is the atmosphere's temperature at the altitude step, A is the shape factor, and L is the heat of ablation. The velocity equation is:

$$\frac{dv}{dz} = -\frac{1}{cos\theta}\frac{\Gamma\rho v}{m}A\left(\frac{m}{\delta}\right)^{2/3} + \frac{g}{v} \tag{2.2}$$

with

$$g = g_T\left(\frac{R_T}{R_T + z}\right)^2, \tag{2.3}$$

where $g_T = -1.352$ m s^{-2} is the gravitational acceleration of Titan at surface level, R_T the radius of Titan, and Γ the drag coefficient. Finally, for the ablation equation we take (Bronshten, 1983):

$$\frac{dm}{dz} = -\frac{1}{cos\theta}\frac{A\Lambda}{2L}\left(\frac{m}{\delta}\right)^{2/3}\rho v^2. \tag{2.4}$$

Particles entering the atmosphere can also lose mass at due to sputtering, which on Earth may set in at altitudes much higher than those at which ablation modeled by Eq. 2.4 becomes important. (Sputtering is due to direct collisions of atmospheric molecules with the surface of the meteoroid, thereby dislodging surface material.) But this process appears to be important only for incident particle velocities above about 30 km s^{-1}. Above this velocity, some incident particles (depending on mass and density) may sputter away $\sim 10 - 20\%$ of their initial mass (Hill et al., 2004;

Popova et al., 2004). Given the average meteoroid impact velocity of 18 km $^{-1}$ at Titan found here, we ignore the effects of sputtering in this discussion.
Finally we also model how θ changes using the equation from (Chyba et al., 1993):

$$\frac{d\theta}{dz} = \left(\frac{1}{v\cos\theta}\right)\left(-\frac{g\sin\theta}{v} + \frac{C_L\rho S_A v}{2m} + \frac{v\sin\theta}{R_T + z}\right) \tag{2.5}$$

Values of the constants used in our atmospheric entry simulations are shown in Table 3.4, along with references for these choices. In the free molecular flow regime, we expect $\Lambda \approx 1$ (Grebowsky, 1981), and this is the choice commonly made in the literature modeling atmospheric entry of microscopic dust. For objects large enough to generate atmospheric shock waves (meteoroids), however, this number is too high, and observations suggest $\Lambda = 0.5$ is a more appropriate choice (Bronshten, 1983; Campbell-Brown & Koschny, 2004). Because we choose $\delta = 3400$ kg m^{-3} for meteoroid density, for consistency we use parameters appropriate for carbonaceous meteoroids.

2.4 A Note on Historical Models

Previous modeling of meteoric entry into Titan's atmosphere has often been based on the equations for meteor velocity, ablation, and thermal radiation given by Lebedinets et al. (1973) and then propagated through the literature (e.g. Pesnell & Grebowsky (2000), Molina-Cuberos et al. (2001a), Pandya & Haider (2014), Popova et al. (2019)). However, these equations contain major errors that appear to have gone uncorrected, and that significantly affect the results of atmospheric entry simulations. We briefly summarize these errors and their effects here, before describing the model we employ.

The Lebedinets *et al.* ablation equation for a meteor of mass m and density δ is:

$$\frac{dm}{dt} = -\frac{4AC_1 m^{2/3}}{\delta^{2/3}T^{1/2}}e^{-C_2/T} - \frac{\Lambda_S A\rho m^{2/3}v^3}{2Q\delta^{2/3}} \tag{2.6}$$

where t is time, A is the shape factor, T is the temperature, C_1 and C_2 are constants that describe the dependence of the evaporation rate on the temperature (given as 6.92×10^{10} g cm^{-2} and 5.78×10^4 K respectively), Λ_S is the sputtering coefficient given by the equation $\Lambda_S(T) = 6 \times 10^{-6}\exp(T_m/290)$, ρ is atmospheric density (a function of altitude, and therefore time, as the meteor descends), v is the meteor's velocity, and Q is the energy of evaporation of a stony meteor (6×10^{10} erg g^{-1}). The corresponding energy equation is (Molina-Cuberos et al. (2001a)):

$$\frac{dT}{dt} = \frac{4A\rho v^3}{8C\delta^{2/3}m^{1/3}}(\Lambda - \Lambda_S) - \frac{4A\sigma T^4}{C\delta^{2/3}m^{1/3}} - \frac{4AC_1 Q}{C\delta^{2/3}T^{1/2}m^{1/3}}e^{-C_2/T} \tag{2.7}$$

where Λ is the heat transfer coefficient, C is the specific heat, and σ the Stefan-Boltzmann constant. The coefficients Λ and Λ_S are unitless.

Equations 2.6 and 2.7 are dimensionally incorrect in both terms of Equation 2.6 and in the third term of Equation 2.7. Instead of producing units of mass per second as required, the first term of Equation 2.6 has units $g\ K^{-1/2}$ and its second term has

units of s^{-1}. The third term in Equation 2.7, which should have units of temperature per second, is instead $K^{1/2}$. The terms containing $T^{-1/2}e^{-C_2/T}$, which describe how ablation is affecting the mass and temperature, are particularly problematic. Evaluating these terms individually results in a value that is essentially zero, negating the effects of evaporation in the mass loss equation and loss of heat through ablation in the change in temperature equation. In our model, which uses corrected forms of these equations, we find the corresponding terms (in Equations 2.1 and 2.4 below) to be non-negligible. When comparing the terms in the temperature equations that pertain to ablation, we find that the ablation term in the Lebedinets formulation is 10^{67} times smaller than the corresponding term in our equation 2.1. As such, we caution against the continued use of the meteor entry equations from Lebedinets et al. (1973), or results from papers that have directly adopted these equations.

Appendix

2.A Definitions of Symbols

Variable	Description	Equation
T	Temperature	2.1
z	Altitude	2.1
m	Mass	2.1
v	Velocity	2.1
θ	Trajectory angle	2.1
ρ	Atmosphere density	2.1
T_a	Atmosphere temperature	2.1

Table 2.1: Descriptions of symbols with location of first appearance

2.B Numerical Constants

Description	Symbol	Value	Equation
Specific heat	C	9×10^6 erg/g/K	2.1
Heat transfer coefficient	Λ	0.5	2.1
Meteoroid material density	δ	3.4 g/cm^3	2.1
Emissivity	ϵ	0.9	2.1
Shape factor	A	1.2	2.1
Heat of ablation	L	8.1×10^{10} erg/g	2.1
Drag coefficient	Γ	1	2.2
Lift coefficient	C_L	10^{-3}	2.5
Radius of Titan	R_T	2,574.7 km	2.3

Table 2.2: Values for constants

Chapter 3

Particle-Atmosphere Interactions

3.1 Introduction

Saturn's moon Titan is the only planetary satellite in our solar system with a dense ($\sim$ 1.5 bar) atmosphere, which has an overall composition of 94.2% N_2, 5.65% CH_4, 0.1% H_2, and smaller amounts of nitriles, hydrocarbons, and other organics (Strobel, 2010; Hörst, 2017). This atmosphere provides an arena for abundant organic chemistry, thought to be driven primarily by solar ultraviolet (UV) and charged particle radiation. (Sagan & Thompson, 1984; Yung et al., 1984b; Krasnopolsky, 2009; Snowden & Yelle, 2014). In the upper atmosphere, molecular nitrogen and methane are dissociated by UV and charged magnetospheric particles, resulting in various C-H-N species. These products then participate in a wide variety of chemical reactions with each other and the ambient neutral and ionized species (such as magnetospheric O^+ (Hartle et al., 2006)) to produce additional hydrocarbons, neutral atomic species, and other C-H-N-O species as described in detail by, for example, Sagan & Thompson (1984), Yung et al. (1984b), Cabane & Chassefière (1995), Krasnopolsky (2009), and Snowden & Yelle (2014). Neutral hydrogen species (H and H_2) in particular are produced through the dissociation of methane and ambient hydrocarbons, but are quickly lost from the atmosphere due to Titan's low gravity. Various studies show that neutral hydrogen production peaks below 1000 km, with atomic hydrogen production peaking at roughly 800 km (Lebonnois et al., 2003) and molecular hydrogen production peaking at roughly 550 km (Krasnopolsky, 2009).

Titan's atmosphere is also subject to a constant bombardment of dust particles and meteoroids. Many families of particles contribute to this flux, including interplanetary dust particles (IDPs) of various origins as well as material from Saturn's extensive ring system. Sources of interplanetary material include Jupiter-family comets (JFCs), Kuiper Belt objects (KBOs), Halley-type comets (HTCs), and Oort Cloud comets (OCCs) (Levison et al., 2006b). Cassini-Huygens spacecraft measurements show that Saturn's E ring extends out to Titan and beyond (Srama et al., 2006, 2011), providing a population of dust impactors on Titan that originate with Saturn's active moon Enceladus.

Particles falling into Titan's atmosphere are an important source of material that can participate in chemical reactions (English et al., 1996; Molina-Cuberos et al., 2001b). Sufficiently large particles moving at hypersonic speeds will also generate atmospheric shocks (Lin, 1954; Revelle, 1976; Silber & Brown, 2014; Silber et al., 2017, 2018). Shocks in an N_2/CH_4 atmosphere have long been known to be an especially efficient source of organic synthesis (e.g. Rao (1966, 1967); Bar-Nun & Shaviv (1975); Borucki et al. (1988); Scattergood et al. (1989); Cabane & Chassefière (1995); Hörst et al. (2018)), with experimental yields (molecules produced per joule of input energy) higher than those for UV or charged particles for some species (Scattergood et al., 1989; Chyba & Sagan, 1992). However, particles whose characteristic size R is sufficiently smaller than the atmospheric mean free path λ at a given altitude in the atmosphere will not generate shocks at that altitude, because the atmosphere cannot be compressed by the particle (Silber et al., 2018). (This criterion will be rendered more specific below.) For specificity we will label as "meteoroids" those particles large enough to generate shocks at some point during their atmospheric entry, ablation, and deceleration, and those that are too small to generate shocks as "dust" particles.

Meteoroid-generated shock waves of sufficient energy have previously been recognized as a potential energy source for organic synthesis on Titan (Scattergood et al., 1989), but the importance of the effect could not be reliably quantified, because only the microscopic dust flux at Saturn had been measured. However, the Cassini spacecraft imaged the results of meteoroid impacts on Saturn's rings, allowing for the first time an observational estimate to be made of the flux and size-frequency distribution of meteoroids at Saturn, and therefore at Titan (Tiscareno et al., 2013). Here, we combine these observationally derived meteoroid flux models and Huygens atmospheric data with yields for organic shock synthesis in N_2/CH_4 gas mixtures from theoretical calculations and shock-tube experiments to predict the quantity of organics expected to be produced in Titan's atmosphere by meteoroid infall.

In Figure 3.1 we show the temperature-density profile as measured by the Huygens Atmospheric Structure Instrument (HASI) (Fulchignoni et al., 2005) that we use in our model. The horizontal lines correspond to where in the atmosphere the particles begin to shock. This is the altitude where they meet the threshold value for the Knudsen number, which we will discuss in more detail in Section 3.3.

This chapter is comprised of results and discussion from Flowers & Chyba (in final review). In Section 3.2 we present flux models for microscopic dust and meteoroids at Titan, calculating impact velocities and the effects of gravitational focusing due to both Saturn's and Titan's gravitational attraction. We then calculate the total mass, and therefore shock energy, available from the meteoroids to drive organic synthesis. This requires determining the smallest meteoroid particle size capable of generating a shock in Titan's atmosphere, and this in turn requires the use of an atmospheric entry model since λ varies with altitude. We present this model in Section 3.3. In Section 3.4 we review relevant experimental and theoretical results for N_2/CH_4 shock synthesis. In Section 3.5, we calculate overall shock production in Titan's atmosphere. Finally, in Section 3.6, we compare these results with those from a standard photochemical model, discuss uncertainties, and draw conclusions. While there are significant uncertainties (quantified below), organic shock production

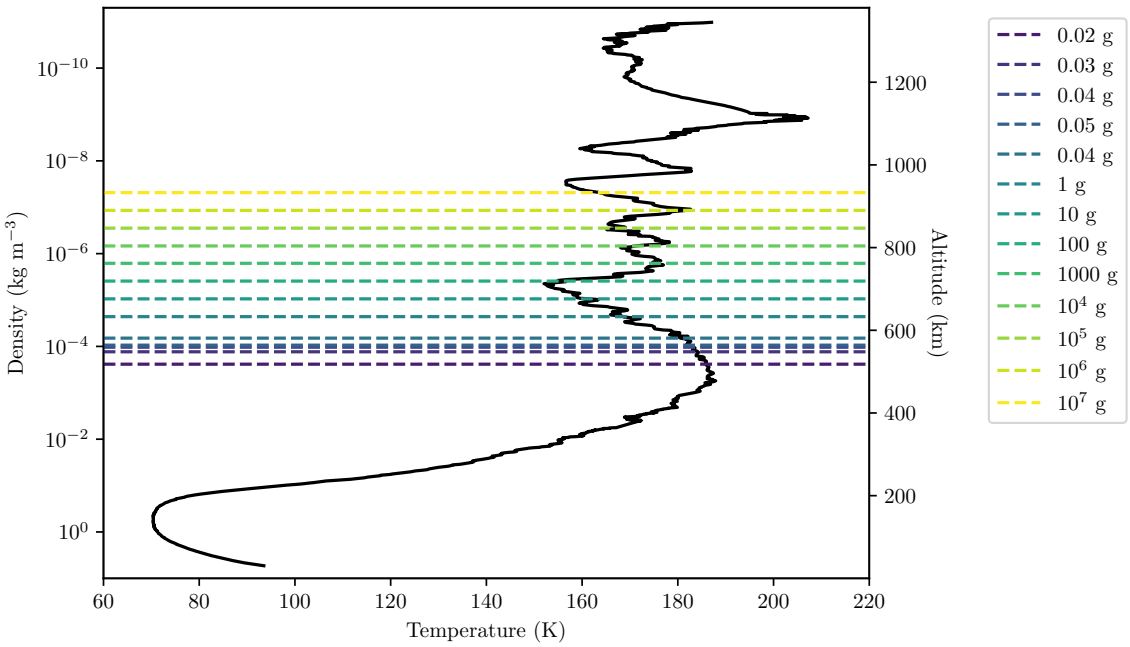

Figure 3.1: Temperature-density-altitude profile of Titan's atmosphere as measured by HASI. The dashed lines note where the particles in our study begin to shock in the atmosphere; the criterion for the shocking condition will be described in Section 3.3.

from meteoroids appears to be so significant that Titan atmospheric chemistry models must henceforth take these effects into account.

3.2 Impact Fluxes and Velocities

There are a number of models for the dust flux at Saturn as a function of particle mass. We summarize some of the most prevalent of these in Fig. 3.2. Grün et al. (1985), Divine (1993), Poppe & Horányi (2012), and Poppe (2016) predict fluxes for particles between 0.5 – 100 μm, originating from the Jupiter family comets, Halley-type comets, the Kuiper Belt, and the Oort Cloud, and while these microscopic particles have the largest flux into the Saturnian system, we will see in Section 3.3 that they are too small to drive shock chemistry in Titan's atmosphere.

However, Tiscareno et al. (2013) report observations taken by Cassini's Imaging Science Subsystem (Porco et al., 2004b) of ejecta clouds produced by impacts on Saturn's A, B, and C rings that allow them to estimate a flux Φ as a function of radius R for meteoroids in the centimeter-to-meter range. Meteoroids in this size range are easily large enough to generate shocks in Titan's atmosphere. Tiscareno *et al.*'s flux estimates (their value for Φ) do not account for two effects that are important for our modeling: gravitational focusing by Saturn (by which Saturn's gravity both increases infalling particle velocities and increases their flux by drawing them in toward Saturn), and the two-dimensional nature of the target presented by

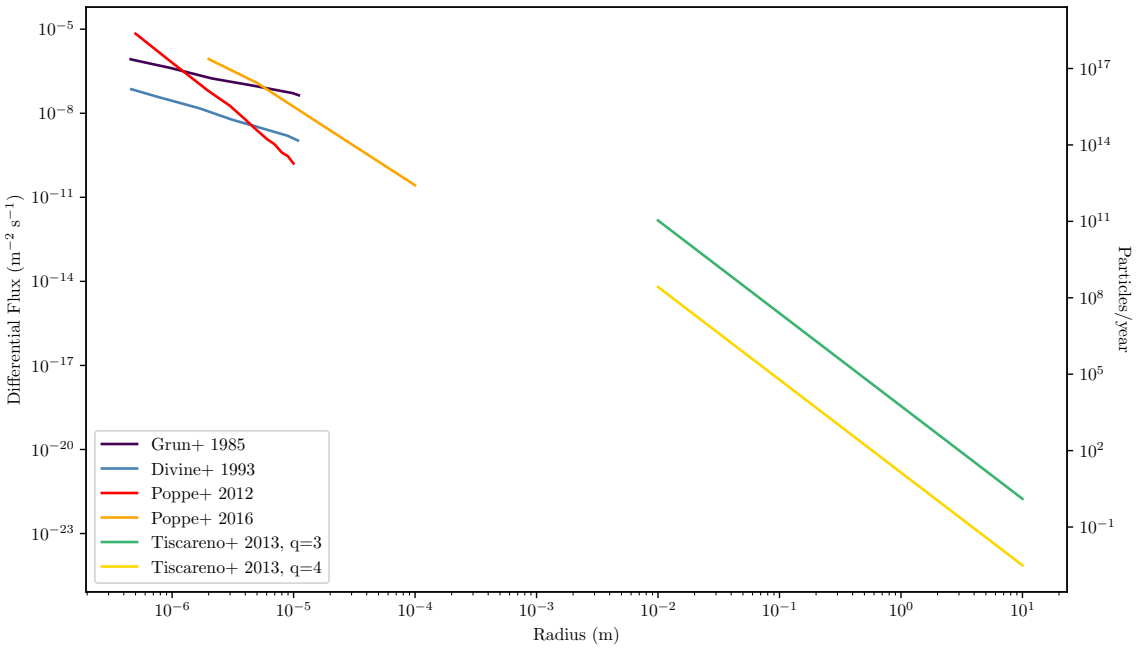

Figure 3.2: Comparison of model fluxes for dust particles and meteoroids in the outer solar system at the heliocentric distance 9.5 AU. The Poppe & Horányi (2012) and Poppe (2016) models were constrained by data from the New Horizon's Student Dust Counter, while those of Tiscareno et al. (2013) were constrained by observations of ring impacts seen by the Cassini orbiter. As described in the text, we have adjusted the Tiscareno *et al.* models to correct for the gravitational focusing effects of Saturn, and have changed their model to assume a density of 3400 kg m^{-3} (see text), rather than their choice of 1000 kg m^{-3}.

Saturn's rings. Their flux estimates must therefore be adjusted by some velocity-dependent factor f_∞ that accounts for these effects. The gravitational focusing factor at some point in space a distance r from the center of Saturn is given by Colwell (1994):

$$G(r) = 1 + \frac{1}{2}\left(\frac{v_{Sesc}(r)}{v_\infty}\right)^2, \tag{3.1}$$

where

$$v_{Sesc}(r) = (2GM_S/r)^{1/2} \tag{3.2}$$

is Saturn's escape velocity at r, with $G = 6.67 \times 10^{-11}$ m^3 kg^{-1} s^{-2} the gravitational constant, $M_S = 5.68 \times 10^{26}$ kg the mass of Saturn, and v_∞ the meteoroid's velocity at "infinity" – say at Saturn's Hill radius. Tiscareno *et al.*'s results depend most strongly on B- and C-ring impacts, so we take $r = 92,000$ km, or 1.6 R_S (saturnian radii), corresponding to the boundary between the B and C rings. For this r, we have $v_{Sesc}(r) = 28.7$ km s^{-1} from Eq. 3.2.

Poppe (2016) finds that the IDP mass flux at Saturn's Hill radius is dominated by the OCC population, consistent with Grün *et al.*'s earlier conclusion. Poppe calculates

the median velocity distribution for this family of grains (with radii of approximately 0.5 μm to 100 μm), and finds it to be 16 km s^{-1}, again before any acceleration due to Saturn's gravity. Cuzzi & Durisen (1990) argue that meteoroids impacting Saturn's rings are also primarily Oort cloud-originating objects. Taking $v_\infty = 16$ km s^{-1} for OCC-originating meteoroids gives $G(r = 1.6\ R_S) = 2.6$ by Eq. 3.1. (We note that IDPs experience size-dependent non-gravitational forces such as radiation pressure and Poynting-Robertson drag that are insignificant for larger meteoroids; we ignore these complications here.) The two-dimensional nature of Saturn's rings reduces the extrapolation of the flux to the Hill radius by another factor of two (Tiscareno et al., 2013), so that we take $f_\infty = 1/(2 \times 2.6) = 0.19$ as the multiplicative factor needed to extrapolate from a flux at the B/C ring boundary to "infinity". Our plot of the Tiscareno *et al.* data in Fig. 3.2 uses this value for f_∞.

To extrapolate Φ to Titan, we must then account for the gravitational focusing due to Saturn's escape velocity at Titan's distance of 20.3 R_S. At this distance, $v_{Sesc}(r) = 7.9$ km s^{-1} and $G(r = 20.3\ R_S) = 1.1$. Titan's escape velocity v_{Tesc} at the top of its atmosphere, which in our simulations we will take to lie at an altitude of 1,500 km, is 2.10 km s^{-1}. This increases $G(r)$ by only about 1%. Extrapolating Φ at infinity to Titan therefore requires multiplying by a factor $f_T = 1.1$. A typical meteoroid impact velocity v_i at 1,500 km above Titan's surface is given by

$$v_i^2 = v_\infty^2 + v_{Sesc}^2 + v_{Tesc}^2, \tag{3.3}$$

which gives $v_i = 18$ km s^{-1}. As a consistency check, we note that the impact velocity at, say, Saturn's B/C ring boundary resulting from this approach is 33 km s^{-1}, consistent with the velocities found by Cuzzi *et al.* in their work on saturnian ring impacts from Oort cloud meteoroids.

Tiscareno *et al.* adopt a power-law distribution for the ejecta produced by meteoroid impact with Saturn's rings, viz. $n(s) = n_0 s^{-q}$, where $n(s)ds$ is the number of ejecta particles with radius between s and $s + ds$, and $3 < q < 4$. For the two end-member cases $q = 3$ and $q = 4$, their regression over their data ultimately yields two possible equations for the meteoroid flux Φ:

$$\log \Phi_3 = -19.476 - 3.643 \log R, \tag{3.4}$$

and

$$\log \Phi_4 = -22.086 - 3.643 \log R, \tag{3.5}$$

where R is the (assumed spherical) meteoroid radius in meters and Φ_q has units of m^{-2} s^{-1}. These are cumulative fluxes, meaning that they give the number flux of all meteoroids with radii $\geq R$. Note that the corresponding equations in Tiscareno *et al.* are in error due to a calculational mistake. Eqs. 3.4 and 3.5 above are the correct expressions (Tiscareno, personal communication, 2022). Although not stated explicitly in their paper, Tiscareno *et al.* assumed a spherical meteoroid density $\delta = 1000$ kg m^{-3} in deriving these equations (Tiscareno, personal communication, 2022).

Eqs. 3.4 and 3.5 can also be written as

$$\Phi_q = a_q R^b, \tag{3.6}$$

where $a_3 = 3.34 \times 10^{-20}$ m^{-2-b} s^{-1}, $a_4 = 8.20 \times 10^{-23}$ m^{-2-b} s^{-1}, and $b = -3.643$.

We note that recent models for microscopic dust at Saturn assume a higher density, with δ between 2500 - 4000 kg m^{-3} (e.g. Poppe (2016)), and that this has been corroborated by some in situ measurements of IDP composition (e.g. Flynn (2004); Macke et al. (2011)). We therefore change the impactor density δ implicit in Eqs. 3.4 and 3.5 from 1000 kg m^{-3} to 3400 kg m^{-3}, a value that is also used in several recent models, particularly those that cite Ip (1990) for parameters, and is determined observationally. Because $R \propto \delta^{-1/3}$, this is equivalent to multiplying R by a factor 0.6650. Eqs. 3.4 and 3.5 then become

$$\log \Phi_3 = -18.831 - 3.643 \log R, \tag{3.7}$$

and

$$\log \Phi_4 = -21.441 - 3.643 \log R, \tag{3.8}$$

and these are the equations that we have used for the meteoroid flux in Fig. 3.2. There is a gap in the models shown in Fig. 3.2 between $\sim 10^{-7}$ g and $\sim 10^{-4}$ g, due to the lack of observational evidence for particles in this mass range – they are too large to be detected by spacecraft dust impact instruments, but too small (so far) to be probed by optical observations.

Following Eqs. 3.7 and 3.8, the coefficients in Eq. 3.6 for the cumulative flux become $a_3 = 1.48 \times 10^{-19}$ m^{-2-b} s^{-1}, $a_4 = 3.63 \times 10^{-22}$ m^{-2-b} s^{-1}, and again $b = -3.643$. The differential flux (the flux per particle radius) is given by

$$\partial \Phi_q / \partial R = b a_q R^{b-1}, \tag{3.9}$$

where $q = 3$ or 4. We can then calculate the total mass flux of meteoroids (assumed spherical) in the range of radii from R_2 to R_1 as

$$M_q = f_T f_\infty \int_{R_2}^{R_1} \frac{4}{3} \pi \delta R^3 \left(\frac{\partial \Phi_q}{\partial R} \right) dR, \tag{3.10}$$

where Φ_q is given by either Eq. 3.7 or 3.8, and M_q has units of mass flux, kg m^{-2} s^{-1}. By Eq. 3.9 this gives:

$$M_q = f_T f_\infty \frac{4}{3} \pi \delta \left(\frac{b}{b+3} \right) a_q (R_1^{b+3} - R_2^{b+3}). \tag{3.11}$$

By Eq. 3.11, if $R_2 \gg R_1$, M_q is dominated by the choice of R_1–the smallest meteoroid included in the calculation.

In principle one should also integrate over an intrinsic velocity distribution about v_i, but this distribution is unknown for centimeter-to-meter scale meteoroids at Saturn. Titan orbits Saturn with an orbital velocity of $v_{Torb} = 5.6$ km s^{-1}, so that impact

velocities vary sinusoidally from its leading to trailing edge like $v_i + v_{Torb} \cos\psi$, where ψ is 0 at Titan's leading point and π at Titan's trailing point. Obviously this does not change the average impact velocity with Titan (though it does represent a significant hemispheric variation); we defer examination of the effects of this variation to a subsequent investigation.

3.3 Atmospheric Entry and Shock Generation

What is the smallest meteoroid that will generate a shock in Titan's atmosphere? This depends on the Knudsen number Kn, defined as the ratio of the atmosphere's mean free path λ to the particle radius R:

$$Kn = \frac{\lambda}{R} \tag{3.12}$$

When Kn is sufficiently large (in the free molecular flow regime) there can be no shock. Intuitively, one might expect that shocks should only set in for $Kn \ll 1$. But while that may hold for reentry vehicles, it does not hold for meteors, for two reasons (Silber et al., 2018; Moreno-Ibáñez et al., 2018). One is that the ablating meteor forms a vapor cap whose dimensions can be two order of magnitude larger than the original meteoroid itself. The other is that the mean free path around the ablating meteor is smaller than the mean free path λ in the atmosphere. And in fact meteor shocks in Earth's atmosphere set in at much higher altitudes (corresponding to much larger values of Kn) than would be the case for reentry vehicles. Observationally, meteors with $R \geq 2$ mm create shocks in Earth's upper atmosphere, at altitudes of around 90 km and below.

At 90 km, Earth's atmospheric number density is $n = 7.12 \times 10^{19}$ m^{-3}, and $\lambda = 2.37$ cm (US Standard Atmosphere, 1976), corresponding to $Kn = 12$ in Eq. 3.12. The mean free path $\lambda = (n\sigma)^{-1}$, where σ is the cross section for collision for the atmospheric molecules. Earth's atmosphere is dominated by N_2 and O_2; for N_2, $\sigma = 0.43$ nm^2 and for O_2, $\sigma = 0.40$ nm^2 (Atkins, 1986). Titan's atmosphere is dominated by N_2 with about five percent CH_4, for which $\sigma = 0.46$ nm^2 (Atkins, 1986), so that σ in Titan's atmosphere may be taken to be the same to within a few percent as that of Earth. We can therefore take shocks in Titan's atmosphere to occur for meteoroids of radius R that penetrate deeply enough to reach a value of n corresponding to a λ that gives the same Kn threshold value for shock creation as in Earth's atmosphere, *viz.* $Kn = 12$.

To determine this R, we use

Figure 3.3 shows the results of our atmospheric entry simulations for meteoroids of different masses. Larger particles penetrate more deeply into the atmosphere before ablating away. Figure 3.3 also shows the $Kn = 12$ threshold; particles penetrating below this line generate shocks. We see that shocks will be generated by meteoroids with $m \geq 0.02$ g or $R \geq 1.1$ mm. To within a factor of two, this is in agreement with the size threshold for shock generation at Earth (Silber et al., 2018), despite Titan's more extended atmosphere.

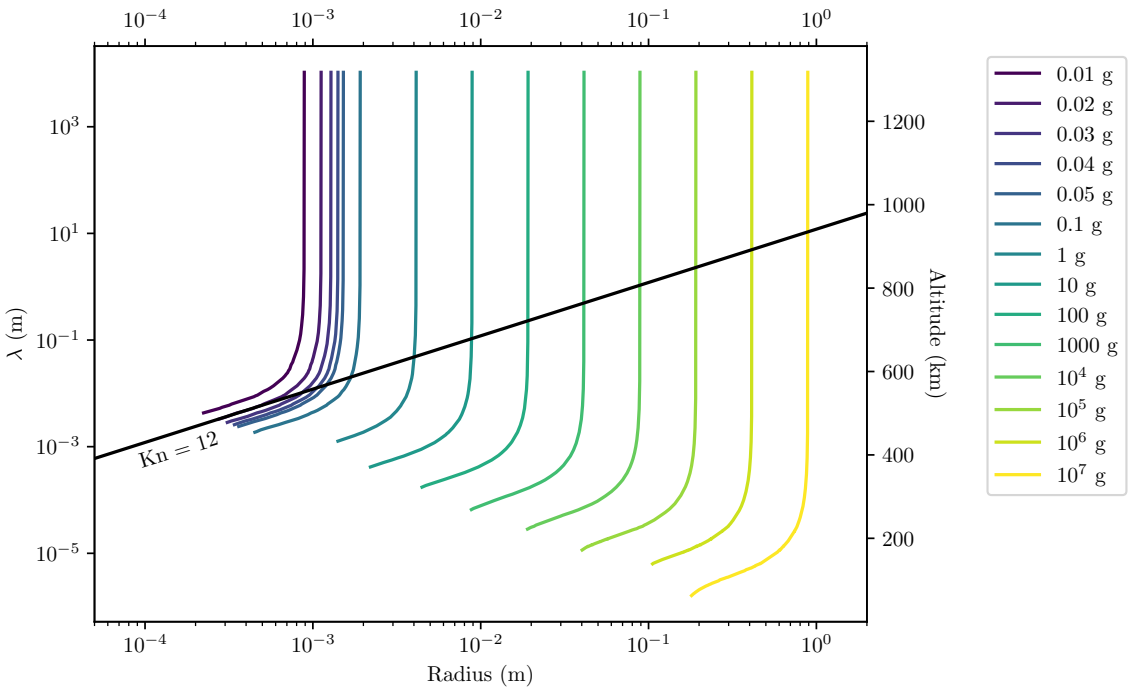

Figure 3.3: Particle mass and radius versus altitude and mean free path λ for ablating meteors Titan's atmosphere. Meteoroids whose trajectories reach below the black $Kn = 12$ line (corresponding to meteoroids with masses greater than 0.02 g) generate shocks that may lead to organic synthesis.

3.4 Shock Synthesis of Organic Molecules

Atmospheric shocks produced by meteoroids entering Earth's atmosphere have been extensively modeled (Lin, 1954; Revelle, 1976; Silber, 2014; Silber et al., 2017, 2018). The meteoroid loses its kinetic energy $E = (1/2)mv^2$ in the atmosphere by both deceleration and ablation; this loss per path length is just:

$$\frac{dE}{dz} = mv\frac{dv}{dz} + \frac{v^2}{2}\frac{dm}{dz}, \tag{3.13}$$

where we have used $d/dt = vd/dz$. The dv/dz deceleration term in Eq. 3.13 generates the bow shock wave at the front of the meteoroid; the dm/dz term leads to the cylindrical shock wave that trails behind the object (Silber et al., 2017). Using Eqs. 2.2 and 2.4, and ignoring the gravitational acceleration term which is unimportant compared to the drag term at the altitudes in the atmosphere where our meteoroids deposit the bulk of their energy and end their trajectories, the comparative contribution of ablation and deceleration to E is:

$$\frac{\frac{v^2}{2}\frac{dm}{dz}}{mv\frac{dv}{dz}} = \frac{\Lambda v^2}{4\Gamma L}. \tag{3.14}$$

For the parameter values in Table 3.4 this ratio equals 5 at our initial velocity of 18 km s^{-1} and decreases as the meteoroid decelerates, equaling 1 at a velocity of 8 km s^{-1}. That is, while a significant amount of the meteoroid's kinetic energy feeds the creation of the bow shock, the majority of its energy feeds the cylindrical shock until the meteoroid has lost ∼80% of its initial kinetic energy.

The effect of the shock passing through a given parcel of the atmosphere is to heat that parcel to high temperatures, driving chemical reactions by exciting and dissociating (depending on the duration and magnitude of the temperature spike caused by the shock) some of the atmospheric molecules. After the passing of the shock, these excited molecules and molecular fragments continue to recombine to form new species until the temperature falls to below a particular species' "freeze-out" temperature T_F. This is the temperature at which the chemical lifetime of that species exceeds the characteristic cooling time of the shocked atmosphere. The resulting concentrations of particular synthesized species are "frozen in" and persist even as temperatures fall far below T_F (Chameides, 1979; Chameides & Walker, 1981).

A number of authors have modeled this process for Earth's contemporary N_2/O_2 atmosphere (e.g. Chameides (1979); Silber et al. (2017)), or its early, possibly more reducing atmosphere (Chameides & Walker, 1981; Ferus et al., 2017). Here we consider analogous work for N_2/CH_4 atmospheres appropriate for modeling Titan. We use the N_2/CH_4 atmosphere thermochemical-hydrodynamic cylindrical shock chemistry calculations of Chameides & Walker (1981) that are built on the cylindrical shock physics calculations of Lin (1954). We find good agreement between the results of their calculations and results from shock-tube experiments for N_2/CH_4 (Rao, 1966, 1967; Bar-Nun & Shaviv, 1975) gas mixtures, with support from more recent shock-tube experiments examining N_2/CH reactions (Dean et al., 1991; Lindackers et al., 1991). Finally, we compare these results with those of laser-induced plasma (LIP) experiments with N_2/CH_4 gas mixtures (Borucki et al., 1988; Scattergood et al., 1989; Ferus et al., 2017).

Silber et al. (2017) discuss the shock chemistry that results from meteoroids entering Earth's atmosphere, treating the deposition of energy behind the meteoroid as an exploding cylindrical line source (Lin, 1954). They state that energy deposited per unit length, E_0, may reach $\sim 10^3$ J m^{-1}, leading to temperatures behind the resulting cylindrical shock wave as high as 6000 K. (Temperatures in the vapor cap at the front of the meteoroid will be significantly higher, likely in excess of 10,000 K (Silber et al., 2017; Anderson, 2019), but the bulk of the object's kinetic energy is released in the trailing cylindrical shock wave, so the focus is on that phenomenon.) Molecular oxygen (O_2) has a dissociation energy of 5.12 eV/molecule (118 kcal/mole), and begins to dissociate at shock temperatures as low as 2000 K, with nearly all of it dissociated by 4000 K. Molecular nitrogen (N_2) has a much higher dissociation energy of 9.76 eV/molecule (225 kcal/mole), and does not dissociate until temperatures above 4000 K. Nevertheless nitric oxide (NO) begins to be produced at temperatures as low as 2000 K (Anderson (2019), Fig. 11.12). This is because there are at least two separate paths to the production of NO. Nitric oxide may be produced by a path in which N_2 is first dissociated, followed by the exothermic reaction $N + O_2 \rightarrow NO + O$. But it may also result from a Zel'dovich mechanism in which a more easily produced oxygen atom

O reacts with a vibrationally excited molecular nitrogen molecule, N_2*, according to $O + N_2^* \rightarrow NO + N$. The activation energy for this reaction is only 3 eV/molecule (69 kcal/mole), lower than either the O_2 or N_2 dissociation energy (Fridman, 2008). The vibrational excitation $N_2 \rightarrow N_2^*$ of the N_2 molecule is itself a resonance process driven by the impact of electrons with energies of $1.7 - 3.5$ eV (Fridman, 2008).

The Zel'dovich mechanism for NO production on Earth points to the explanation for why the production of hydrogen cyanide (HCN) in shocked N_2/CH_4 atmospheres begins at temperatures as low as 2500 K. Rao reports data from twenty-one shock-tube experiments with N_2/CH_4 gas mixtures in a 1:1 ratio diluted in Ar for shock temperatures between 2000 K and 5750 K (Rao, 1966, 1967). Generation of acetylene, C_2H_2, ethane, C_2H_4, and carbon "soot" is observed at 2000 K and higher temperatures; HCN production begins by 2500 K and increases toward higher temperatures, with a corresponding drop in C_2H_2 production as more C is incorporated into HCN. We therefore expect this "low-temperature" production of HCN to occur on Titan as meteoroids shock its atmosphere.

Rao finds the dissociation energy for methane in the equation $CH_4 \rightarrow CH_2 + H_2$ to be 81 kcal/mole, less than the dissociation energy of O_2. Production of HCN is unlikely to result from N_2 dissociation unless temperatures reach above 4000 K. Rao finds that even at 5000 K, only 0.1% of the initial N_2 is dissociated to N atoms, but nevertheless 10% of the initial N_2 is incorporated into HCN. This is because of a Zel'dovich-like mechanism, in which a series of reactions between N_2* and various hydrocarbons and their radicals drive HCN formation for energies well below those required to dissociate N_2 alone. These include reactions such as $CH_2 + N_2^* \rightarrow CH + H + N_2$ (128 kcal/mole) and $CH + N_2^* \rightarrow HCN + N$. The activation energy for this last reaction has been determined in shock-tube experiments at temperatures between 2340 K and 4660 K to lie between 14 kcal/mole and 22 kcal/mole (Dean et al., 1991; Lindackers et al., 1991; Medhurst et al., 1993). There is therefore no surprise that in N_2/CH_4 atmospheres, shock heating produces HCN at temperatures as low as 2500 K, and hydrocarbons at even lower temperatures. At temperatures above 5000 K, HCN production will increasingly be due to reactions with single N atoms, such as $CH_4 + N \rightarrow HCN + H_2 + H$ and analogous equations with CH_4 fragments (Ferus et al., 2017).

To calculate total yields of HCN and hydrocarbons in Titan's atmosphere, we need production efficiencies ϕ_i (in molecules J^{-1}) for each of the ith species produced. At 4000 K, HCN production in Rao's shock-tube experiment corresponds to a production efficiency $\phi_{HCN} = 2.0 \times 10^{17}$ molecule J^{-1} (Rao, 1967; Bar-Nun & Shaviv, 1975). It is encouraging that this same production efficiency results from a thermochemical-hydrodynamic model of shock heating due to a linear energy discharge based on Lin's cylindrical shock modeling for an N_2/CH_4 atmosphere: for this theoretical model, HCN production efficiency $\phi_{HCN} = 1 \times 10^{17}$ molecules J^{-1} for an assumed linear energy deposition $E_0 = 10^5$ J m^{-1} and an N_2/CH_4 ratio of 4.3% CH_4 (Chameides & Walker, 1981; Borucki et al., 1988). Production efficiency depends only weakly and indirectly on E_0 with the variation due to changes in T_F (which weakly depends on E_0). Chameides (1979) finds that production efficiency (molecules J^{-1}) varies by a factor of less than three as E_0 ranges from 1 J m^{-1} to 10^8 J m^{-1}. But he suggests

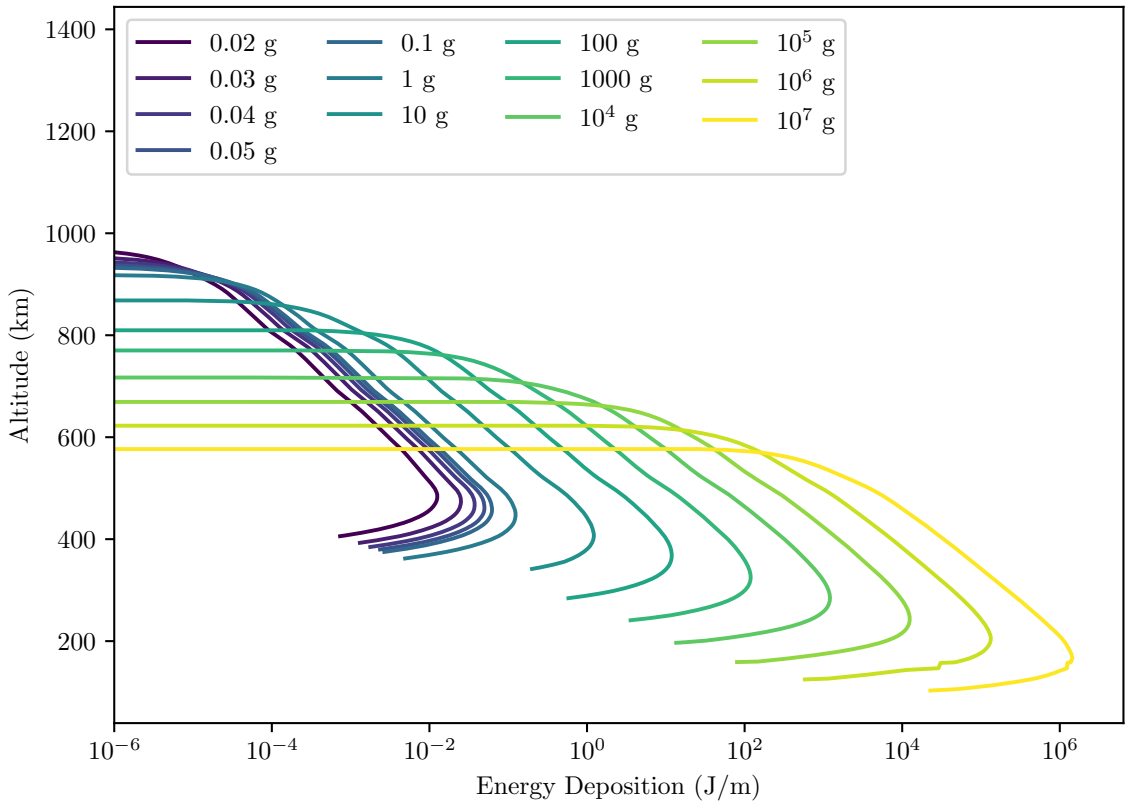

Figure 3.4: Energy deposition E_0 in J/m for individual meteoroids of a given mass descending through Titan's atmosphere.

that values of E_0 below 1 J m^{-1} produce temperatures too low for significant chemical yields, so we set this as our lower threshold for organic molecule production driven by shocks.

Figure 3.4 shows energy deposition in J m^{-1} for meteoroids with masses relevant to our discussion that enter, decelerate, and ablate in Titan's atmosphere. Meteoroids that enter with initial masses between 10 g and 10^7 g have maximum E_0 values ranging from 1 J m^{-1} to 10^6 J m^{-1}. Below, in evaluating Eq. 3.11 we will take R_1 and R_2 to be the radii corresponding to spherical particles of these masses.

As previously noted, other investigators have used laser-induced plasma (LIP) experiments with N_2/CH_4 gas mixtures to simulate the effect of meteoroids and lightning (each of which produces a cylindrical shock wave) in Titan's atmosphere (Borucki & McKay (1987); Scattergood et al. (1989); Ferus et al. (2017)). Borucki et al. (1988) and Scattergood et al. (1989) report results for a variety of $N_2/CH_4/H_2$ concentrations. The closest of these to observed Titan atmospheric conditions (95% N_2, 5% CH_4, 1 bar pressure) are those of Borucki *et al.*. Scattergood *et al.* show that results do not vary much for H_2 concentrations as high as 5%. Borucki & McKay (1987) report ϕ_i values for hydrogen cyanide (HCN), acetylene (C_2H_2), ethane (C_2H_4), ethylene (C_2H_6), and propane (C_3H_8), results that we have digitized from their published figures and summarized in Table 3.1. In Table 3.1, we compare the production ef-

Species	Thermochemical calculation[a]	Shock-tube[b]	Laser-induced plasma[c]
HCN	1×10^{17}	2.0×10^{17}	6.0×10^{16}
C_2H_2	-	7.1×10^{17}	6.2×10^{16}
C_2H_4	-	1.0×10^{17}	5.2×10^{15}
C_2H_6	-	-	4.5×10^{15}
C_3H_8	-	-	1.3×10^{14}

Table 3.1: Comparison of theoretical and experimental production efficiencies ϕ_i (molecules J^{-1}) for N_2/CH_4 gas mixtures.

Note. — [a]Assumes 10^5 J m^{-1} and 4.3% CH_4 atmosphere (Chameides & Walker, 1981; Borucki et al., 1988) [b]Results for 4000 K (Rao, 1967; Bar-Nun & Shaviv, 1975) [c]Assumes 5% CH_4 atmosphere Borucki et al. (1988)

ficiencies resulting from thermochemical-hydrodynamic calculations (Chameides & Walker, 1981; Borucki et al., 1988) with those derived from shock-tube (Rao, 1967) and LIP experiments (Borucki et al., 1988). We note that as temperatures in the shock-tube experiments approach 6000 K (results not displayed in Table 3.1 but tabulated by Bar-Nun & Shaviv (1975)), the relative abundances of HCN, H_2H_2, and C_2H_4, and therefore their relative production efficiencies, approach those shown for the LIP experiments. But in fact production efficiencies for HCN and are similar (within a factor of about 3) across the shock-tube, LIP, and calculated results. LIP experiments achieve higher temperatures from the laser-induced shock than reached in most of the shock-tube experiments reported here, which likely accounts for the different relative ϕ_i reported in Table 3.3. Borucki & McKay (1987) and Scattergood et al. (1989) do not report temperatures achieved in the laser-induced plasma of their experiments, but Ferus et al. (2017) determine plasma temperatures in their LIP experiments ranging from 4200 K to 9300 K.

3.5 Net Shock Synthesis in Titan's Atmosphere

Silber et al. (2017) estimate temperatures T' behind the cylindrical shock front of meteoroids entering Earth's atmosphere by relying on empirically derived equations for strong shocks that relate the shock wave's Mach number M to the pressure p' behind the shock and the temperature T_0 and pressure p_0 of the unshocked atmosphere (Zeldovich & Raizer (2002), Ch. 7):

$$\frac{p'}{p_0} = \frac{7}{6}M^2 - \frac{1}{6}; \tag{3.15}$$

and

$$\frac{T'}{T_0} = \frac{1}{36}(7 - M^{-2})(M^2 + 5). \tag{3.16}$$

Combining Eqs. 3.15 and 3.16 gives

$$T' = \frac{T_0}{6}\frac{p'}{p_0}\left[1 + 35\left(6\frac{p'}{p_0} + 1\right)^{-1}\right]. \tag{3.17}$$

Silber et al. (2017) note that Bronshten (1983) concludes that $10^2 \leq p'/p_0 \leq 10^4$ for meteoroids in Earth's atmosphere, and they choose $p'/p_0 = 100$. With this choice, Eq. 3.15 gives the Mach number of the shock to be $M = 9.3$ and Eq. 3.17 gives $T' = 17.6T_0$. By Eq. 3.11, the majority of useful shock energy delivered to Titan's atmosphere will be due to the smallest particles capable of generating shocks with energies above 1 J m^{-1}, or 10 g meteoroids. Fig. 3.4 shows that 10 g meteoroids at Titan deposit the bulk of their energy around 400 km altitude. We see in Fig. 1 that the temperature of Titan's undisturbed atmosphere at this altitude is about 180 K. Therefore for the Silber et al. (2017) choice of p'/p_0, the temperature behind the shock front reaches about 3200 K. This temperature is well above the threshold for HCN and hydrocarbon generation found in shock-tube experiments. We note, however, that a choice $p'/p_0 = 200$, still near the very bottom of the range found by Bronshten (1983), would yield a temperature of 6600 K, in the realm of temperatures achieved in laser-induced plasma experiments. We also note that Eqs. 3.15 and 3.16 assume a specific heat ratio $\gamma = 1.4$ (Zeldovich & Raizer, 2002) appropriate to a diatomic gas with two rotational degrees of freedom; including vibrational modes could lower γ, resulting in lower estimates for T' (Zucrow & Hoffman, 1976; Chameides, 1979). Because of this sensitivity to the choice of p'/p_0 and γ, we therefore choose not to rely on this method of estimating shock temperatures to determine the resulting chemistry, but instead approach the problem via the values of E_0 found in our meteoroid simulations shown in Fig. 3.4.

Of course no single experiment or calculation provides a perfect analogue to shock-driven chemistry in Titan's atmosphere. Nevertheless, it is encouraging that the values for ϕ_{HCN} in Table 3.1 are as consistent as they are, falling within a factor ~ 3 of one another. As previously noted, the majority of chemically useful shock energy delivered to Titan's atmosphere will be due to the smallest particles capable of generating shocks with energies above 1 J m^{-1}. Production efficiencies vary weakly with E_0, found in one calculation to drop by a factor of 2.3 as E_0 decreases from 10^5 J m^{-1} to 1 J m^{-1} (Chameides, 1979). To extrapolate from the ϕ_i values in Table 3.1 to those more appropriate for calculating the effects of these lower-energy cylindrical shocks, we therefore scale by a factor $f_\phi = 1/2.3 = 0.43$. It is likely that f_ϕ is species-dependent, but to our knowledge this level of detail is not currently available either in theoretical or experimental results for N_2/CH_4 atmospheres. In our subsequent calculations, we will use the thermochemical-hydrodynamic result in Table 3.1 for ϕ_{HCN}, scaled down in magnitude by the factor f_ϕ to account for the fact that the bulk of shock synthesis-relevant energy delivered by meteoroids to Titan's atmosphere lies in objects with values of E_0 as low as ~ 1 J m^{-1}. We then estimate shock production efficiencies ϕ_{C2H2} and ϕ_{C2H4} from the shock-tube results in Table 3.1, scaled down by a factor 2 by analogy to the ratio of the ϕ_{HCN} for the thermochemical-hydrodynamic

calculation vs. the 4000 K shock-tube results, multiplying these values as well by f_ϕ. These results, displayed in Table 3.2, provide the final production yield values we use in this study. We continue to carry two significant figures in Table 3.2 since these are intermediate values for our final calculations, but it should be clear from our discussion that these values are themselves reliable at best to one significant figure.

Species	$f_\phi \phi_i$ (molecules/J)
HCN	4.3×10^{16}
C_2H_2	1.5×10^{17}
C_2H_4	2.2×10^{15}

Table 3.2: Production yield values ($f_\phi \phi_i$) used in this study

With v_i from Eq. 3.3 and M_q from Eq. 3.11, the total energy flux into Titan's atmosphere from meteoroids in the size range R_1 to R_2 may be written

$$E_q = \frac{1}{2} M_q v_i^2, \tag{3.18}$$

where E_q has units J m^{-2} s^{-1}. The number of molecules of species i synthesized per m^2 per s due to meteor shocks in Titan's atmosphere may then be estimated as

$$N_{q,i} = f_\phi \phi_i E_q. \tag{3.19}$$

By Eqs. 3.11 and 3.18 with $b + 3 = -0.643$, E_q, and so $N_{q,i}$, is dominated by the smallest meteor size R_1 that can generate a shock in the atmosphere. We take this to be the radius corresponding to a spherical particle of mass $m = 10$ g with $\delta = 3.4$ g cm^{-3}. Using $R_1 = 8.9$ mm in Eq. 3.11 and $f_\phi \phi_i$ from Table 3.2, we calculate $N_{q,i}$ from Eq. 3.19 for $q = 3$ and $q = 4$. We compare these with production rates in Titan's atmosphere by UV photochemistry (Krasnopolsky, 2009) in Table 3.3. These column production rates are typically reported in the photochemistry literature in units of molecules cm^{-2} s^{-1} so we adopt these units for Table 3.3.

In Table 3.3 we also present results for H_2 production. The photochemistry result is again from Krasnopolsky. The results for shock production are not directly from experiment, but rather are estimated from the analysis of Civiš et al. (2017), for laser

Species	Photochemistry	Shocks (q=3)	Shocks (q=4)
HCN	1.2×10^9	3×10^7	8×10^4
C_2H_2	7.5×10^9	1×10^8	3×10^5
C_2H_4	2.7×10^9	2×10^6	4×10^3
H_2	1.2×10^{10}	2×10^8	6×10^5

Table 3.3: Column production rates (cm^{-2} s^{-1}) for HCN, hydrocarbons, and H_2 in Titan's atmosphere by UV photochemistry (from Krasnopolsky (2009), Table 6) compared with meteor shock production predicted here using the Tiscareno *et al.* meteoroid flux models with $q = 3$ and $q = 4$.

simulations of meteor shocks in N_2/CH_4 gases, with some mixtures also including D_2O. Absent D_2O, the overall formation of acetylene from methane can be described by the reaction $2CH_4 \rightarrow C_2H_2 + 2H_2$, and of hydrogen cyanide by $2CH_4 + N_2 \rightarrow 2HCN + H_2$. Since these are the two dominant products from the shock chemistry (see Table 3.3), these reactions allow us to make a first estimate of H_2 production via shocks.

Table 3.3 shows that for the case where $q = 3$ correctly models the ejecta distribution at Saturn's rings, meteor entry into Titan's atmosphere is responsible for $\sim 1\%$ as much production of HCN, C_2H_2, and H_2 as is photochemistry. These percentages are reduced by a factor of about 300 if $q = 4$ provides a better ejecta model. Given how carefully tuned photochemistry models are now compared with observed compositions for Titan's atmosphere (Hörst et al., 2018), these results imply that detailed Titan atmospheric organic chemistry models must henceforth take into account meteor shock production. This conclusion is only reinforced by a consideration of the altitude distribution of meteor shock synthesis.

3.6 Energy Deposition vs. Altitude

We showed in the previous section that meteoroid-shock-driven chemical synthesis likely makes a significant contribution to the production of organics and H_2 in Titan's atmosphere. We now describe the distribution of this production as a function of altitude.

First, we show that meteoric deposition of energy in Titan's atmosphere, and the resulting shock chemistry, has a very different distribution than the energy inputted into Titan's atmosphere by the other larger sources of chemistry-driving exogenous energy incident upon Titan's atmosphere, UV photons and magnetospheric ions. We take cumulative flux from the Tiscareno models together with our model results of meteoroid deceleration and ablation through Titan's atmosphere to calculate the total atmospheric energy deposition in J/km from meteors for one saturnian year (29 Earth years). Using the photochemical model in Krasnopolsky (2009), we show in Fig. 5 the total energy deposition of UV photons with wavelengths between 90 – 100 nm and 120 – 130 nm. Photons in this wavelength range are primarily responsible for N_2 and CH_4 photodissociation, respectively (see Fig. 2 in Hörst et al. (2018)). Smith et al. (2009) provide measurements of the H^+ flux onto Titan from the Cassini magnetospheric imaging instrument's (MIMI) ion-neutral camera (INCA) (Krimigis et al., 2004a). Although there are many ion species in Saturn's magnetosphere, H^+ ions dominate in the outer portion that Titan moves through (Young et al., 2005). We present the energy input by H^+ in Titan's atmosphere in Fig. 3.5 (Krimigis et al., 2004a). In all cases, we determine energy deposition by simply calculating the change in energy over altitude.

Quantitative results again depend on the correct choice of q in the Tiscareno *et al.* ejecta model, but in the $q = 3$ model, we see that meteoric injection of energy exceeds that of magnetospheric protons and even that of 90 – 100 nm UV light. Regardless of the choice of q, meteoroids deposit their energy–and therefore drive atmospheric

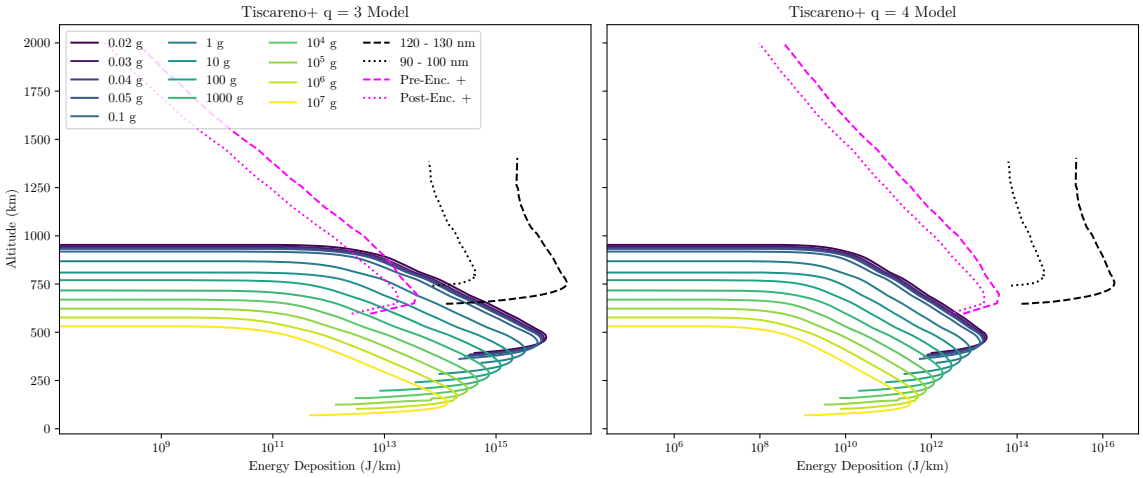

Figure 3.5: Comparison of the energy deposition in Titan's atmosphere due to all meteors hitting Titan's atmosphere in one saturnian year (with flux distribution as described by the Tiscareno *et al.* model for $q = 3$ and $q = 4$; see text), compared to the energy deposition from magnetospheric H^+ measured by the Cassini MIMI INCA instrument pre- and post-encounter with a Titan flyby (Smith et al., 2009; Krimigis et al., 2004a), and the energy deposition from UV photons as modeled by Krasnopolsky (2009), also in one saturnian year. All curves shown should, at their lowest altitude, be understood to continue roughly horizontally to lower energies at the left of the figure.

chemistry–hundreds of kilometers below energy deposition by UV and protons, so that meteoroids appear to be the dominant source of chemistry-driving exogenous energy between about 250 and 600 km in altitude.

Since the efficiency of organic synthesis by shocks is often as high or higher than that for UV (Chyba & Sagan, 1992), this result should hold for exogenously driven organic synthesis as well. In Fig. 3.6, we show results from this simple model for the production of C_2H_2 and HCN per kilometer over a Saturnian year, by combining the results of Fig. 3.5 with the efficiencies shown in Table 3.2. At and below roughly 550 km in altitude, production of HCN and C_2H_2 is, dominated by meteoroid shock energy as UV photons and magnetospheric ions cannot penetrate the atmosphere as deeply. It is striking that this altitude broadly coincides with the presence of an observed haze layer. If $q = 3$, meteors deposit more energy than the magnetospheric H^+ ions and photons in some cases, while even for $q = 4$ they come within an order of magnitude of the H^+ energy deposition rate.

3.7 Conclusion

In this study we have presented a model for meteoroid-driven organic chemistry in Titan's atmosphere, calculating total resulting yields for hydrogen cyanide, acetylene, and ethane, as well as an implied resulting yield for molecular hydrogen. In order for

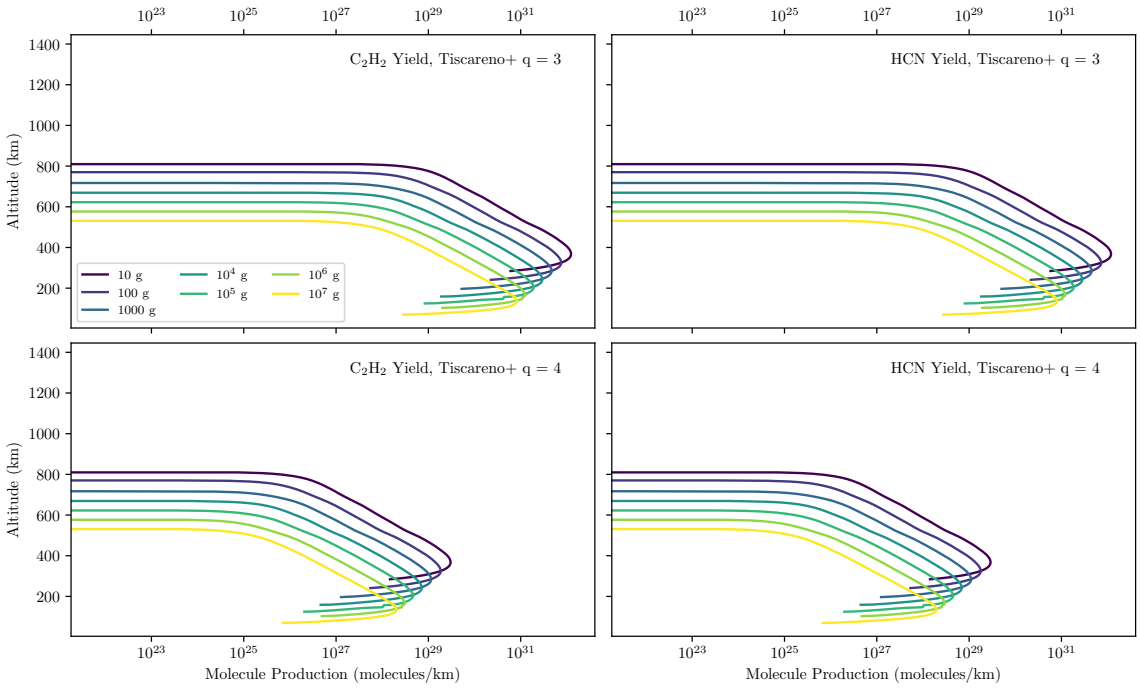

Figure 3.6: Number of molecules per kilometer produced by the energy generated from meteoroids shocking Titan's atmosphere for the $q = 3$ and $Q = 4$ Tiscareno *et al.* flux cases, for one saturnian year.

an entering particle to shock Titan's atmosphere to a temperature sufficient to drive the relevant chemistry, the particle needs to satisfy several criteria. First, it needs to be big enough so that the size of its vapor cap (much larger than the particle's physical diameter) is larger than an atmospheric molecule's mean free path–a comparison that of course depends on altitude in the atmosphere. Our Knudsen-number analysis, coupled with an atmospheric entry model, led us to conclude via Fig. 3.3 that shocks can be generated in Titan's atmosphere by meteoroids with masses ≥ 0.02 g.

Second, we made use of our meteoroid atmospheric entry simulations to determine energy deposition (J/m) in the atmosphere over the course of the meteoroids trajectory as that object decelerates and ablates. We drew on previous work modeling the nitrogen- and carbon-based chemistry that occurs in N_2/CH_4 atmospheres as a result of linear shocks caused by meteoroid trajectories. We concluded that a meteoroid would need to deposit at least 1 J/m, corresponding to masses at and above 10 g, to drive such chemistry.

It is possible to estimate the flux of object larger than 10 g entering Titan's atmosphere due to observations made by the Cassini spacecraft of apparent meteoroid strikes on Saturn's rings (Tiscareno et al., 2013). We used these results, albeit with a difference choice of meteoroid density, to determine net energy deposition as a function of altitude in Titan's atmosphere. The close agreement of thermochemical simulation results (Chameides & Walker, 1981) and experimental shock-tube results (Rao, 1966, 1967) for N_2CH_4 atmospheres then allowed us to estimate HCN, C_2H_2,

C_2H_4, and H_2 production as a function of altitude in Titan's atmosphere. We found that meteoroid-driven production of these molecules appears to be the dominant source for these molecules below roughly 550 km in Titan's atmosphere, an entirely new result. Moreover, net production by meteoroid shocks in the atmosphere could reach as high as $\sim 1\%$ of photochemical production for these molecules, although that result is dependent on one's choice of the fragmentation parameter q in Tiscareno et al.'s models for observations of impacts on Saturn's rings (Tiscareno et al., 2013).

Our model is simple for several reasons. We have used average meteoroid velocities, ignoring the impact-velocity asymmetry between the leading and trailing faces of Titan. We have taken the N_2/CH_4 ratio of Titan's atmosphere to be constant with altitude. And while we have used the thermochemical and shock-tube data available in the literature, and noted that these seem appropriate in light of their relation to the more-extensive laser-induced plasma results, one can certainly wish that there were a more extensive set of both modeling and experimental data exploring a wider range of atmospheric compositions, linear energy depositions, and shock temperatures. In future work we hope to relax at least some of these assumptions, while recognizing that considerable uncertainty will remain until there are additional spacecraft data addressing the flux of meteoroids more massive than 10 g in the vicinity of Saturn.

Appendix

3.A Definitions of Symbols

Variable	Description	Equation
v_{Sesc}	Saturn escape velocity	3.1
v_{Tesc}	Titan escape velocity	3.3
r	Distance from Saturn	3.1
Φ_q	Meteoroid flux	3.7
R	Radius of particle	3.7
M_q	Mass flux	3.10
λ	Mean free path	3.12
E	Energy	3.13
z	Altitude	3.13
p'	Pressure behind shock	3.15
p_0	Pressure in unshocked atmosphere	3.15
T'	Temperature behind shock	3.16
T_0	Pressure in unshocked atmosphere	3.16
$N_{q,i}$	Number of molecules synthesized	3.19

Table 3.4: Descriptions of symbols with location of first appearance

3.B Numerical Constants

Symbol	Description	Value	Equation
v_{inf}	Velocity at infinity	16 km/s	3.1
M_S	Mass of Saturn	5.68×10^{26} kg	3.2
v_i	Initial velocity	18 m/s	3.3
v_{inf}	Velocity at infinity	16 km/s	3.3
a_q	Flux coefficient	1.48×10^{-19} (optimistic) 3.63×10^{-22} (conservative)	3.6
b	Flux exponential	-3.643	3.6
f_T	Gravitational focusing factor at Titan	1.1	3.10
f_{inf}	Gravitational focusing factor at infinity	0.19	3.10
Λ	Heat transfer coefficient	0.5	3.14
Γ	Drag coefficient	1	3.14
L	Heat of ablation	8.1×10^{10} erg/g	3.14
M	Mach number	9.3	3.15

Table 3.5: Values for constants

Chapter 4

TitanWRF

4.1 Introduction

Over the last couple of decades, general circulation models (GCMs) have gained prevalence in planetary and exoplanetary studies, but generally speaking these models are skewed towards gaseous planets as opposed to terrestrial ones. It is incredibly difficult to incorporate all of the processes that drive atmospheric dynamics on Titan - subsurface heat transfer, surface-atmosphere interactions at the planetary boundary layer, moisture transport in the methane cycle, photochemistry in the upper portions of the atmosphere, and so forth. A handful of models, in 1-, 2-, and 3-D have been developed over the years for Titan, mostly as modifications on Earth GCMs. They all have varying degrees of realism, incorporating a combination of physical aspects of Titan. With varying degrees of realism though, there are varying degrees at successfully reproducing observations. For this chapter, I will review the handful of Titan GCMs that currently exist, particularly focusing on the TitanWRF GCM I worked with for several studies that are part of this thesis. It is, in my opinion, one of the most "complete" of the Titan GCMs.

In Section 4.2 I will describe the history and current state of Titan GCMs today, and in Section 4.3 I will describe the GCM I worked with for this thesis, including my own improvements and criticisms that are part of a forthcoming publication.

4.2 State of Titan GCMs

4.2.1 Laboratoire de Météorologie Dynamique's GCM

The first Titan GCM was produced at Laboratoire de Météorologie Dynamique (I will refer to it as LMD GCM) (Hourdin et al., 1995), and in many ways modern GCMs are still trying to reproduce its results. Prior to this study, there had been attempts to create GCMs for terrestrial worlds from Earth GCMs (e.g., the NASA GISS model Somerville et al. (1974); Stone et al. (1977)), usually to study the Martian climate (e.g., Pollack et al. (1981); Barnes et al. (1993)), though there had been attempts at modeling Venus's atmosphere (e.g., Young & Pollack (1977)). Hourdin

et al. were the first group to develop a computational model for Titan's atmosphere. Previously, they had developed GCMs for Mars (Hourdin et al., 1993) and a general version that allowed one to describe a terrestrial planet in 19 parameters (Hourdin & Talagrand, 1992). As nearly all following GCMs use the same or similar mathematical frameworks, I will spend a little time describing them. These planetary GCMs were created from a code that LMD had developed previously to study Earth's climate, based on the six primitive equations of meteorology:

Conservation of Mass

$$\begin{aligned} 0 &= \frac{\partial \rho}{\partial t} + \nabla \cdot (\rho \mathbf{U}) \\ &= \frac{\partial \rho}{\partial t} \delta x \delta y \delta z \\ &+ \Big[\frac{\partial (\rho u)}{\partial x} + \frac{\partial (\rho u)}{\partial y} + \frac{\partial (\rho u)}{\partial z} \Big] \delta x \delta y \delta z \end{aligned} \tag{4.1}$$

Conservation of Momentum

$$\begin{aligned} \frac{D\mathbf{U}}{Dt} &= 2\mathbf{\Omega} \times \mathbf{U} - \frac{1}{\rho} \nabla P + \mathbf{g}_{eff} + \mathbf{F}_f \\ &= \Big(\frac{Du}{Dt} - \frac{uv \tan \phi}{a} + \frac{uw}{a} \Big) \hat{\mathbf{i}} \\ &+ \Big(\frac{Dv}{Dt} + \frac{u^2 \tan \phi}{a} + \frac{uw}{a} \Big) \hat{\mathbf{j}} \\ &+ \Big(\frac{Dw}{Dt} - \frac{u^2 + v^2}{a} \Big) \hat{\mathbf{k}} \end{aligned} \tag{4.2}$$

The terms can be rewritten using the definition of the vector cross product and expanding the Coriolis term $2\Omega \times U$ and expanding Ω in terms of unit vectors. The final form of the conservation of momentum equation is thus:

$$\begin{aligned} \frac{D\mathbf{U}}{Dt} &= \Big(-\frac{1}{\rho} \frac{\partial P}{\partial x} + 2\Omega v \sin \phi - 2\Omega w cos\phi + F_{\mathrm{fx}} \Big) \hat{\mathbf{i}} \text{ (eastward comp. of momentum)} \\ &= \Big(-\frac{1}{\rho} \frac{\partial P}{\partial y} - 2\Omega u \sin \phi + F_{\mathrm{fy}} \Big) \hat{\mathbf{j}} \text{ (northward comp. of momentum)} \\ &= \Big(-\frac{1}{\rho} \frac{\partial P}{\partial z} - \mathbf{g}_{eff} + 2\Omega u \cos \phi + F_{\mathrm{fz}} \Big) \hat{\mathbf{k}} \text{ (vertical comp. of momentum)} \end{aligned} \tag{4.3}$$

Conservation of Energy

$$\frac{\partial T}{\partial t} = -\frac{1}{\rho c_p} \frac{\Delta F(z)}{\Delta z} \tag{4.4}$$

These equations determine large-scale physics in this, and most (if not all) computational models of planetary atmospheres. In the LMD GCM, they implement a finite difference method as described in Sadourny & Laval (1982) to solve for these equa-

tions in 3-D. They spatially discretize the equations on a staggered latitude-longitude Arawaka C-grid (Arakawa & Lamb, 1981) in order to preserve the mass, potential temperature, potential vorticity, and angular momentum. Conservation of angular momentum in particular is important to guarantee that any superrotation generated in the model is not a numerical artifact.

They ran this model at two resolutions: a low resolution 32 × 24 and a high resolution 64 × 48 in longitude and latitude respectively. In both cases, there were 55 vertical σ levels, which are pressure normalized to the surface pressure value. On average, these layers were roughly 2.5 km thick near the surface, and were 9km thick at the model. Their model only reached $\sim$ 300 km above the surface, Titan's stratosphere. The dynamics were calculated in 400-second time steps for the lower resolution model, and 180-second time steps for the higher resolution model.

In this and all GCMs, horizontal dissipation of energy must be properly modeled to account for nonlinear interactions at large, resolved scales and at small, unresolved scales, and to avoid dynamic instabilities in the model, although it is not physically motivated. This is handled by the Laplacian:

$$\frac{\partial}{\partial t} = (-1)^{n_{diss}} \frac{1}{\tau_{diss}} \delta x^{2n_{diss}} \Delta^{n_{diss}} \tag{4.5}$$

The values for n_{diss} and τ_{diss} (see Table 4.2 for the definitions) are set to a time longer than 10,000 Titan days in the simulation, though these values will vary depending on the resolution of the model.

Titan's thick atmosphere strongly absorbs and reflects most of the sun's radiation. Haze particles absorb 40%, 30% is reflected off the top of the atmosphere, and 30% reaches the troposphere. Radiation transfer in the LMD model is a two-stream approximation (radiation from above and below, in infrared and visible light) as described by Toon et al. (1989), computed with code developed for Titan by McKay et al. (1989) known as the Titan Greenhouse Model (TGM). The TGM is a microphysical model that calculates the distribution of opacity in Titan's atmosphere. For radiative transfer in a 2D scattering atmosphere, how the intensity of radiation changes as a function of optical depth is described by the equation (as per Toon et al. (1989)):

$$\begin{aligned} \mu \frac{\partial I_\nu}{\partial \tau_\nu}(\tau_\nu, \mu, \phi) = I_\nu(\tau_\nu, \mu, \phi) - S_\nu(\tau_\nu, \mu, \phi) - \frac{\omega_{0\nu}}{4\pi} \\ \cdot \int_0^{2\pi} \int_{-1}^{1} P_\nu(\mu, \mu', \phi, \phi') d\mu' d\phi' \end{aligned} \tag{4.6}$$

The two-stream radiation is then calculated by relating the intensity differential to the flux differential from above (-) and below (+) by the relation:

$$\begin{aligned}\frac{\partial F_\nu^\pm}{\tau_\nu} = \pm \int_0^1 I_\nu^\pm(\tau_\nu, \mu) d\mu \mp \frac{1}{2} \int_0^1 \int_{-1}^1 P_\nu(\mu, \mu') \\ \cdot I_\nu^\pm(\tau_\nu, \mu') d\mu d\mu' \mp \int_0^{2\pi} \int_0^1 S_\nu(\tau_\nu) d\mu' d\phi'\end{aligned} \tag{4.7}$$

The solution for the two fluxes for each atmospheric layer n is:

$$\begin{aligned}F_n^+(\tau) &= k_{1n} \exp(\lambda_n \tau) + \Gamma_n k_{2n} \exp(\lambda_n \tau) + C_n^+(\tau) \\ F_n^-(\tau) &= \Gamma_n k_{1n} \exp(\lambda_n \tau) + k_{2n} \exp(-\lambda_n \tau) + C_n^-(\tau)\end{aligned} \tag{4.8}$$

The constants k_1 and k_2 will depend on the boundary conditions, and λ and Γ depend on the form of the two-stream equation. There are a variety of tunable parameters to simulate haze (which absorbs and scatters the optical radiation in the upper atmosphere), the mixing ratio of known molecular species at the time, and observed properties of Titan's atmosphere. The main sources of opacity are N_2, H_2, and light hydrocarbons (mainly acetylene, ethane, and methane) that cause collision-induced absorption in a greenhouse effect, and the abundant organic species (methane again and haze particles) that absorb solar radiation in an antigreenhouse effect.

Finally, turbulent mixing is calculated in the model by the equation:

$$\frac{\partial}{\partial t} = \frac{1}{\rho} \frac{\partial}{\partial z} \left(\rho K_z \frac{\partial}{\partial z} \right) \tag{4.9}$$

where $K_z = l \exp 1/2$ and e scales with the Richardson number:

$$\mathrm{Ri} = \frac{g \partial \rho / \partial z}{\rho (\partial u / \partial z)^2} \tag{4.10}$$

which is the ratio between the buoyancy and flow shear of the fluid.

With this computational model setup, the LMD team tested two models: a quick 2D model before the main 3D model, the first of its kind. They run the 3D model over 30 Titan years (at the lower resolution), and they write that "(t)he most remarkable result of this first simulation is the fact that the circulation, after a long spin-up phase, reaches a regime of strong superrotation." After a spin-up phase that lasts 23 Titan years, the stratosphere rotates significantly faster than the atmosphere at rest. They define a superrotation index μ that is the ratio of angular momentum of the layer(s) of the atmosphere of interest ($a \cos\phi (u + a\Omega \cos\phi)$) to the total angular momentum of the atmosphere at rest ($2/3a^2\Omega$). Their plot of μ vs. time is shown in Figure 4.1. They force a steady-state by taking the results at the end of year 23 and increasing the winds by 25%, and after roughly 7 years the model stabilizes at $\mu \sim 7.5$.

The small-scale oscillations in the plot correspond to seasonal variations - minima correspond to the solstice-equinox transition, and maxima correspond to the equinox-

solstice transition. Angular momentum is transferred seasonally between the poles and equator. The circulation of energy on Titan - as on Earth - is dominated by Hadley circulation, with warmer air rising from the equator, flowing poleward and cooling, descending at the poles, and returning to the equator. Near solstice, there is a downward transfer of angular momentum and the superrotation stops increasing in the atmosphere. Near equinox, there is an upward transfer of angular momentum, and the superrotation increases in the atmosphere. Large scale eddies are what transport the angular momentum in both seasons, and the model produces zonal winds on order 100 m/s at the 1-mbar pressure level and 20 m/s at the 20-mbar pressure level. Although at the time the Hourdin publication there were no direct observations of Titan's zonal winds, this was consistent with values derived from a stellar occultation measurement, described in Hubbard et al. (1993). Their wind velocity results would later be compared with observations from Cassini and follow-up ground observations (which will be discussed later), and shown to be an underestimate in the stratosphere and an overestimate in the troposphere.

I will note that the IPSL-LMDZ (Lebonnois et al., 2012) is a 3-D successor of the LMD. Rannou et al. (2002, 2004b) took the original model and incorporated coupled haze physics and the updated photochemical model of Lebonnois et al. (2001), creating what they term the 2-D IPSL model. Citing an "increase in computer power" over the decade since the 2-D IPSL model, Lebonnois et al. (2012) created a 3-D version of the 2-D IPSL model with an updated dynamical core, the LMDZ4 (Hourdin et al., 2006; Lebonnois et al., 2010). There are not significant differences in the results of these models (the 2-D LMD, the 2-D IPSL, and the 3-D IPSL-LMDZ) to merit an entire section. The most notable improvement of this 3-D study over the preceding 2-D studies is the comparison to Cassini-Huygens data, which had not been available at the publication time of the previous two model iterations. Even with upgrades to the model that incorporate more realism, the results do not differ drastically from the 2-D cases, and the same discrepancies between what is observed and what is modeled persist.

4.2.2 Cologne GCM

The second 3D GCM of Titan's atmosphere was developed at the Institute for Geophysics and Meteorology, University of Cologne by Tokano et al. (1999). Theirs would be the first attempt to reproduce the Hourdin et al. (1995) superrotation results, while also retrieving a temperature profile that was more consistent with observations. This also would be the first model to include the main and detached haze layers below 200 km and above 300 km respectively. A year after the LMD results were published, Hutzell et al. (1996) published results from the first 2D haze model that Tokano *et al.* were able to incorporate in their model. Recent observations of Titan had also revealed seasonal variability of the haze particles' distribution (Karkoschka & Lorenz, 1997; Lorenz et al., 1997; Gibbard et al., 1999), an additional focus for the Tokano *et al.* study.

The GCM does the standard calculation of solving the primitive equations of meteorology. Its dynamical core is from the ARIES/GEOS GCM Version 2 from

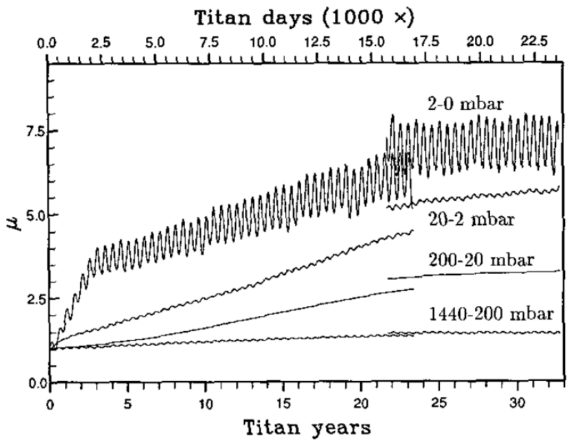

Figure 4.1: Figure 3 from Hourdin et al. (1995) showing how the superrotation index μ varies with time for the troposphere (1440 - 200 mbar), tropopause (200 - 20 mbar), lower stratosphere (20 - 2 mbar), and upper stratosphere at the model top (2 - 0 mbar).

NASA GSFC (Suarez & Takacs, 1995), which utilizes a staggered latitude-longitude C-grid. The resolution of this model is 24 × 32 in latitude and longitude, with 30 vertical layers. The vertical coordinate $\sigma = P/\pi$ where P is the pressure and π is a dynamic surface pressure that changes by mass convergence/divergence:

$$\frac{\partial \pi}{\partial t} = -\sum_{k'=1}^{KM} \nabla \cdot (\pi \mathbf{v}_{k'})(\delta\sigma)_{k'} \tag{4.11}$$

where KM is the total number of layers k'. The addition of haze particles is modeled as a continuity equation for number density (in cm^{-3}):

$$\frac{\partial(\pi n)}{\partial t} = -\nabla_\sigma \cdot (\pi \mathbf{v} n) - \frac{\partial(\pi \dot{\sigma} n)}{\partial \sigma} \tag{4.12}$$

The haze layer is between $z = 300$ and 30 km in the model, but the opacity distribution was run as either latitudinally varied or uniform.

This study also utilizes the McKay et al. (1989) code used in Hourdin & Talagrand (1992); Hourdin et al. (1995) (and many other GCMs going forward) to calculate the two-stream radiative transfer. At the surface, the temperature is held constant over time at every latitude ϕ, at $T_g = 95\,\mathrm{K} - 5\,\mathrm{K}|\sin\phi|$ (Flasar et al., 1981). In order to calculate the insolation, the model utilizes algorithms from Davies et al. (1992) and Olson et al. (1995) to generate the astronomical parameters as a function of Julian date. This allows the model to take into account the variation in diurnal solar heating, the large eccentricity of Saturn's orbit, and the variation in insolation at the top of Titan's atmosphere.

In many ways it is similar to the Hourdin et al. (1995) model, but it differs in terms of numerical scheme, vertical resolution, treatment of subgrid-scale physics, and handling of ground temperature.

The model was run in 5 cases: 2 control cases that were just calculating the radiative transfer (with no atmospheric dynamics) and 3 full GCM cases that varied atmospheric conditions. The 2 control cases were the aforementioned varying and uniform haze cases. In the uniform haze case, their results are consistent with those of Hourdin et al. (1995) and Voyager 1 and 2 measurements (Flasar et al., 1981; Letourneur & Coustenis, 1993; Coustenis & Bezard, 1995), though the results for the Northern heating rate lag behind the solar cycle, and the observed temperature asymmetry is not reproduced. They test a varying haze opacity case by varying the number density of haze particles to try to reproduce the observed North-South haze albedo asymmetry (see Figure 1.4). There were several including temporal variations in particle composition (Allen et al., 1980), solar UV output (Pollack et al., 1980), size and distribution (Toon et al., 1992), and seasonal wind variability (Hutzell et al., 1996). Ultimately, they do not reproduce the observed haze asymmetry in a model that does not include atmospheric dynamics.

The 3 full GCM cases consisted of one control case that had constant opacity, one with a modified cooling rate, and one with reduced meridional circulation in order to try to reproduce observed features (haze asymmetry and superrotating stratospheric jet) of Titan's atmosphere and understand the mechanisms behind those features. In the constant opacity case, haze particles are transported in three dimensions, but they are not coupled to radiative processes. They fail to reproduce the observed stratospheric jet due to excessive meridional circulation transporting angular momentum away from the equatorial region where the jet is observed towards higher latitudes. This model also does not reproduce the observed haze asymmetry, as the meridional circulation produces a pair of symmetric Hadley cells with the same heating rate, which disallows asymmetric heating of the haze particles (that are also transported symmetrically to both hemispheres). In the modified cooling rate model, they attempt to account for the observed distribution of nitriles and some hydrocarbons that favors the spring pole. They do this by forcing a net positive heating rate in the southern hemisphere during the vernal equinox, delaying the meridional cell turnover and subsequent heat transport. This does reproduce an asymmetry in the haze opacities of the northern and southern hemisphere at equinoxes (as observed). In the final test, they limit the meridional circulation in order to mitigate the effects the excess circulation had on stunting the growth of the stratospheric superrotating jet. Although they were able to generate superrotating jets at high latitudes, this model failed to reproduce the observed equatorial jet. The Cologne GCM ultimately proved that one needs to couple haze dynamics and chemistry, radiative processes, and bulk atmospheric dynamical processes in order to recreate observed phenomena.

4.2.3 Titan Community Atmosphere Model

Titan CAM (Friedson et al., 2009) is a 3D GCM that was developed from the National Center for Atmospheric Research (NCAR)'s Community Atmosphere Model Version 3 (CAM3) (Collins et al., 2006). NCAR CAM is a publicly available Earth model for atmospheric studies. It is currently in V6 and still used widely today to study the Earth's atmosphere and climate patterns. It incorporates many physical processes

(some standard amongst GCMs and others not) including "forcing by Saturn's gravitational tide (Tokano & Neubauer, 2002); turbulent diffusion; parameterization of the planetary boundary layer and surface layer; scattering and absorption of short-wave radiation; absorption and emission of long-wave emission; and heat conduction in the soil (Friedson et al., 2009)."

Titan CAM uses a finite volume algorithm (CAM3 allows the user to choose between three different dynamical cores), which is based on the Flux-Form Semi-Lagrangian scheme from Lin (2004). The model is run at a relatively low resolution of 10×15 degrees in latitude by longitude respectively during the spin-up phase (for computational efficiency) and 61 Eulerian vertical layers. This is a hybridization of a vertical coordinate that follows the surface topography and one that follows layers of constant pressure in the atmosphere. The model top is at ~ 400 km, encompassing the entire stratosphere. The radiation transfer is handled by a two-stream direct-integration algorithm to calculate the effects of short-wave ($\lambda < 5\mu$m) radiation, and a two-stream δ-Eddington approximation (Briegleb, 1992) to calculate the effects of scattering. The flux that Titan receives is calculated as a function of latitude and longitude, and they account for diurnal heating variations, although they do ignore the effects of Titan passing through Saturn's shadow. For the first time in a 3D study, they are able to incorporate atmospheric data from the Cassini mission. The model uses the observed methane profile, and the mixing ratios for detected molecular species at the time.

Aerosols in this model are assumed to be uniform, but the atmospheric extinction, single scattering albedo, and phase function vary as a function with altitude. There are three distinct aerosol types distributed uniformly between the surface and 80 km. The photochemical model they incorporate is from the 1D model of Wilson & Atreya (2004), and it includes 37 hydrocarbons (14 advected species, 24 non-advected radicals) with 85 chemical reactions. The chosen species and reactions are those that are known to absorb and/or photochemically react with the wavelengths that are able to penetrate Titan's atmosphere, as well as those that are profile-determining species.

The planetary boundary layer (PBL; the area of the atmosphere directly affected by the surface) scheme and turbulent diffusion are basically unchanged from the Earth model, but how it models the surface and subsurface is slightly modified to emulate what was assumed about Titan's surface composition at the time from albedo measurements. The surface is heated by both shortwave radiation and thermal radiation, and it is cooled through thermal emission. Heat is transferred between the 20 soil layers by conduction. They assume that the surface is comprised of porous regolith, setting the thermal inertia to 335 J m^{-2} s$^{-1/2}$ K^{-1} and the emissivity to 0.86. Surface-atmosphere interactions are governed by the Monin-Obukhov similarity theory, a universal framework to describe the interactions between the average flow and temperature in a surface that is under non-neutral conditions (like the ground under a turbulent atmosphere). Collins et al. (2004) describe the mathematics behind this theory in detail in the technical report for CAM3. To summarize, the velocity, temperature, and humidity of the surface layer are described by dimensionless parameters u^*, θ^*, and q^* respectively. The vertical dimension is also dimensionless, and the profiles of each of the parameters are defined by universal shape functions $\zeta = z/L$,

where z is the height parameter, and L is the characteristic Monin-Obuknov length. Some values in their model are empirically determined for the Earth model, and they keep them for Titan with only small modifications.

Although Titan CAM produced results consistent with the Cologne and Caltech (aka planetWRF (Richardson et al., 2007), to be discussed in the final section of this chapter) models, it failed to reproduce the stratospheric superrotation that was in the LMD model and in observations. Winds only reached maximum speeds of roughly 10 m/s. They did generate seasonal Hadley circulation like the LMD, but the polar jet produced was significantly weaker. The minimum in this cycle happened in the model near $L_s = 330°$, which was in agreement with Cassini RADAR measurements (Stiles et al., 2008), suggesting that Titan's rotation rate could be changing even over the relatively short timescale of the Cassini mission. Atmospheric angular momentum could be being transferred to the surface, but at the time they did not have measurements to prove this conjecture. Tomasko et al. (2005) had previously predicted that Titan's rotation rate was increasing, and they suggested that the icy surface layer might be decoupled from what could be an interior ocean. Titan CAM's results further supported this theory, although the authors note that it is possible that imperfections and omissions in their model could explain the calculated angular momentum transfer. Ultimately, even though Titan CAM also failed at reproducing observed atmospheric dynamics, it did lead to interesting questions about the exchange of energy and angular momentum between the atmosphere, surface, and even subsurface.

4.2.4 Titan Atmospheric Model

The Titan Atmospheric Model (TAM) by Lora et al. (2015) is one of the most recent 3D GCMs to enter the Titan market. Its dynamic core is the Geophysical Fluid Dynamics Laboratory's (GFDL) Flexible Modeling System (FMS) (Gordon & Stern, 1982). The FMS is a spectral transform model (Orszag, 1970; Eliasen et al., 1970; Orszag, 1971; Bourke, 1972), which is a model in which field variables are represented as finite sums of spectral modes (such as Fourier modes or spherical harmonics) as opposed to grid points, and the nonlinear terms in the variables are transformed and calculated in physical space at every time step before being transformed back to the spectra space to be applied to the evolution of the model. This type of model is a more efficient alternative to non-staggered grid point models (Daley et al., 1976), but they have several drawbacks such as being unable to resolve small-scale processes as well as grid-point models and having difficulty handling schemes with periodic boundary conditions. The Lora et al. (2015) study runs the model at two resolutions, L32 ($\sim 5.6°$ in the horizontal and 32 vertical layers) and L50 ($\sim 5.6°$ in the horizontal again and 50 vertical layers).

The two-stream, nongray radiation transfer model is from Toon et al. (1989); Briegleb (1992), though they do not use the McKay et al. (1989) code, and it does include seasonal and diurnal insolation variations. The methane opacity is calculated using correlated-k coefficients from HITRAN (Rothman et al., 2009), and the global methane profile is set to the observed profile from Huygens (Niemann et al., 2005).

The haze is modeled as horizontally homogeneous, perfectly absorbing in the IR, and following a power law fit in the optical (Tomasko et al., 2008).

TAM is the second model to include the effects of evaporation and precipitation of methane (no clouds/cloud formation, and no ethane) in the radiative transfer. There are two precipitation schemes: a large-scale condensation scheme (Frierson, 2007) and a quasi-equilibrium convection scheme (O'Gorman & Schneider, 2008). In the former, methane molecules are allowed to condense when their grid box exceeds 100% relative humidity and then re-evaporate in underlying layers. In the later, unstable columns relax towards a moist pseudoadiabat, and the liquid rains immediately to the surface.

The surface-atmosphere boundary layer is described by the Monin-Obukov similarity theory (as in Titan CAM). The soil is modeled as 15 layers of variable depth that extends 80 m below the surface. Physical parameters for the soil assume a porous icy regolith composition (Tokano, 2005), but topography and albedo variations are not included. The liquid content of the ground is tracked with a "bucket" model, that adds the amount that is precipitated to the surface and subtracts the amount that is evaporated under Titan's atmospheric conditions as $\frac{\partial q_g}{\partial t} = P - E$, where evaporation E becomes progressively more limited when the grid box's methane content drops below 100 kg/m^2.

Five simulations were run in total for the Lora et al. (2015): a control case that ran at L32 resolution from rest, another control case at L50 with a higher time resolution from the prescribed superrotation rate, a case where each vertical layer's optical depth was varied by the equation:

$$d\tau = dt(1 - (\cos 2\phi - 1)|\sin t|); \tag{4.13}$$

a case where the surface methane was replaced by a global 100-m deep reservoir akin to an inexaustible supply of methane, and a final case of a 4-m deep global reservoir, with 100-m deep reservoirs at the locations of Ontario Lacus, Kraken Mare, Ligeia Mare, and Punga Mare. The first two models were run until a steady state of superrotation was achieved, roughly 70 Titan years for the lower resolution model, and 2 Titan years for the higher resolution model, plus an additional couple of Titan years for analysis purposes. The third model was run to test how haze variation affects the results when compared to the control model. The final two models were run to test how the methane cycle affects the results when compared to the control model.

TAM is able to reproduce the observed temperature profile, zonal winds in the troposphere, and a surface temperature and vertical humidity distribution that is consistent with the surface liquid distribution, and they are able to do so without incorporating the interplay between hazes, trace gases, and large-scale atmospheric dynamics. But they are unable to reproduce the observed stratospheric superrotation, summer mid-latitude clouds, and the previously computationally produced responses to surface turbulent fluxes at the poles. This is in part due to choices made to simplify the model, such as not including topography or cloud microphysics, and assuming the surface methane is inexhaustible.

4.3 TitanWRF

One of the main goals of all of these 3D GCMs is to reproduce the observed superrotating jet observed in Titan's stratosphere (Kostiuk et al., 2001; Bird et al., 2005; Folkner et al., 2006). As we have seen, nearly all of these models fail at this objective, with the exception of the first Titan GCM. It is not enough though to generate windspeeds that are in agreement with observations. All computational modeling efforts strive to include as much realism as possible. Not only do we want to reproduce the superrotation, we want to reproduce it in a model Titan that is as close to the real Titan as possible so that we can trust our understanding of its atmospheric chemistry and dynamics. In this section I will describe the TitanWRF model and my updates and tests to generate superrotation in models with topography.

4.3.1 planetWRF

The TitanWRF model is a planet-specific version of PlanetWRF (Richardson et al., 2007; Newman et al., 2011), which in turn was derived from a GCM for the Earth's climate, the Weather Research and Forecasting (WRF) model (Michalakes et al., 2005; Skamarock et al., 2005). WRF is a 3-D mesoscale model, developed in a collaboration between the National Center for Atmospheric Research (NCAR), the National Oceanographic and Atmospheric Administration (NOAA), the US Department of Defense, and several universities for research and forecasting of the Earth's atmosphere. WRF integrates the fully compressible Euler equations in flux form, with the option of fully solving or approximating the hydrostatic approximation. The code itself is very modular, allowing the user to customize the dynamic core, physics packages, integration scheme, and more. With WRF's modularity, it was easier to build a generalized planet model that was not Earth-specific.

In order to create PlanetWRF, there were two main issues with WRF that needed to be addressed. First, since WRF is a mesoscale model, it could not fully simulate the global domain. Second, it was written exclusively for Earth, with many parameters and processes hard-coded to be Earth-specific. Richardson *et al.*'s changes to the WRF model can be grouped into four categories:

1. Implementation of a Nonconformal Grid
2. Generalization of Planetary Parameters
3. Stabilization of Polar Boundaries and Filtering
4. Parameterization of Sub-Grid-Scale Processes

In order to use the entire globe as a single domain, PlanetWRF uses a cylindrical map projection (a common nonconformal grid used in many GCMs). To calculate

the projection coordinates x and y, the following definitions are used:

$$\begin{aligned} x &= a\lambda \\ y &= a\phi \\ dx &= ad\lambda \\ dy &= ad\phi \\ dX &= a\cos\phi d\lambda \\ dY &= ad\phi \\ m_x &= \sec\phi \\ m_y &= 1 \end{aligned} \tag{4.14}$$

They have also modified the code to be run with a rotated pole, but as I only use the simple cylindrical map projection, I will not list the equations used to convert to the rotated pole here. I run these models with a resolution of 5.625° × 5° in longitude and latitude respectively, with 54σ' vertical layers from the surface to ∼ 500 km. The modified sigma level, σ', is equal to $(P - P_{top})/(P_{surf} - P_{top})$

To generalize the planetary parameters was an easier modification. WRF already had a centralized container for some parameters like surface gravity and gas constants. They simply added additional variables such as orbital parameters and time scales (though they did introduce a solar longitude L_S date system as well) to this central container.

In order to accurately model conditions at the poles in the model, appropriate boundary conditions must be set. The meridional velocity is set to zero, and no flux or gradient calculations can happen across the pole. All grid points with latitudes greater than 60° and that meet the cutoff frequency criterion are Fourier filtered. The cutoff frequency is described by the equation:

$$\kappa_{\max} = (N/2)\cos\phi \tag{4.15}$$

Finally, to parameterize sub-grid-scale processes - i.e. radiative transfer processes - different modules were written for each of the terrestrial bodies initially tested in PlanetWRF V1. In the rest of this chapter, I will describe the Titan-specific modifications in PlanetWRF (TitanWRF), as well as my own improvements, current limits, and future work.

4.3.2 Radiative Transfer

As in many of the GCMs mentioned in Section 4.2, TitanWRF has based its radiative transfer scheme for Titan on McKay et al. (1989), leaving much of the code intact but updating tables (initial atmospheric temperature-pressure profile, molecular profiles, radiation flux, surface details, etc) with new observational data. Equations 4.6 - 4.8 describe how the two-stream radiative flux is calculated. TitanWRF is able to account for the specific spatial, diurnal, and seasonal changes in the solar forcing with the inclusion of the generalized planetary parameters.

4.3.3 Methane Cycle

To include Titan's methane cycle, Newman et al. (2016) needed to parameterize atmospheric evaporation and condensation (and the latent heating and cooling of the atmosphere), precipitation, and surface evaporation and cooling. Condensation will occur in the model when the vapor pressure of methane exceeds the saturation vapor pressure of the atmosphere. There are four temperature regimes that dictate whether or not there will be no condensate (190.53 K $< T$), the condensate is liquid methane (126.2 K $< T <$ 190.53 K $< T$), the condensate is a solution of methane and nitrogen (90.68 K $< T <$ 126.2 K), and the condensate is methane ice ($T <$ 90.68 K).

The surface evaporation is given by the equation:

$$\mathrm{Ev}_{\mathrm{CH_4}} = \min(\mathrm{Surf}_{\mathrm{CH_4}}, \max[C_{\mathrm{drag}}(Q_{\mathrm{sat}} - Q_{\mathrm{CH_4}})M_{\mathrm{fact}}\delta t, 0]) \tag{4.16}$$

where

$$\begin{aligned} Q_{\mathrm{sat}} &= R_{\mathrm{hum}} P_{\mathrm{sat}} M_{\mathrm{rat}}/P \\ \mathrm{Surf}_{\mathrm{CH_4}} &= \mathrm{Surf}^{\mathrm{init}}_{\mathrm{CH_4}} + \sigma_0^t(\mathrm{Pr}_{\mathrm{CH_4}} - \mathrm{Ev}_{\mathrm{CH_4}}) \end{aligned} \tag{4.17}$$

M_{fact} varies with the type of surface liquid methane falls on to. If it falls into porous regolith for example, and is permanently trapped, M_{fact} tends towards 0, whereas if it falls onto a lake where it can easily be evaporated again, M_{fact} tends towards 1. In flat models and in models where surface type is not tracked, M_{fact} is set to 0.5 everywhere.

Finally, to calculate how the temperature of the atmosphere and surface change, the incremental temperature step with time equations are:

$$\begin{aligned} \delta T_{\mathrm{atm}} &= L_{\mathrm{CH_4}} \delta Q_{\mathrm{CH_4}}/c_p \\ \delta T_{\mathrm{surf}} &= -L_{\mathrm{CH_4}} \delta \mathrm{Ev}_{\mathrm{CH_4}}/(c_p^{\mathrm{surf}} \rho_{\mathrm{surf}} \delta z_{\mathrm{surf}}) \end{aligned} \tag{4.18}$$

4.3.4 Planetary Boundary Layer

After running the model with the default topography for 40 years, there is no significant spin-up of the atmosphere, and peak windspeeds are only order 1 m/s, when the goal is to achieve windspeeds of 200 m/s. Two tests were done to both modify the code and explore the parameter space for surface-atmosphere interactions. The first was to change how TitanWRF was handling vertical diffusion in and above the PBL. From Huygens observations, Titan's planetary boundary layer is the lowest 10 m of the atmosphere, though there is a slightly convective neutral PBL that extends to 300 m above the surface (Tokano et al., 2006). The model uses the Medium Range Forecast (MRF) model PBL parameterization in most cases, unless the goal is to model atmospheric turbulence with large eddy simulations. Hong & Pan (1996) developed the MRF PBL based on the nonlocal-K diffusion scheme of Troen & Mahrt (1986). Vertical diffusion had been handled historically by a local-K approach: take the local values of temperature and windspeed, and parameterize the diffusivity coefficients as functions of the local Richardson number (Equation 4.10). Many authors (e.g. Wyn-

gaard & Brost (1984); Stull (1993)) had pointed out the limitations of this scheme in unstable conditions. This is particularly egregious in the PBL, where momentum and mass transfer is accomplished by large eddies that need to be modeled as a bulk phenomenon and not a local one.

Hong and Pan choose to use the nonlocal-K scheme because it can handle large eddy diffusion processes efficiently. I will spend a little time describing the equations that are core to the TitanWRF model's handling of the PBL; reminder that all of the variable definitions can be found in Table 4.2. The turbulence diffusion equations can be described by the equation:

$$\frac{\partial C}{\partial t} = \frac{\partial}{\partial z}\left[K_c\left(\frac{\partial C}{\partial z} - \gamma_c\right)\right] \tag{4.19}$$

K_c is the local diffusion coefficient as defined in local-K theory in the free atmosphere. There are countergradient correction terms γ_c applied within the mixed boundary layer on θ and q to incorporate the effects of large-scale eddies to the total flux:

$$\gamma_c = b\frac{\overline{(w'c')}}{w_s} \tag{4.20}$$

The momentum diffusivity coefficient is described by the equation:

$$K_{zm} = kw_s\left(1 - \frac{z}{h}\right)^p \tag{4.21}$$

The von Kármán constant k (called "xkzo" in TitanWRF for historical reasons) is a dimensionless constant that describes the distribution of the longitudinal velocity in turbulent flows. This can vary depending on the planet/moon atmosphere, but was actually set to zero in the default TitanWRF model.

with the mixed velocity scale height w_s equalling:

$$w_s = u_*\phi_m^{-1} \tag{4.22}$$

The functions ϕ_m and ϕ_t vary depending on if conditions are stable or unstable. For unstable and neutral conditions $(\overline{w'c'}) \leq 0$:

$$\begin{aligned} \phi_m &= \left(1 - 16\frac{0.1h}{L}\right)^{-1/4}, \text{ for } u \text{ and } v \\ \phi_t &= \left(1 - 16\frac{0.1h}{L}\right)^{-1/2}, \text{ for } \phi \text{ and } q \end{aligned} \tag{4.23}$$

and for the stable regime $(\overline{w'c'}) > 0$:

$$\phi_m = \phi_t = \left(1 + 5\frac{0.1h}{L}\right) \tag{4.24}$$

The boundary layer height is calculated by the equation:

$$h = \mathrm{Rib}_{\mathrm{cr}} \frac{\theta_{va}|U(h)|^2}{g(\theta_v(h) - \theta_s)} \tag{4.25}$$

where

$$\theta_s = \theta_{va} + \theta_r \big[= b \frac{\overline{(w'\theta'_v)_0}}{w_s h} \big] \tag{4.26}$$

The boundary layer height is calculated iteratively by first estimating Equation 4.25 without the effects of thermal excess. This initial h is used to calculate ϕ_m and ϕ_t to get the mixed layer velocity w_s. Finally, the actual h is calculated, allowing us to calculate K_{zm}.

The eddy diffusivity for temperature and moisture is calculated from the Equation 4.21 and the Prandtl number, a dimensionless number that is the ratio of momentum diffusivity to thermal diffusivity. In the model, this is described by the equation:

$$\mathrm{Pr} = \big(\frac{\phi_t}{\phi_m} + bk\frac{0.1h}{h}\big) \tag{4.27}$$

Exiting the PBL and entering the free atmosphere, the diffusivity coefficients are described by the equation:

$$K_{m,t} = l^2 f_{m,t}(\mathrm{Rig}) \Big| \frac{\partial U}{\partial z} \Big| \tag{4.28}$$

where $f_{m,t}(\mathrm{Rig})$ are stability functions of the local gradient Richardson number:

$$\mathrm{Rig} = \frac{g}{T} \frac{\partial \theta_v}{\partial z} \frac{\partial U}{\partial z}^{-2} \tag{4.29}$$

and the mixing length l is calculated as:

$$\frac{1}{l} = \frac{1}{kz} + \frac{1}{\lambda_0} \tag{4.30}$$

4.3.5 Topography

The default map at this time is the Synthetic Aperture RADAR (SAR) map from Lorenz et al. (2013) (see Figure 4.2). Cassini RADAR took images of Titan's surface, and Lorenz *et al.* developed the SARTopo routine to analyze the results and produce the map used in this model. Initially, SAR only covered $\sim$ 35% of Titan's surface. SAR-topo is the scheme to estimate an along-track topographic profile. It is able to use the overlap in the beam footprints to interpolate terrain heights in the gaps. Additional radar altimetry was obtained eventually to bolster the dataset and improve the SARTopo map and covering more of Titan. The Cassini data are binned in $1^\circ \times 1^\circ$ in latitude-longitude respectively, and there are a couple of gaps corresponding to roughly 2000 km of area due to the spacecraft's orbit.

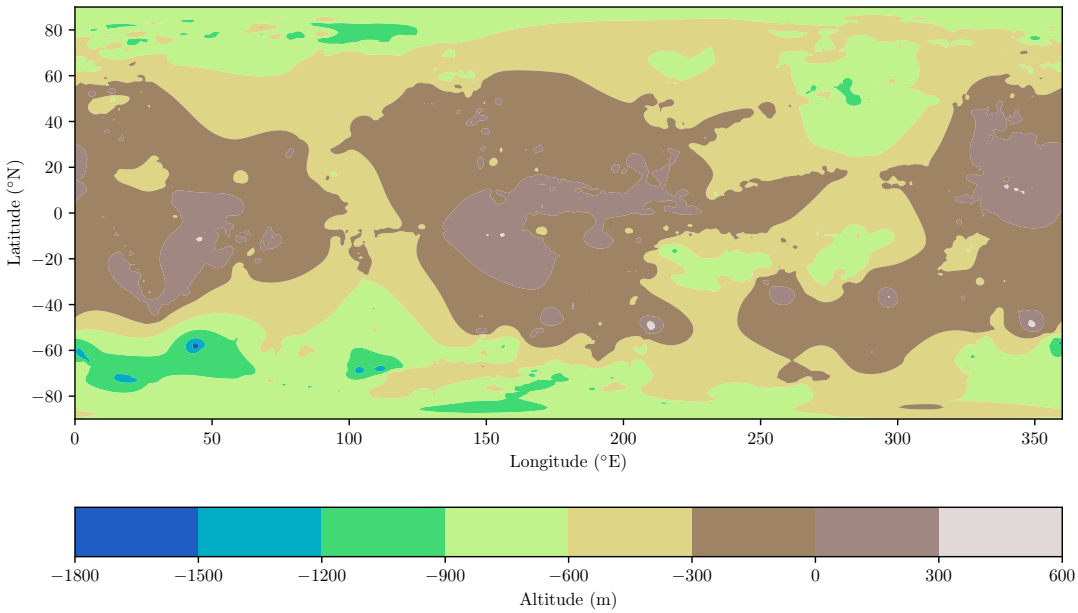

Figure 4.2: SARTopo map from Lorenz Lorenz et al. (2013) as used as input in TitanWRF.

Although the xkzo tests showed some improvement over the default topography model, we were still only getting windspeeds of order 10 m/s. The diffusion above the PBL was not the only issue. We thus hypothesized that gravity waves generated by the surface topography, particularly in regions with "sharp" topographical features, were growing too large and deterring the growth of the jet. After completing the xkzo study, I then ran a model set using the best of the xkzo models (xkzo = 0.025) and Gaussian-smoothed versions of the Lorenz map and Corlies Corlies et al. (2017) that is also included in the current version of TitanWRF. In Figure 4.3 one can see the two topographical maps as TitanWRF sees them at its current resolution. In the smoothed versions, many of the smaller features and sharper corners have been smoothed out by the Gaussian image smoothing routine in `python`.

4.3.6 Results

Our first diagnostic of how my changes affected model spin-up is to calculate how the superrotation index changes over time. This index is the total angular momentum of an atmospheric layer divided by the total angular momentum of that layer at rest, and the observed windspeeds correspond to an index of 16 and greater. The flat TitanWRF model does achieve this index, but the best I was able to produce in models with topography has an index of 11 after running the model with xkzo = 0.025 and smoothed topography for 70 Titan years. Figure 4.4 shows a comparison of the evolution of superrotation indices for all of the models tested.

This is not to say though that the model is not significantly improved over the previous version. This superrotation index corresponds to peak windspeeds of 125

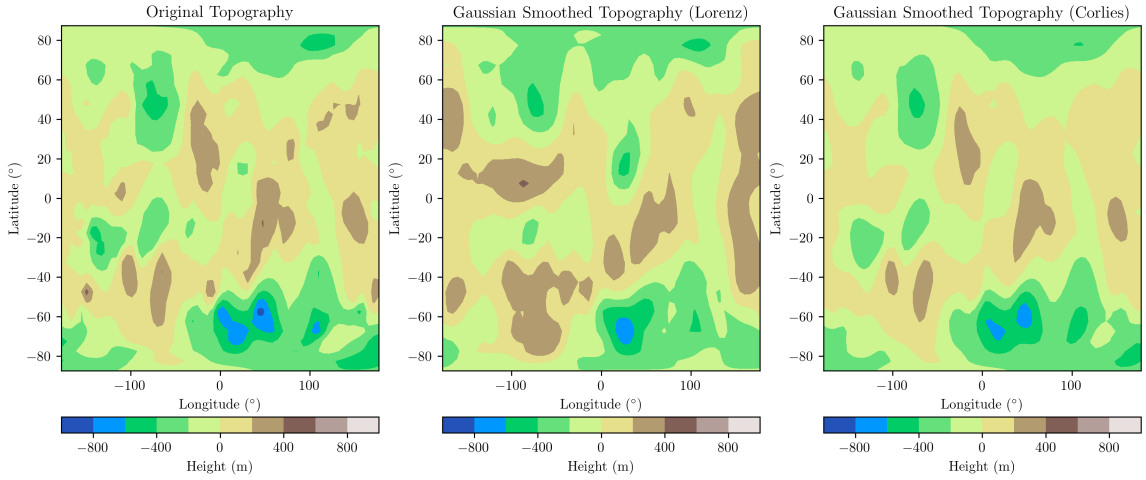

Figure 4.3: The default topographical map from Lorenz et al. (2013) (left) and the Gaussian-smoothed versions of the Lorenz map and Corlies map (Corlies et al., 2017)tested in this study (middle and right) as interpreted by TitanWRF. The original map data is read in, shifted to the same latitude-longitude scale, and reduced in resolution.

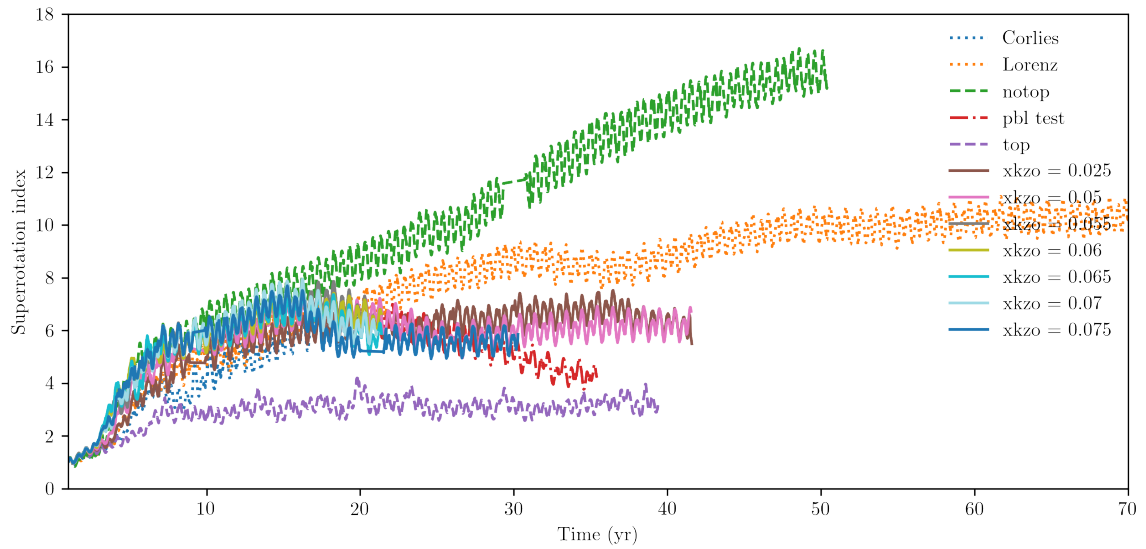

Figure 4.4: Comparison of the superrotation indices of several different models tested in this study. Corlies and Lorenz refer to two smooth-topography tests using the Corlies et al. (2017) and the Lorenz et al. (2013); Corlies et al. (2017) maps. "notop" refers to the default version of TitanWRF which has no topography. "pbl test" is the brief test to modifiy the vertical diffusion scheme above the PBL. "top" is the version of the model with the default Lorenz map (no smoothing). And the various "xkzo" lines refer to tests using each of those as the von Kármán constant.

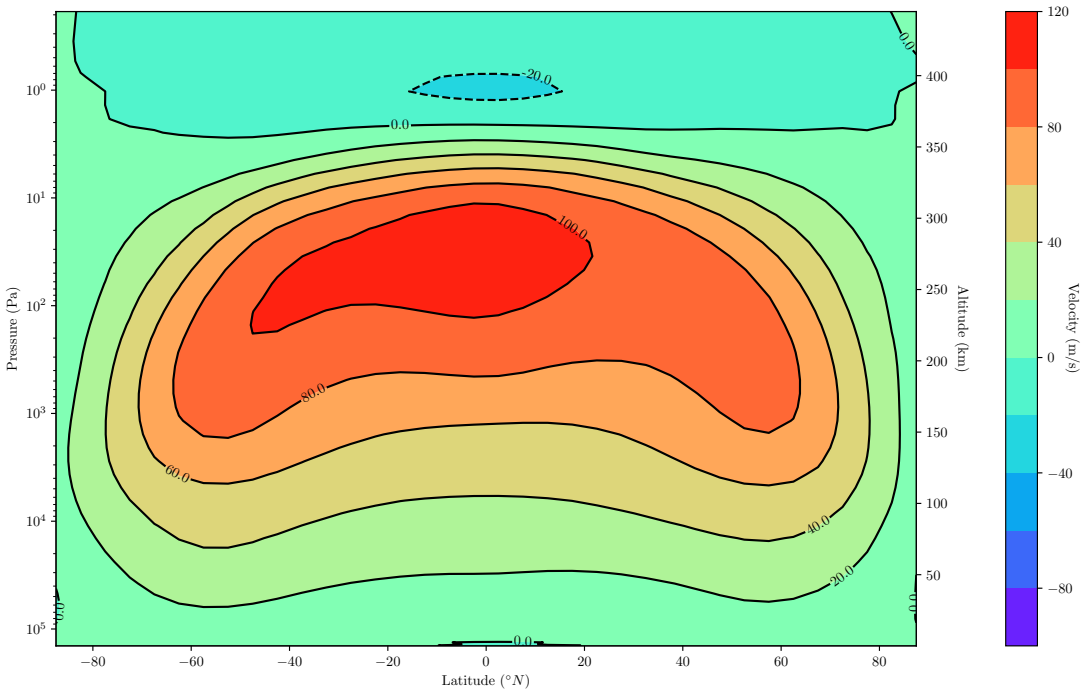

Figure 4.5: Zonal wind plot at the end of the spin-up period, in year 70 of the model. Peak windspeeds occur between 200 and 300 km in the stratosphere. Observations of the superrotating jet measure it at an altitude of $\sim$ 345 km (Cordiner et al., 2020b; Flowers et al., in prep. 2023a).

m/s in the stratosphere, though at slightly lower altitudes than observed. Figure 4.5 shows the zonal winds for the final year of the simulation.

We also compared temperature-altitude and zonal wind profiles to Huygens HASI and DWE data (see Figure 4.6) so see if any of my tests were an improvement over the original TitanWRF model setup. The temperature-altitude profile in all cases does not properly reproduce the troposphere, underestimating or overestimating the temperature and shifting the height of the troposphere down. All models with topography follow a similar temperature profile, though the default topography model has more erratic temperature swings than all of the others, supporting the hypothesis that the lack of diffusion in that model was the source of some error. All of the models with topography though overestimate the temperature of the stratosphere. The zonal winds do not match the observations at all, even though they are calculated at the same longitude and latitude as the Huygens landing site (192.3° west, 10.3° south). Models with topography produce values closer to the measurements than the model without topography, so it is possible that since these are average values (as opposed to the instantaneous value measured by the DWE) that we will not be able to calculate a zonal wind profile that more closely matches the observations.

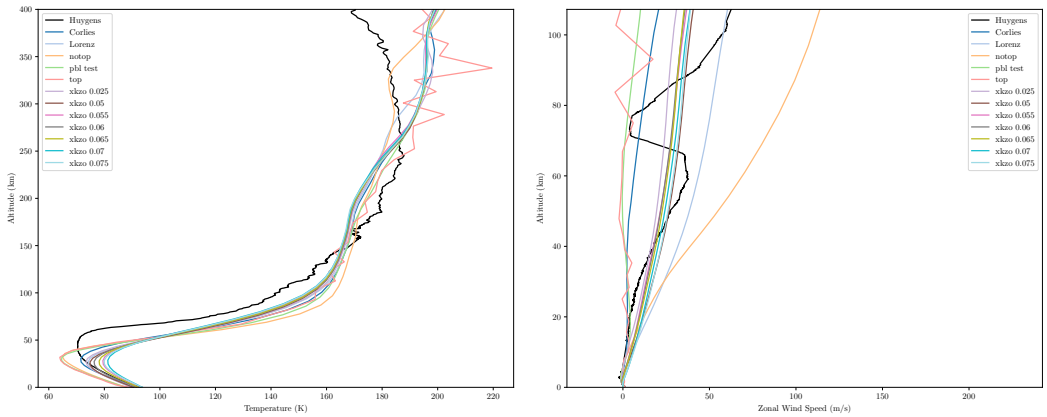

Figure 4.6: (Left) Comparison of the temperature-pressure profiles calculated in TitanWRF vs. the Huygens lander HASI measurements (Fulchignoni et al., 2005) in black. (Right) Comparison of the average zonal winds at the Huygens landing site versus the Huygens lander DWE measurements (Folkner et al., 2006).

4.4 Conclusion

There are a handful of Titan 3-D GCMs in use today, several of which were derived from GCMs of the Earth's atmosphere. Terrestrial worlds are extremely difficult to model. The interplay between atmospheric, surface, and subsurface processes is difficult to capture in its entirety without there either being immense computational costs or oversimplifications. Earth GCMs have the advantage of being able to almost immediately verify and hard code the physical properties observed. For Titan, where we still lack crucial information about surface composition, the true extent of its liquid methane reservoirs, haze dynamics, and more, we are at a disadvantage until the Dragonfly Mission begins operations. For the time being, we are able to compare Titan GCM output to Cassini-Huygens measurements and gradually improve our models. In this chapter, I summarized the current state of Titan GCMs and analyzed the GCM I have worked with, TitanWRF. I discuss the modifications I have made to this model, and present results of the first TitanGCM to produce order 100 m/s winds in the stratosphere with topography included in the model. I compare these results to observations from Cassini-Huygens, and finally discuss additional hypotheses for further improvement. The summary of all GCMs discussed in this chapter can be found in Table 4.1.

Model	Reference	Summary	Strengths	Weaknesses
LMD	Hourdin et al. (1995)	The first Titan 3D GCM	Successfully reproduces superrotation observed at the time	Underestimates winds observed by Cassini; no topography
Cologne GCM	Tokano et al. (1999)	First model to include hazes	Reproduces observed haze asymmetry	Does not reproduce stratospheric superrotation; no topography
TitanWRF	Richardson et al. (2007)	Based on Earth WRF model	Modular, reproduces superrotation (now with topography, though not quite as fast as observed)	Does not quite reproduce observed superrotation with topography, fails to reproduce TP Profile and ZW profile
Titan CAM	Friedson et al. (2009)	Based on NCAR model	Reproduced seasonal Hadley circulation and is consistent with other models	Fails to reproduce superrotation
IPSL-LMDZ	Lebonnois et al. (2012)	Successor to LMD	Is able to reproduce results of original	Results not drastically different from original
TAM	Lora et al. (2015)	Newest GCM	Reproduces observed TP profile and some surface conditions	Does not reproduce stratospheric superrotation, simplified model

Table 4.1: Summary of current 3-D Titan GCMs in chronological order of first appearance.

Appendix

4.A Definitions of Symbols

Variable	Description	Equation
ρ	Density	4.1
t	Time	4.1
$\mathbf{U}$	Velocity field (u, v, w dimensions)	4.1
Ω	Reference frame rotation velocity	4.2
P	Pressure	4.2
$\mathbf{g}_{eff}$	Effective gravity term	4.2
$\mathbf{F}_f$	Frictional forces	4.2
T	Temperature	4.4
z	Altitude	4.4
μ	cos of angle of incident radiation	4.6
I_ν	Intensity of radiation with frequency ν	4.6
τ_ν	Optical depth of radiation with frequency ν	4.6
S_ν	Source function	4.6
$\omega_{0\nu}$	Scattering albedo	4.6
P_ν	Scattering phase function	4.6
F_ν	Flux	4.7
$\lambda_n u$	Wavelength	4.8
Γ	Coefficient based on form of equation	4.8
C_n	Functions of optical depth	4.8
K_z	Turbulence coefficient	4.9
l	Mixing length	4.9
e	Turbulent KE diagnosic	4.9
π	Dynamic surface pressure	4.11
$\mathrm{Ev}_{\mathrm{CH_4}}$	Evaporation rate	4.16
$\mathrm{Surf}_{\mathrm{CH_4}}$	Surface distribution of methane	4.16
C_{drag}	Surface exchange coefficient	4.16
Q_{sat}	Saturation mass mixing ratio (mmr)	4.16
$Q_{\mathrm{CH_4}}$	mmr Methane vapor	4.16
R_{hum}	Relative humidity	4.17
P_{sat}	Saturation pressure	4.18
$\mathrm{Pr}_{\mathrm{CH_4}}$	Precipitation rate	4.17
T_{atm}	Atmospheric temperature	4.18
T_{surf}	Surface temperature	4.18
ρ_{surf}	Surface density	4.18
C	Turbulent prognostic variable	4.19
K_c	Eddy diffusivity coefficient	4.19
γ_c	Correction to local gradient	4.20
b	Proportionality coefficient	4.20

ω_s	Mixed-layer velocity scale	4.22
u_*	Surface frictional velocity scale	4.22
ϕ_m	Surface wind profile function at top	4.22
ϕ_t	Surface countergradient profile function	4.23
$K_z m$	Momentum diffusivity coefficient	4.21
h	Boundary layer height	4.21
θ_{va}	Virtual potential temperature at lowest model level	4.25
θ_v	Virtual potential temperature	4.25
θ_s	Temperature near surface	4.25
θ_r		4.26
U	Horizontal wind speed	4.28
$K_{m,t}$	Free atmosphere diffusivity coefficients	4.28
$f_{m,t}$	Stability functions	4.28
λ_0	Asymptotic length scale	4.30

Table 4.2: Descriptions of symbols with location of first appearance

4.B Numerical Constants

Symbol	Description	Value	Equation
M_{fact}	Surface moisture availability factor	0.5	4.16
M_{rat}	Radio of mean molecular masses	16/27	4.17
c_p	Specific heat capacity	1044 J/K/kg	4.18
δz_{surf}	Surface altitude step	0.012	4.18
p	Profile shape exponent	2	4.21
k	von Kárman constant	varies	4.21
g	Surface gravity	1.35 m/s^2	4.29

Table 4.3: Values for constants

Chapter 5

Superrotating Jet

5.1 Introduction

A major dynamic feature of Titan's atmosphere is the presence of strong superrotating winds in the upper and lower atmosphere. First detected with the Voyager I IR instrument (IRIS) (Flasar et al., 1981), an equatorial, high altitude superrotating jet, as well as superrotating zonal winds in troposphere have since been measured by Cassini-Huygens (Bird et al., 2005; Achterberg et al., 2008, 2011; Folkner et al., 2006), and several ground-based telescopes (e.g. Hubbard et al. (1993); Kostiuk et al. (2001); Moreno et al. (2005)). More recently, Titan has been imaged by the Atacama Large Millimeter Array (ALMA) (Lellouch et al., 2019; Cordiner et al., 2019, 2020b), and comparisons between the different observations at different epochs suggest temporal variability the high altitude zonal wind Cordiner et al. (2020a). For slow rotating bodies like Titan, a single large Hadley cell tends to dominate the atmosphere from pole to pole, and one would expect a jet to form in higher latitudes (Tokano et al., 1999). Its location at the equator suggests that there is a mechanism through which eddies must be transporting angular momentum from the surface up towards the stratosphere and/or from the poles and mid-latitudes towards the equator (Gierasch, 1975; Rossow & Williams, 1979).

Over the years, different general circulation models (GCMs) have tried to reproduce this superrotating jet. The first 3D Titan GCM, created at Laboratoire de Météorologie Dynamique (LMD) (Hourdin et al., 1995) did generate a superrotating zonal wind that reasonably reproduced the measurements that were available at the time. Since then, no one has been able to produce 3D GCM results that agree with measurements of the jet, particularly in models that include surface topography. In this chapter I present results from Flowers et al. (in prep. 2023a) of the TitanWRF V3 3D GCM (Richardson et al., 2007; Newman et al., 2011; Flowers et al., in prep. 2023b) that incorporate Titan's observed topography, and compare them to ALMA observations. I specifically will focus on the observations results for the winds in Titan's upper stratosphere ($z \sim 350 - 400$ km), where the superrotating jet is detected. Section 5.2 describes the data taken with ALMA in 2016 and 2017 used in this study (Cordiner et al., 2020b), section 5.3 briefly describes the TitanWRF model setup (for

more details on TitanWRF in this dissertation, see Chapter 4), in section 5.4 I present the resulting TitanWRF output and discuss how it compares to the ALMA data in section 5.5, before concluding in section 5.6.

5.2 Observations

The data used in this study are from ALMA program 2016.A.00014.S (PI: M. Cordiner) as described in Cordiner et al. (2019, 2020b), taken on May 8th and May 16th, 2017, to be complementary with Cassini CIRS observations of Titan's solstice on May 24th, 2017. Titan was observed in several Band 7 frequency windows in the 349 - 364 GHz range to encompass the molecular transitions of interest. In this study, we use the observations of acetonitrile (CH_3CN). The CH_3CN ($J = 19 - -18$) transition was observed at a resolution of $\Delta\nu = 488$ kHz. 46 antenna were configured such that the spatial resolution was $\approx 0.''24 \times 0.''19$. The total observing time was 138 min, resulting in an RMS noise of ≈ 2 mJy beam^{-1} MHz^{-1} (Cordiner et al., 2020b). Quasar J1733-1304 was used for the flux calibration, observed on May 4th and May 17th and with an accuracy of $\pm 6\%$ (Cordiner et al., 2019).

After continuum subtracting the raw observations, the data were imaged and deconvolved with a mask diameter of $1.''3$ using the `tclean` package from CASA 5.6 (Emonts et al., 2019). This corrects for the time-variability of Titan's orbital position and radial velocity. The pixel size was set to $0''.025$ and the flux threshold was twice the RMS noise per channel. The CH_3CN data was convolved to a circular beam dimension $\theta_{km} = 1670$ km to account for Titan's varying geocentric distance ($\Delta = 9.21$ AU in 2017).

Finally, to produce Doppler maps from this data, Cordiner et al. (2020b) used the method from Lellouch et al. (2019) to calculate line of sight (LOS) velocities for CH_3CN (and the other gases in their study) as a function of spatial coordinates. To do so, they fit Gaussian profiles to the emission lines of individual spectra to determine their Doppler shifts. Because CH_3CN also has pressure-broadened Lorentzian wings, the fits were restricted to 3 MHz-wide spectral regions centered on the line cores. To remove the pseudo-continuum created by the wings, an intensity offset was included. To improve the sensitivity of the CH_3CN calculation, the results for the three highest-frequency lines were averaged together. The uncertainty for the measurements was derived by refitting the Gaussian line model to a set of synthetic noise datasets with a Monte Carlo approach similar to the one in Lellouch et al. (2019).

5.3 TitanWRF

The TitanWRF GCM is a Titan-specific version of the PlanetWRF atmospheric model (Richardson et al., 2007). PlanetWRF itself was developed from the Weather Research and Forecasting (WRF) model created by the National Center for Atmospheric Research to study the Earth's atmosphere. PlanetWRF is the generalized version that has been modified to allow the user to specify planet-specific parameters

to calculate global and local climate systems. So far it has been adapted to study the atmospheres of Mars, Venus, and Titan. Unlike the original WRF model, PlanetWRF includes a nonconformal grid modification in order to use the full globe as a domain, polar boundaries and filtering to handle poleward and over-the-pole material advection and prevent instabilities at high latitudes, generalized parameterization and timing schemes to easily change planetary parameters like surface gravity and orbital distance, and parameterization of sub-grid-scale physical processes such as radiative transfer schemes and haze physics. For a full description of the PlanetWRF model and how it was modified for Titan, see Richardson et al. (2007).

For TitanWRF, the once-hard-coded parameters for Earth have been generalized in the code, allowing us to easily define its orbital parameters and general physical properties such as its size, orbital architecture, and boundary layer mixing schemes. The radiative transfer is calculated following the same two-stream approach as described McKay et al. (1989), with gas and haze properties calculated from a slight modification of a scheme described in the same study. The model also incorporates Saturn's gravitational impact, a solver for surface and subsurface heat diffusion, and a non-local boundary layer diffusion solver.

Our model is configured as a 3D global, latitude-longitude, hydrostatic model. There are 54 σ' vertical layers, where $\sigma' = (P - P_{top})/(P_{surf} - P_{top})$ and P is pressure. The horizontal resolution is 5° in latitude and 5.625° in longitude. The GCM was run on the NASA Pleiades cluster for $\sim$ 35 (nonconsecutive) actual days on 3 nodes, 24 processors per node, to simulate 70 Titan years, with a timestep of 10 Titan days. For the remainder of this paper, all time scales (year, day, hour, etc) will refer to a Titan time scale (1 Titan year = 29 Earth years), but all units will be in SI. As referenced in the Introduction, several Titan GCMs, including TitanWRF, were able to reproduce the observed stratospheric superrotation under certain conditions, none of which included topography. In this paper, we present TitanWRF results that include topography in the model set up, using topographical maps produced from Cassini RADAR data using the SARTopo data described in Stiles et al. (2009); Lorenz et al. (2013) and Corlies et al. (2017). A separate publication is in preparation describing our improvements to the TitanWRF model to generate appreciable superrotation in non-flat models (Flowers et al., in prep. 2023b). Then to create line of sight Doppler wind maps from the model output for comparison with ALMA data, we use the equation:

$$v_{LOS} = -(u \sin\theta + v \cos\theta \sin\phi) \tag{5.1}$$

where u is the east-west and v is the north-south wind components, ϕ and θ are latitude and longitude respectively, R_p being the planet's radius at the surface, z is the altitude, and Ω the planet's bulk rotation rate.

5.4 Results

I find that with my improvements to TitanWRF we come closer than ever before to reproducing the observed superrotation in models that include Titan's topography. Figure 5.1 shows the Doppler wind maps as measured via CH_3CN observations for

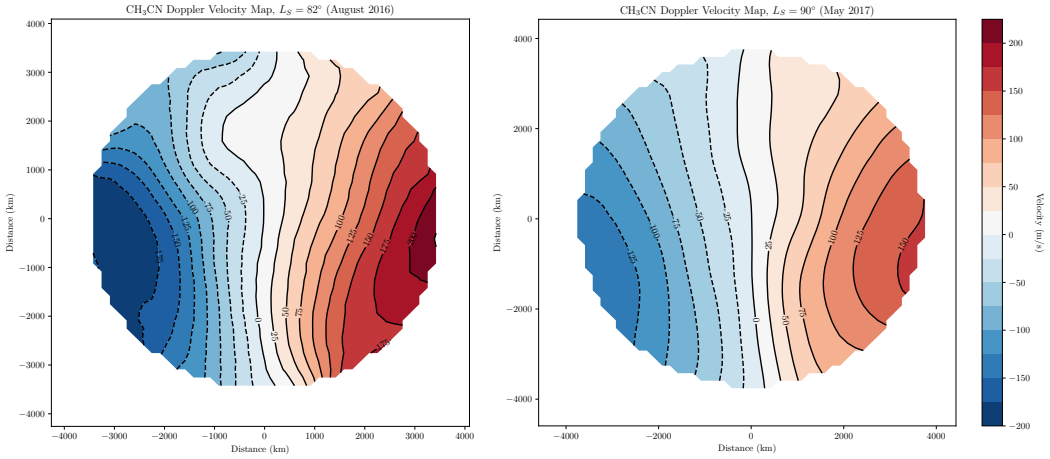

Figure 5.1: CH_3CN Doppler maps from Cordiner et al. (2020b) from August 2016 (left) and May 2017 (right).

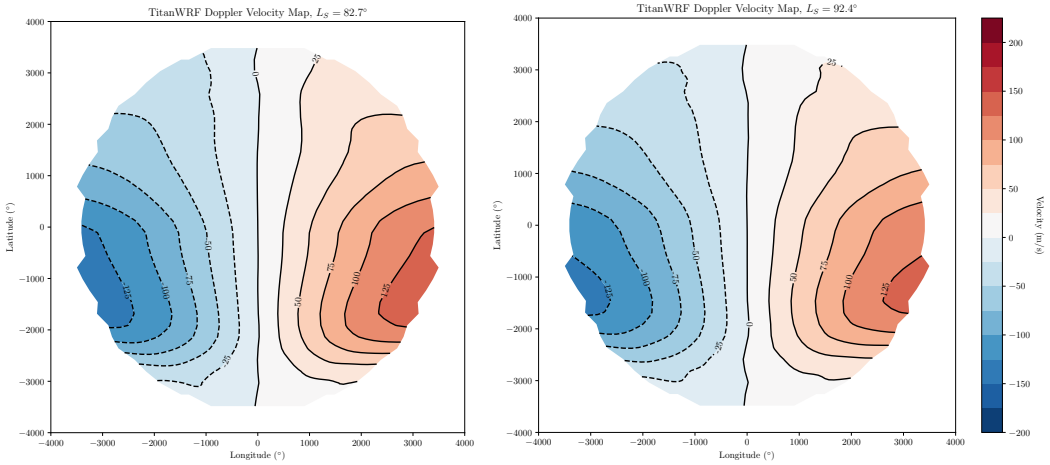

Figure 5.2: Doppler maps from TitanWRF output in year 69 at $L_S = 82.7°$ and $L_S = 92.4°$, which correspond closest to the time of the ALMA observations in Figure 5.1

$L_S = 82°$ and $L_S = 90°$, while Figure 5.2 shows Doppler wind maps as produced by TitanWRF at the closest corresponding times in the model. The ALMA maps probe winds at roughly 345 km in altitude, but peak Doppler windspeeds in the TitanWRF output is from slightly lower at ~ 300 km. The TitanWRF Doppler maps come from the end of this model's spin-up period, shortly after an angular momentum transfer event. Wind speeds peak at 150 m/s in the model, compared to 225 m/s in the observations. It should be noted though that at $L_S = 90°$, peak wind speeds are only 175 m/s.

5.5 Discussion

For the first time we present results of the TitanWRF GCM including topography that represent a significant improvement over previous attempts to reproduce observed superrotation in the upper stratosphere. Many previous models that did not include topography produced weak stratospheric winds (e.g. Friedson et al. (2009); Lora et al. (2015)), and the LMD model (Hourdin et al., 1995; Lebonnois et al., 2012) so far is the only one to reproduce observations (also in the flat case). Although this model is an improvement, we still do not quite reach the observed windspeeds, and the peak winds are observed lower down as opposed to in the same region of the atmosphere probed by the CH_3CN line. This can be for several reasons. The first is that the region of the atmosphere we are trying to replicate is near the model top. Due to the boundary conditions at the top of the model, there is less adiabatic heating in the winter hemisphere. This negatively affects the temperature gradient, and winds that circulate from the poles to the equator where they dump angular momentum and contribute to the equatorial jet's growth. Another issue could be due to the gravity waves caused by the surface topography interfering with barotropic waves that grow the jet. A final potential issue that we will note is that the resolution might be too lower to capture sub-grid scale physics that could affect the transport of angular momentum. A longer discussion of these issues is in Section 4.3.

The ALMA data shows seasonal variability of the jet, with peak (deconvolved) windspeeds dropping by as much as 27 m/s in the CH_3CN observations, but we do not reproduce this level of variability in the TitanWRF model. Though there are variations in the jet's shape, the windspeed is consistent over the same time period in the model.

Jet growth occurs as barotropic (Rossby) waves deposit energy into the equatorial jet. Around solstices, there is a large upwelling of angular momentum from the poles towards the equator, and the reverse happens at equinoxes. Gravity waves generated by surface topography can interfere with this process though, stunting the growth of barotropic waves, which could partially explain why our peak windspeeds are lower than observation. Another known issue is the dependence on the horizontal resolution. Newman et al. (2011) found that when they halved their standard resolution, while the model spun up much quicker, the final superrotation index (the ratio of the atmospheric layer's angular momentum to the total atmosphere's angular momentum at rest) was lower than the value necessary to achieve observed windspeeds (in a model with no topography). We intend on exploring the effects of increasing the resolution of the model in the future, but note that it is very computationally expensive.

5.6 Conclusion

We present Doppler wind velocity maps generated with the TitanWRF GCM in models that include topography, and compare the results to ALMA Doppler wind velocity maps for Titan's stratosphere at an altitude of $\sim$ 345 km. We find significant improvement over previous models that include topography in generating superrotation,

retrieving maximum windspeeds of 150 m/s at an altitude of 300 km. In the default state of TitanWRF, and many other GCMs that include topography, maximum wind speeds in the stratosphere only reach a few-to-tens of meters per second. With observed winds at this altitude being between 175 - 225 m/s, our results are significantly closer, though we recognize some caveats.

The peak windspeeds occur ≈ 45 km lower than where the observations were taken of the jet. This is likely do to the fact that the model top is at ~ 400 km, and winds near the model top are unable to grow efficiently due to a lower adiabatic heating rate in the winter hemisphere. The slower windspeeds are also generally caused by gravity waves generated at the surface by the topography. These waves grow and interfere with the growth of barotropic waves (those responsible for speeding up the stratospheric jet). We have taken steps to mitigate their effects, described in Flowers et al. (in prep. 2023b), but we have not completely fixed the issue. To do so will be the work of a future study.

Appendix

5.A Definitions of Symbols

Variable	Description	Equation
v_{LOS}	Line of sight velocity	5.1
u	East-west velocity	5.1
v	North-south velocity	5.1
θ	Longitude (°E)	5.1
ϕ	Latitude (°N)	5.1
z	Altitude	5.1

Table 5.1: Descriptions of symbols with location of first appearance

5.B Numerical Constants

Variable	Description	Value	Equation
R_p	Titan's radius	2,574.7 km	5.1

Table 5.2: Values for constants

Chapter 6

Surface-Atmosphere Interactions

6.1 Introduction

Titan's surface is in many ways incredibly similar to the Earth's: it has rivers, lakes, and seas and a vast equatorial desert with sand dunes that can reach over 100 meters in height. Instead of being shaped by water though, Titan's surface is shaped by liquid methane.

Until the Cassini-Huygens mission, we knew very little about Titan's surface. The main haze layer was too thick for ground-based telescopes or flyby probes to penetrate. There were several calculations of Titan's temperature-pressure profile, with predictions for what the surface temperature should be (McKay et al., 1989, 1991), and eventually there was a measurement taken by but it was not until the Cassini orbiter took images of the surface that we understood that Titan not only had a diverse topography, but also liquid methane (Tomasko et al., 2005; Stofan et al., 2007; Cassini Collaboration, 2019). Titan's north and south poles have large liquid methane reservoirs, the largest being Kraken Mare in the north pole (Stephan et al., 2010). Titan's methane cycle - analogous to the water cycle on Earth - carves channels and canyons, and over time the shorelines of the large lakes and seas have grown and receded (Barnes et al., 2009; Hayes et al., 2011).

Titan's liquid methane content still has not been precisely quantified. Theoretically, much of Titan's methane should be evaporating away, the surface becoming drier. In some cases, Titan's methane lakes are shrinking in size. In Figure 6.1, one can see how the shoreline of Ontario Lacus in Titan's south pole has receded (Aharonson et al., 2009; Hayes et al., 2011). But the lakes and seas seem to have relatively stable methane content, so the question remains: how is Titan's liquid methane being replenished? There is some evidence of an underground ocean of liquid methane, ethane, and water, but a new mission is required to confirm its presence.

Titan's mid-latitudes and equatorial region is significantly drier than its poles. There are a variety of topographical features (see Figure 6.2) imaged with Cassini and Huygens instruments that are the result of aeolian and fluvial processes analogous to those that take place on Earth, or impacts. Dunes were perhaps the most surprising feature (after liquid methane). Prior to the Cassini mission, it was predicted that

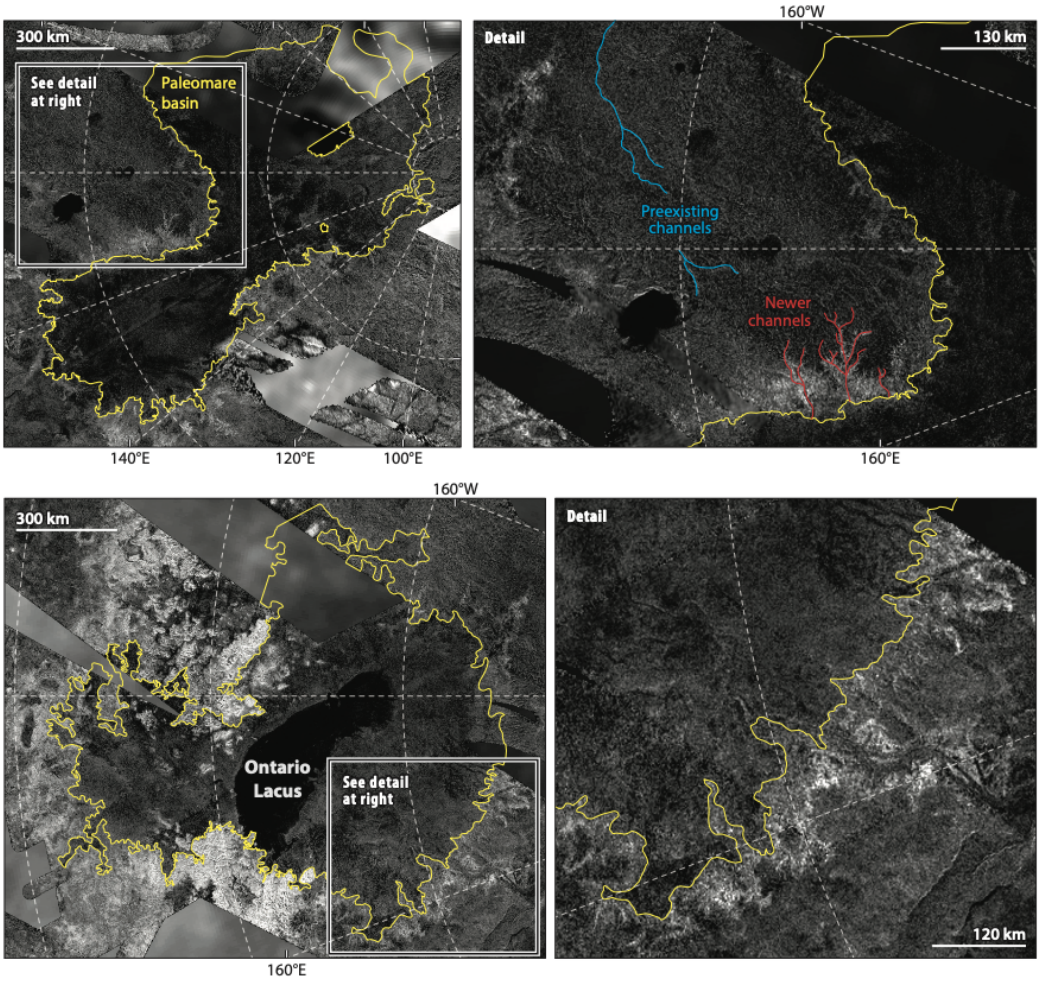

Figure 6.1: Synthetic Aperure Radar (SAR) mosaics from Cassini RADAR of Ontario Lacus in Titan's south pole. Yellow lines show the previous extent of Ontario Lacus, and blue and red lines show preexisting and newly forming channels respectively. SAR is a form of active data collection, where the instrument produces radiation itself, and then records the reflected radiation off the planet (or moon).

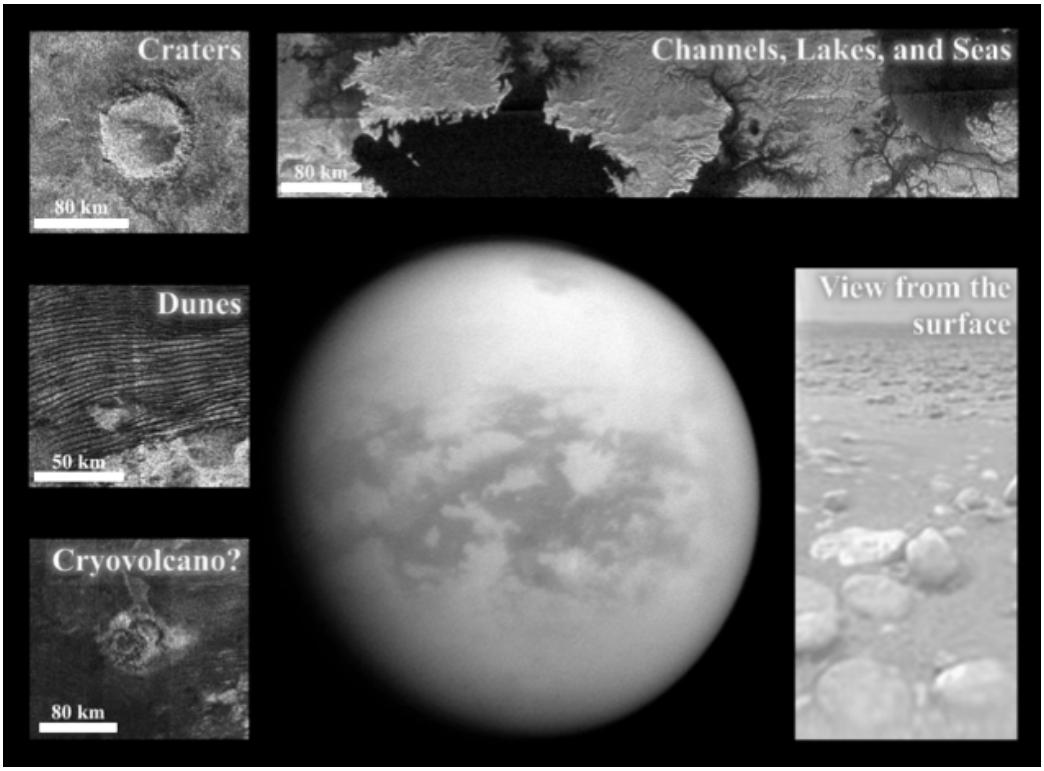

Figure 6.2: Figure 9 from Hörst (2017), which compiles examples of several surface features of Titan imaged with Cassini RADAR and Huygens DISR.

Titan's atmosphere was not conducive for dune formation (Lorenz et al., 1995), yet dunes cover 10 - 20% of Titan's surface (Elachi et al., 2005; Lorenz et al., 2006b; Radebaugh et al., 2008; Lorenz & Radebaugh, 2009; Le Gall et al., 2011; Rodriguez et al., 2014). The NASA Dragonfly will be landing in Titan's equatorial region, somewhere in the Shangri-La field, and exploring the dunes as it makes its way to Selk Crater. As such, understanding the mechanisms behind which they are formed and evolve over time is important from an engineering perspective. This chapter contains discussion and results from Flowers et al. (in prep. 2023c). Section 6.2 contains an overview of our understanding of dunes from Cassini-Huygens, while section 6.3 focuses on the study itself, before concluding in section 6.4.

6.2 Dunes

6.2.1 Observations

Cassini RADAR (Elachi et al., 2004) and VIMS (Brown et al., 2004) mapped and characterized Titan's surface, but with only $\sim$ 10% of sunlight reaching the surface (McKay et al., 1991; Tomasko et al., 2005), this was a difficult task from orbit. RADAR had four modes (altimeter, scatterometer, Synthetic Aperture RADAR (SAR), and radiometer), and generally observed in the K-band at a frequency of 13.87

GHz, corresponding to a spatial resolution of several tens of kilometers. The SAR could observe at higher resolutions in a couple of modes. VIMS operated in wavelengths from 0.35 - 5.2μm, and could at achieve a few kilometers of resolution (at best a few hundred meters of resolution). The Huygens DISR instrument was also able to take visible light images during its descent (Tomasko et al., 2002). In order to make basic determinations of Titan's surface composition, RADAR and VIMS data were correlated, with some input from the DISR data (Soderblom et al., 2007; Rodriguez et al., 2014).

The RADAR instrument has the best spatial sampling of the orbital suite. SAR has spatial resolutions of 0.2 - 2 km/pixel when the spacecraft is at its closest approach (up to 4000 km in altitude), and "HiSAR" has spatial resolutions of 1 - 20 km/pixel when the spacecraft is at altitudes of 10000 km and greater. Between 2004 and 2013, the RADAR instrument took nearly 150 images and covered 58% of Titan's surface. The mosaic of these images can be seen in Figure 6.3. SAR's spatial resolution is good enough to identify individual dunes (seen in Figure 6.2 and in Figure 6.4). Rodriguez *et al.* manually outline the dune regions in the bottom image of Figure 6.3, and determine that dunes cover 13 $\pm$ 2% of Titan's surface (revised from the 20% determination of Radebaugh et al. (2008)).

The VIMS instrument takes images in 352 separate wavelengths that are produced as hyperspectral cubes (Brown et al., 2004). There are two detectors: the VIMS-VIS which observes from λ = 0.35 - 1.04μm, and VIMS-IR which observes from λ = 0.88 - 5.11μm. VIMS-IR is able to see to Titan's surface through the "methane windows" at λ = 0.93, 1.08, 1.27, 1.59, 2.03, 2.7, 2.8, and 5 μm Sotin et al. (2005), and it is this data used to characterize the dune fields. It should be noted though that all observations taken below $\sim$ 5 μm have blurring effects due to atmospheric scattering from haze particles and other aerosols in Titan's atmosphere, while the 5 μm window is generally free of these effects (Rodriguez et al., 2006). VIMS covered most of Titan's surface (see Figure 6.5), and by characterizing regions by color, Rogriguez *et al.* extracted an equatorial region that correlated with the dune fields they identified in the RADAR maps.

Correlating this type of data allows one to make determinations about the compositions of the dunes to a certain extent, but additional data from the Cassini-Huygens mission would be used to determine specific molecular species.

6.2.2 Composition

"Dark brown" and "dark blue" refer to organic sediment and volatile ices respectively in the literature (Soderblom et al., 2007; Barnes et al., 2008; Rodriguez et al., 2014; Hörst, 2017). From the Cassini-Huygens data, several methods were employed to determine the composition of Titan's surface beyond just "organic sand" and "ice." In the VIMS spectral data there is evidence for water ice (Griffith et al., 2012; Hayne et al., 2014), CO_2 (Barnes et al., 2005; McCord et al., 2008), and nitriles (Clark et al., 2010). There is some conflict between these findings, with suggestions that some surface features are indicative of one species and not the other, though dielectric

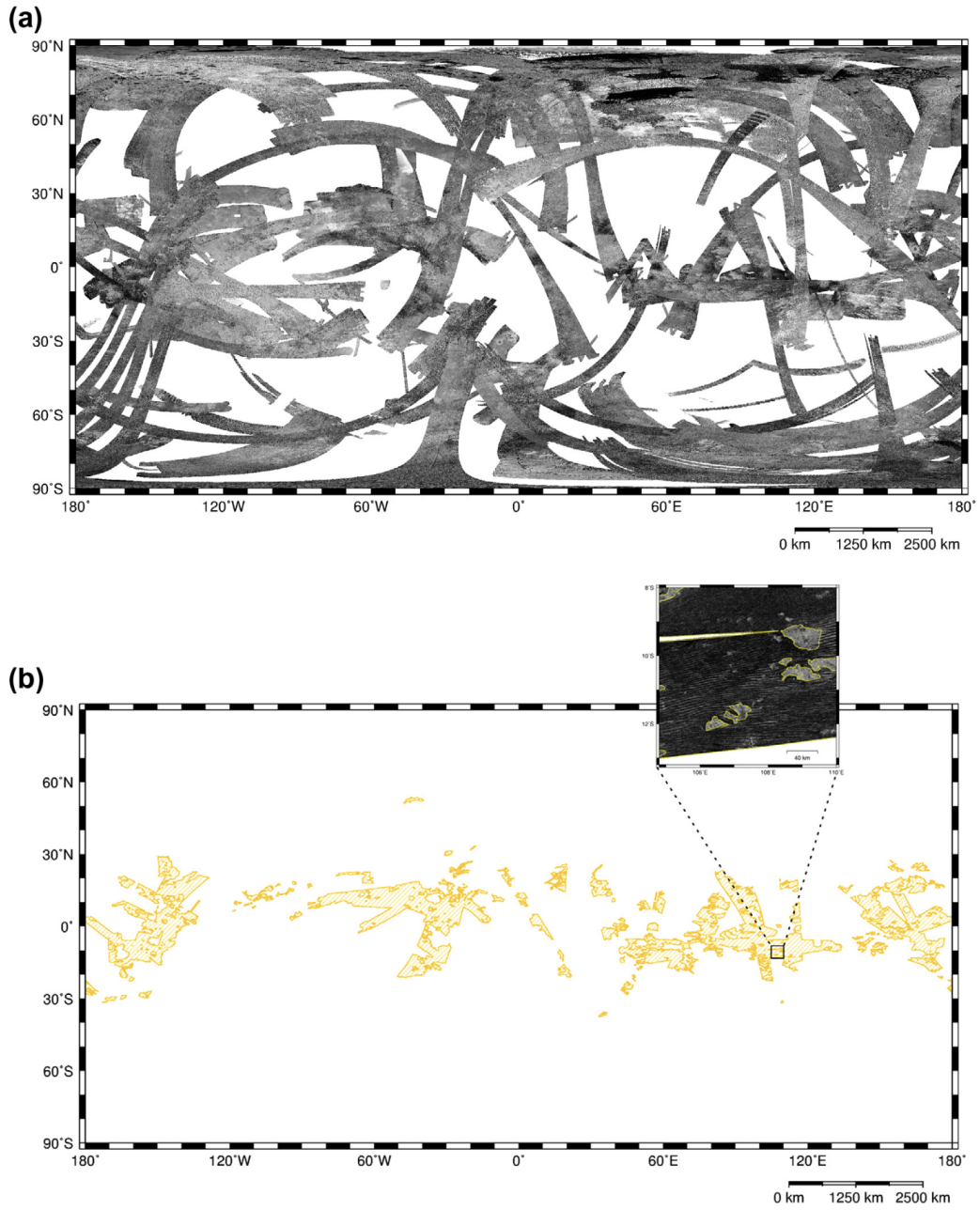

Figure 6.3: Figure 1 from Rodriguez et al. (2014). (Top) Map of Titan as covered by the RADAR instrument. (Bottom) Dune fields highlighted in yellow.

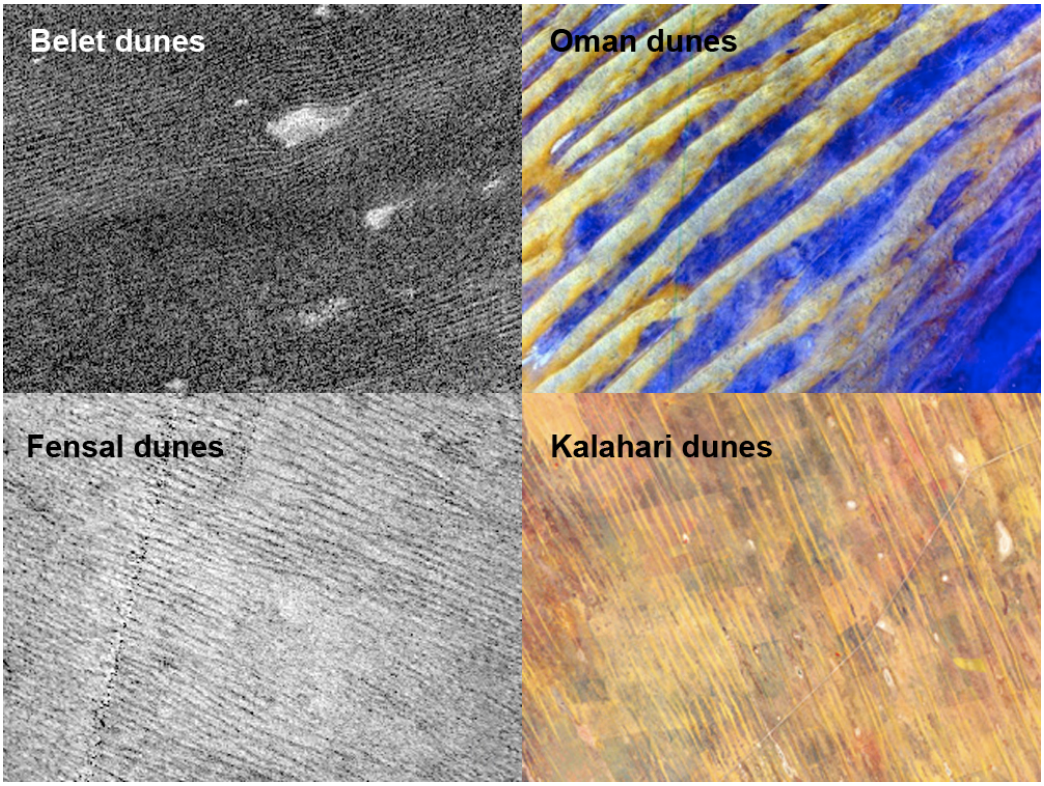

Figure 6.4: Image credit: NASA/JPL-Caltech, and NASA/GSFC/METI/ERSDAC/JAROS and U.S./Japan ASTER Science Team. Cassini RADAR images of Titan's Belet and Fensal dune regions compared with dunes found on Earth in the Oman and Kalahari deserts.

constant measurements of the surface do seem to confirm the presence of water ice (Janssen et al., 2016).

When Huygens landed, its behavior afterward suggested it touched down on something soft (Zarnecki et al., 2005; Lorenz, 2006). It was able to take direct measurements of Titan's surface composition with the GCMS instrument (Niemann et al., 2002, 2005). The GCMS measured the profiles of several species during its descent to the surface. Though it could not quantify a surface composition, it did measure methane evaporating from the surface after being heated by the lander (Niemann et al., 2010; Lorenz et al., 2014). DISR spectral data also suggested the presence of methane ice (Rannou et al., 2016), but there is unfortunately very little additional information on what the dunes are made of.

6.3 Study on Dune Orientation

6.3.1 Formation and Orientation

Dunes on Titan, like dunes on Earth, are formed via aeolian processes. They are eastward propagating, generally parallel to the equation, and roughly 100 m tall (Lorenz

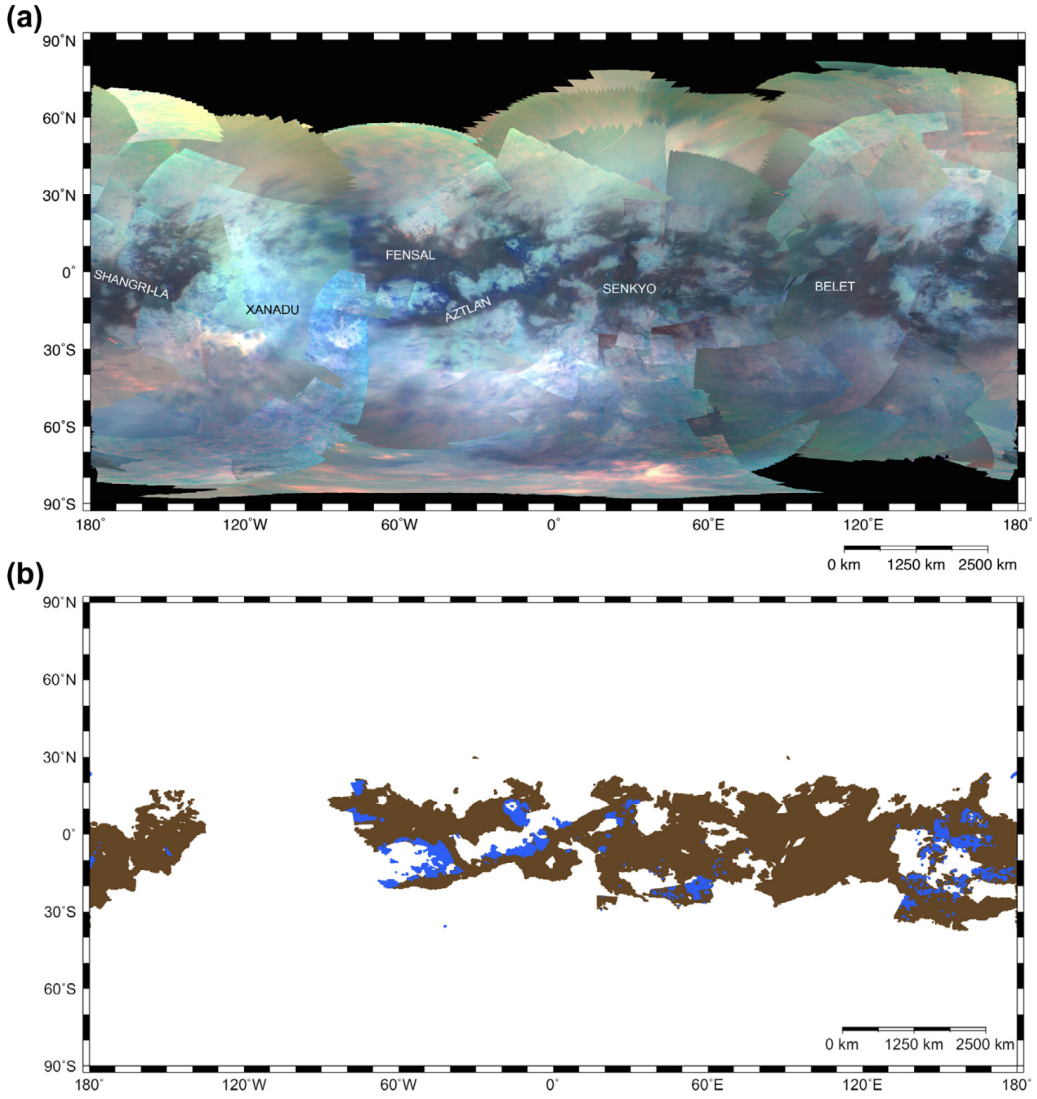

Figure 6.5: Figure 2 from Rodriguez et al. (2014). (Top) Mosaic of VIMS images in false color corresponding to different observing channels. (Bottom) "Dark brown" and "dark blue" regions extracted from ±40°.

et al., 2006b; Radebaugh et al., 2008; Tokano, 2010; Le Gall et al., 2011). Since the dunes are formed by winds, their orientation gives us key insight to the surface wind speeds and directions. It also makes them a great observational comparison point for GCMs.

The dunes being eastward propagating means that they are transported by westerly winds, but there is disagreement over how those winds are propagating at the surface. Are there simply dominant westerlies that varies on diurnal timescales (Lorenz et al., 2006b)? Or are there obtuse bimodal winds as a result of the seasonal Hadley circulation reversal (Tokano, 2008; Barnes et al., 2008)? There are various observations that refute parts of each hypothesis, and unfortunately for modelers, there are many wind parameters that can affect dune transport.

There are a couple of dune migration schemes. If the wind is unidirectional and there is little sand, crescent-shaped dunes form and will migrate on the non-erodable surface beneath them. As the amount of sand increases, the individual crescent-shaped dunes eventually link into longer transverse forms perpendicular to the average wind direction. In the final scheme, the wind is bimodal, and the dunes form long, parallel lines that extend in the resultant wind direction.

To evaluate the resultant dune orientation, there are two common methods. In the first, one takes the ratio of the resultant drift potential (RDP) to the drift potential (DP), the latter of which is described by the equation:

$$q_i = v^2(v - v_t)t \text{ summed over all directions } i \tag{6.1}$$

The resultant DP vector is the RDP (Fryberger et al., 1979). where q is the annual rate of sand drift for a specified direction, v is the wind velocity, v_t is the threshold wind velocity, and t is the percentage of time that the wind blew from the specified direction. Longitudinal dunes are parallel to the resultant direction, while transverse dunes are perpendicular to it. The second method introduces the concept of the maximum gross bedform-normal transport (GBNT) originally described by Rubin & Hunter (1987). In the GBNT, dunes become aligned such that the gross transport of sand normal to the bedform is maximized. For an arbitrary bedform, the transport is described by the equation:

$$T = D|\sin\alpha| + S|\sin\theta - \alpha| \tag{6.2}$$

T is maximized when:

$$\alpha_{GBNT} = \tan^{-1}\left[\pm\frac{R + |\cos\theta|}{|\sin\theta|}\right] \tag{6.3}$$

This is for the case where the windflow is not interrupted by the dune, but when it is interrupted by the dune, then we have the bedform instability case (BIM), and the orientation angle is:

$$\alpha_{BIM} = \frac{1}{2}\tan^{-1}\left[\frac{sin2\theta}{\cos 2\theta + R}\right] \tag{6.4}$$

There is a final scheme proposed by Courrech du Pont et al. (2014) based on experimental observations known as the fingering mode (FM). If the bimodal wind forms an obtuse angle, and the sand source is fixed, the dune orientation becomes an elongated "finger" aligned with the average sand flux vector. The dune's orientation is then described by the equations:

$$\alpha_{FM} = \tan^{-1}\left[\frac{\sin\theta}{R + \cos\theta}\right] \tag{6.5}$$

when $\gamma = \beta H/W$ (the dune aspect ratio multiplied by a dimensionless factor that accounts for wind acceleration) is equal to zero and

$$\alpha_{FM} = \tan^{-1}\left[\frac{\sin\theta}{\sqrt{R} + \cos\theta}\right] \tag{6.6}$$

when $\gamma = +\infty$.

Finally, the sand flux (the rate at which the dunes grow) can be described by the equation (after Lorenz et al. (1995), an update to Equation 6.1):

$$q = 2.6\frac{\rho_a}{g}(v_* - v_{*,t})(v_* + v_{*,t})^2 \tag{6.7}$$

where ρ_a is the atmosphere's density, g is the surface gravity, and v_* is the friction speed, with $v_{*,t}$ being the threshold friction speed (the windspeed necessary to overcome friction forces that would preclude dune growth). The rate at which the dune will migrate (move perpendicular to the dune's crest) is

$$c_y = \frac{q_y}{\rho_d H} \tag{6.8}$$

where q_y is the meridional sand flux, ρ_d is the sand material density, and H is the dune height (on average 100 m from observations (Lorenz et al., 2006b)).

In this study we use the surface winds output from the TitanWRF (Richardson et al., 2007; Newman et al., 2011) General Circulation Model (GCM) to predict dune transport directions and orientations in these three modes and compare them to the observed dune orientations.

6.3.2 TitanWRF

The TitanWRF GCM (described in Section 4.3) is a 3-D general circulation model that is highly modular. For this study, we calculate dune orientations with two models: a "flat" model that contains no topography, and a model that contains topography from the SARTopo map of Lorenz et al. (2013). There have been improvements made to TitanWRF's handling of topography, described in Section 4.3. The models are run at a resolution of $5.625° \times 5°$ in longitude and latitude respectively, with 54 vertical "modified sigma" σ' levels from the surface to approximately 500 km. The flat model is run for $\sim$ 50 (in-simulation) years and the model with topography is

run for ~ 70 years. In order to capture the diurnal variations in winds that can affect dune orientation, we selected a time frame from this model and ran it at half hour timesteps.

6.3.3 Results

First, we will look at the surface winds. The dunes are primarily found in the mid-latitudes, and observationally should be formed by westerlies. When calculating the surface winds in the flat and (see Figures 6.6 and 6.7). In the model with topography, we do not often produce strong westerlies in latitudes between $\pm 20°$, though there periods (such as the one shown in Figure 6.6) where some regions that correspond to known dune fields do have eastward-propagating winds. In the model without topography, we produce even fewer westerlies in latitudes between $\pm 20°$. There are strong westerlies (and easterlies) at higher latitudes, but as the dunes are observed to be in Titan's equatorial regions, we do not focus on times in the model when those are maximized.

The resultant dune growth directions and orientations are shown in Figures 6.8 and 6.9, where we focus specifically on a region at the center of the map; red lines are the orientation as predicted by the transport mode, and black lines are the dune transportation and elongation direction. The arrows at both ends just mean there is no favored direction for transport. Both plots have a threshold friction velocity of 0 m/s (i.e. any winds can shift the dunes). In order to get the dune orientations, we select a range of years at the ends of the simulation where windspeeds are fastest, as over time the winds shift the dunes. We see that there is generally little difference between the GBNT and BIM methods of calculation, which is expected since they are conceptually very similar.

In the case with no topography we do get dunes consistently aligned along the equator, but that is unfortunately not the case for the model with topography. This has generally been the case for other studies that use GCM outputs with topography included (e.g. Tokano (2010)).

6.4 Conclusion

We use the surface winds calculated in two different TitanWRF models to predict dune orientations in three different modes. The output from a model with topography and one without is used to calculate transport direction and dune orientation angles according to 1) the gross bedform-normal transport mode, 2) the bedform instability mode, and 3) the finger mode. In the model without topography, we are able to produce dunes oriented along the equator (which is in agreement with observations), but little such alignment is seen in the model with topography. There still remain many gaps in our knowledge of how topography in GCMs is affecting surface winds and the resultant dune orientation predictions.

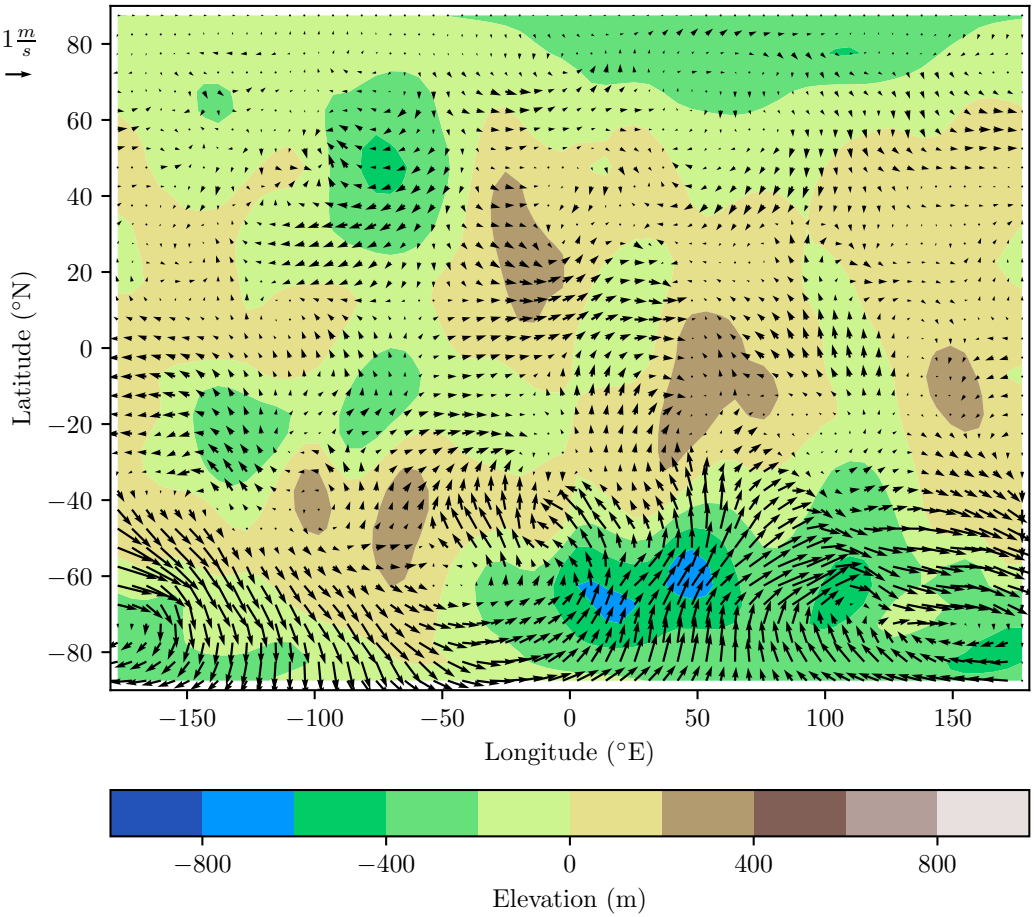

Figure 6.6: Surface winds in TitanGCM model with topography at $t = 64$ years, $L_S = 165.15°$. At this snapshot in the model there are the strongest observed westerlies in the equatorial region. There are other periods of time with strong westerlies, but they are at higher latitudes.

Appendix

6.A Definitions of Symbols

6.B Numerical Constants

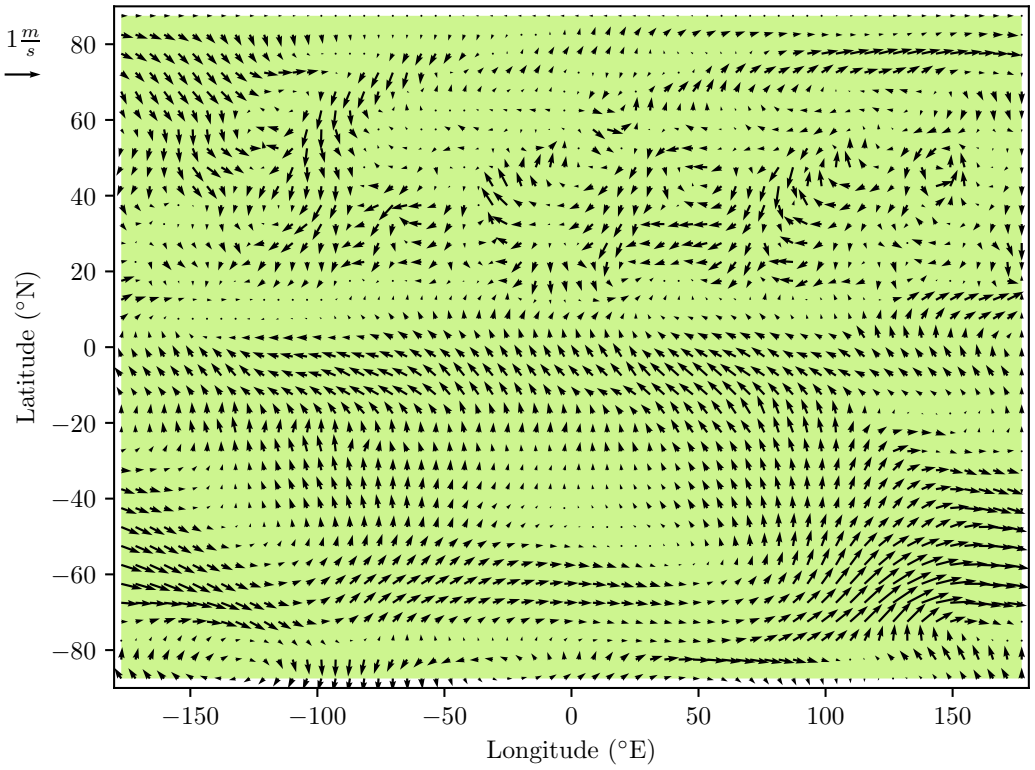

Figure 6.7: Surface winds in TitanGCM model without topography at $t = 47$ years, $L_S = 176.07°$. In this model we observe no westerlies in the equatorial region, which would explain why we see poor agreement between the predicted dune orientations and observations discussed later in this chapter.

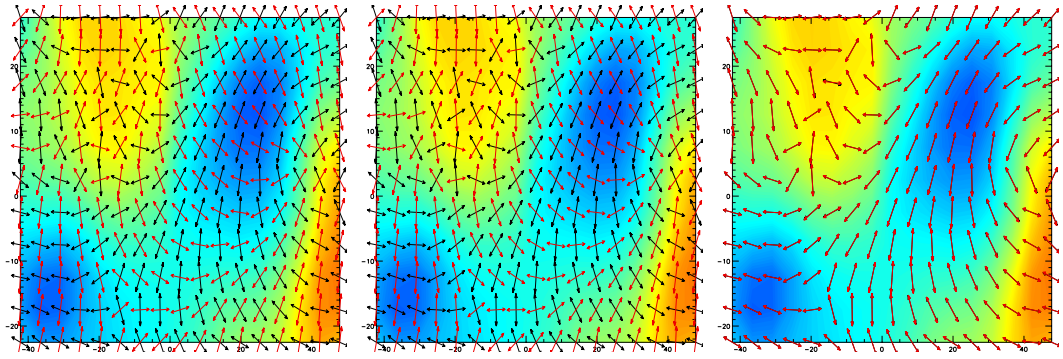

Figure 6.8: Predicted dune orientations from TitanWRF GCM output of surface winds in model with topography resulting from winds in years 64 to 70. X-axis is longitude in degrees E, Y-axis is latitude in degrees N.

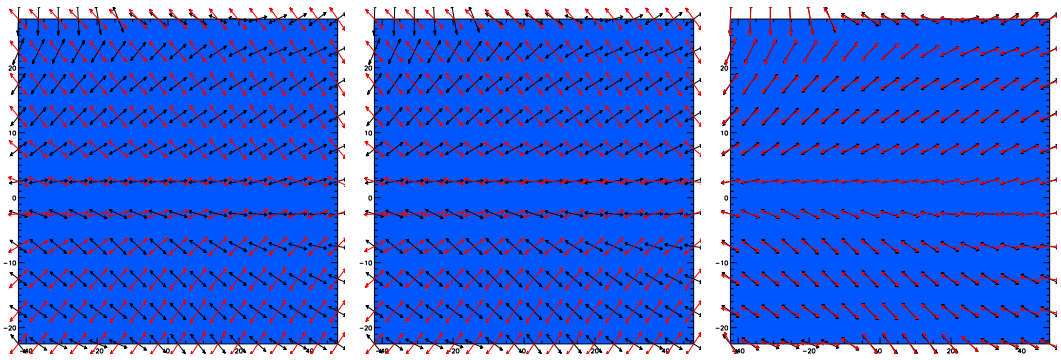

Figure 6.9: Predicted dune orientations from TitanWRF GCM output of surface winds in model without topography in years 47 to 50. X-axis is longitude in degrees E, Y-axis is latitude in degrees N.

Variable	Description	Equation
q_i	Annual sand rate drift	6.1
v	Wind velocity	6.1
t	Time	6.1
T	Sand transport	6.2
D	Transport from dominant vector	6.2
S	Transport from subordinate vector	6.2
α	Angle between dominant vector and bedform	6.2
θ	Divergence angle between transport vectors	6.2
α_{GBNT}	Dune orientation angle in GBNT mode	6.3
R	Ratio of D:S	6.3
α_{BIM}	Dune orientation angle in BIM mode	6.4
α_{FM}	Dune orientation in fingering mode	6.6
ρ_a	Atmospheric density	6.7
v_*	Friction speed	6.7
c_y	Sand migration rate	6.8
q_y	Meridional sand flux	6.8
ρ_d	Sand material density	6.8

Table 6.1: Descriptions of symbols with location of first appearance

Description	Symbol	Value	Equation
g	Surface gravity	1.35 m/s^2	6.7
H	Dune height	100 m	6.8

Table 6.2: Values for constants

Finally, as per my advisor's request:

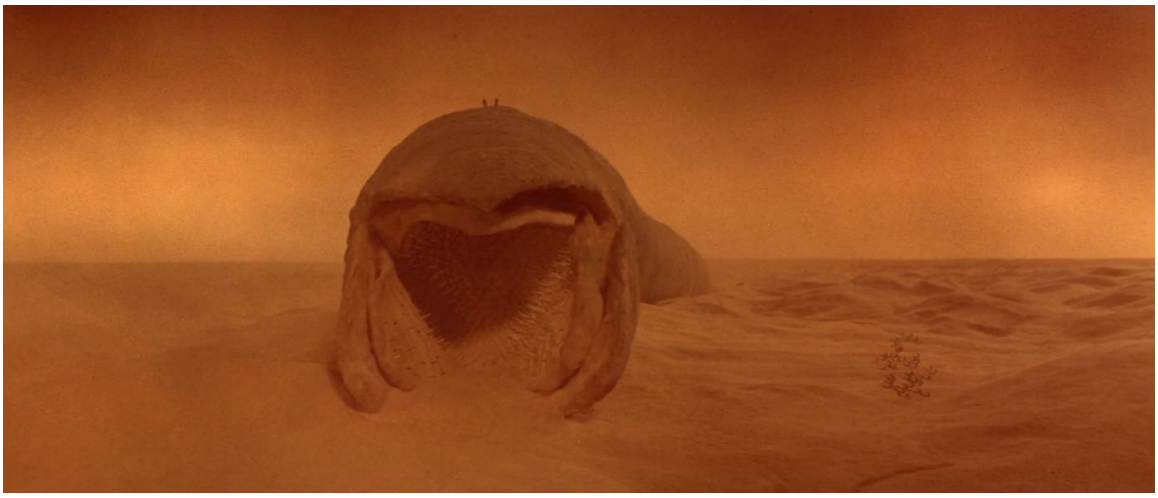

Figure 6.10: ©Universal Pictures, 1984. *Turning the sandworm.* "Deep in the human unconscious is a pervasive need for a logical universe that makes sense. But the real universe is always one step beyond logic." - Frank Herbert, *Dune*

Chapter 7

Conclusions & Potential for Future Work

7.1 Summary

The main contributions of this thesis to the study of Titan's atmosphere are in improvements to computational modeling methods that incorporate more realism than ever before and in furthering our understanding of Titan's energy and materials budget as it pertains to atmospheric chemistry. In all of the studies included in this thesis, I have intertwined the theoretical with the observational: in some cases using in situ measurements of Titan's atmosphere as model input, and in others comparing model results with telescope and probe data. To summarize each chapter:

- Chapter 2: Titan orbits through a rich particle environment, with infalling material coming from several sources. Interplanetary dust makes up the bulk of the flux onto Titan, the composition of which is predominantly that of carbonaceous chondrites, with some water and volatile ices from Saturn's E-ring, Enceladus's plumes, and cometary particles. More my studies on how meteoroids contribute to atmospheric chemistry on Titan, I developed a computational model for meteor entry. Through this research I also discovered an egregious error in meteor dynamics models that has persisted in the literature, a lesson for all to check sources that have been cited for decades without real reflection.

- Chapter 3: Using the computational model described in Chapter 2 and an improved flux model based on observations, I calculated how much energy meteoroids can deliver to an atmosphere via shocks, and subsequently calculated the expected amount of hydrocarbon and molecular hydrogen products. This study showed that meteoroids contribute more energy than previously thought, in the optimistic case delivering just as much if not more energy than magnetospheric ions and UV photons. They also deliver energy to parts of the atmosphere not reached by the ions and photons, such as the mid-stratosphere and lower and the night side of the moon. Thus, one cannot discount their contributions to atmospheric chemistry in models of Titan's atmosphere.

- Chapter 4: In this chapter I review the current state of Titan General Circulation Models (GCMs) and discuss my improvements on the TitanWRF GCM. It is incredibly difficult to model terrestrial worlds with high fidelity. Current Titan GCMs are sometimes able to reproduce observed superrotating jets in the simplified case of a flat planet (one with no topography). Many of these models also do not include dynamical processes such as the methane cycle, haze dynamics, or accurate profiles as measured by Cassini. TitanWRF is one of the most "complete" GCMs in that it does include many of the processes that are omitted in previous models, though it does still have its limits. I improved how TitanWRF was handling vertical diffusion processes, and completed a wave analysis study to determine differences between my improved model and previous versions.

- Chapter 5: For the first time, I present results from a 3-D GCM that includes the observed topography that reproduces and sustains a superrotating jet. Top wind speeds in the model at the model top ($\sim$ 400 km) are only 25 m/s slower than some ALMA observations of the same altitude, and lower in the model atmosphere we produce the same windspeeds as observed. There are plans to extend the model top in the near future, which hopefully will allow us to reproduce the higher windspeeds at the 400 km level.

- Chapter 6: Using the TitanWRF predictions for surface windspeeds, I calculate expected dune orientations. The Dragonfly mission will land a rotocopter in Titan's equatorial desert, where it will traverse the dune fields to sample the atmosphere, surface, and subsurface. Understanding how the dunes are formed and shift is important for Dragonfly mission operations as it pertains to the rotocopter's route. With the improved model, we see improvements over previous attempts to predict dune orientations.

7.2 Future Work

Studying the Chemical Reaction Chains from Meteoroid Material

The natural follow-up to my study on meteor-driven shocks is to calculate how this affects the chemical profiles of hydrocarbons and hydrogen in Titan's atmosphere, and the creation and evolution of haze particles in the detached haze layer at $\sim$ 500 km. I have shown that there is meteoroid-driven shock chemistry taking place in the stratosphere and lower, in regions of the atmosphere not accessible to UV photons and magnetospheric ions which are generally the largest sources of energy in Titan's atmosphere. In the optimistic particle flux case, meteoroids actually contribute more energy than magnetospheric ions at the same altitudes.

How the detached haze layer is formed and evolves over time is an open area of research. With shock chemistry production peaking at the same altitude as this layer, it begs the question: how much do these particles contribute to haze chemistry and dynamics? A potential project will be to calculate the tholin production rate as caused by the chemistry driven by meteoroids.

Extending the TitanWRF Model Top

One issue across the Titan GCMs is that they only extend about 500 km above the surface, when we are trying to study phenomena at or above this cut-off. Boundary conditions at the model top can stunt the growth of the stratospheric jet by hindering upper atmosphere circulation. If the circulation is not as robust, the winter hemisphere's adiabatic heating is also lower than required to generate the observed windspeeds and temperature gradients. There is a preliminary version of the model with a higher model top of $\sim$ 700 m, but it very quickly "blows up" in temperature for reasons we are still trying to understand.

In addition to extending the model top in TitanWRF, I am also exploring coupling TitanWRF GCM output to a different GCM that models the thermosphere. The Thermospheric GCM (TGCM) was developed by Müller-Wodarg et al. (2000) to simulate the atmosphere from an altitude of 600 km to the top of the atmosphere at 1400 km. I. C. F. Müller-Wodarg and I are working to derive a model floor for the TGCM from the model top of TitanWRF in order to bridge the 200 km gap between the two models' altitude limits and further improve TitanWRF's generation of the stratospheric superrotating jet in models with topography.

Using Models to Detect New Molecular Species

For the last ten to fifteen years, there has been progress made in the field of computational modeling as applied to atmospheric transmission spectroscopy. Using general circulation models (GCMs) to simulate atmospheric dynamics, radiative transfer codes to produce spectra, and a combination of the two, we have an increasing understanding of how atmospheric dynamics inform chemistry, which in turn inform spectroscopy. Fortunately, this growth in computational knowledge is coincident with the advent of new space- and ground-based telescopes that are specifically tasked with studying the atmospheres of planets and exoplanets. Mid-resolution (R $\sim$ 3,000 - 25,000) and high-resolution (R $\geq$ 25,000) spectrographs are now in operation at Magellan, Keck, the European Very Large Telescope, the Stratospheric Observatory for Infrared Astronomy (SOFIA), the James Webb Space Telescope (JWST), and more, and will be included on upcoming telescopes such as the Giant Magellan Telescope, the Nancy Grace Roman Space Telescope, Large Ultraviolet Optical Infrared Surveyor Telescope.

Recent studies have shown that a combination of observed and synthetic spectroscopic data can accurately determine atmospheric conditions of hot Jupiters (e.g. Flowers et al. (2019); Beltz et al. (2021); Wardenier et al. (2021); Deitrick et al. (2022)). Studies of this type have the benefit of improving our understanding of the processes that are responsible for the atmospheric dynamics that are being observed as well as improving our understanding of the models we employ from making adjustments to the models to better fit observations. There has been preliminary work done in this vein for smaller, terrestrial exoplanets (e.g. Fauchez et al. (2019, 2022); May et al. (2021)) but given the lack of mid- or high-resolution spectra of terrestrial exoplanets with high signal-to-noise (S/N) and the general difficulty of creating high fidelity GCMs that account for terrain, the proof of concept is largely theoretical for smaller bodies until such a time as we can take space-based observations, ground-based extremely large telescope facilities come online, and we improve our

terrestrial GCMs. When it comes to work inside of the solar system though, there is surprisingly little research in trying to understand the atmospheres of terrestrial bodies through a combination of observed and synthetic transmission spectra, though there are several GCMs based on Earth meteorological models, as well as radiative transfer models for retrieval of atmospheric parameters from spectra. Titan is a prime candidate for this kind of study, since there are a couple of 3D Titan GCMs as well as spectroscopic observations of its atmosphere. While the main components of its atmosphere have been well-established, we continue to search for signatures of more complex organic molecules in existing data. Given Titan's relevance to the decadal surveys' and NASA's astrobiological and mission goals, it is highly likely that within the next handful of years, more observations and GCM development will be not only required, but prioritized.

I have proposed to continue the work to analyze Atacama Large Millimeter Array (ALMA) data using the NEMESIS code (Irwin et al., 2008) in tandem with the TitanWRF GCM. I would generate spectra of the models using the NEMESIS code with model inputs from TitanWRF and then retrieve atmospheric parameters from those spectra with observations from ALMA, SOFIA, and/or other sources.

Bibliography

Achterberg, R. K., Conrath, B. J., Gierasch, P. J., Flasar, F. M., & Nixon, C. A. 2008, Icarus, 194, 263

Achterberg, R. K., Gierasch, P. J., Conrath, B. J., Michael Flasar, F., & Nixon, C. A. 2011, Icarus, 211, 686

Aharonson, O., Hayes, A. G., Lunine, J. I., et al. 2009, Nature Geoscience, 2, 851

Allen, M., Yung, Y. L., & Pinto, J. P. 1980, ApJ, 242, L125

Altobelli, N., Kempf, S., Landgraf, M., et al. 2003, Journal of Geophysical Research: Space Physics, 108

Anderson, J. D. 2019, Hypersonic and High Temperature Gas Dynamics, 3rd Ed. (AIAA)

Arakawa, A., & Lamb, V. R. 1981, Monthly Weather Review, 109, 18

Atkins, P. W. 1986, Physical Chemistry, 3rd edn. (Oxford University Press), 643–662, table 26.2

Bar-Nun, A., & Shaviv, A. 1975, Icarus, 24, 197

Barnes, J. R., Pollack, J. B., Haberle, R. M., et al. 1993, J. Geophys. Res., 98, 3125

Barnes, J. W., Lorenz, R. D., Radebaugh, J., et al. 2015, Planetary Science, 4, 1

Barnes, J. W., Brown, R. H., Turtle, E. P., et al. 2005, Science, 310, 92

Barnes, J. W., Brown, R. H., Soderblom, L., et al. 2008, Icarus, 195, 400

Barnes, J. W., Brown, R. H., Soderblom, J. M., et al. 2009, Icarus, 201, 217

Beltz, H., Rauscher, E., Brogi, M., & Kempton, E. M. R. 2021, AJ, 161, 1

Bird, M. K., Dutta-Roy, R., Heyl, M., et al. 2002, Space Sci. Rev., 104, 613

Bird, M. K., Allison, M., Asmar, S. W., et al. 2005, Nature, 438, 800

Bockelée-Morvan, D. 2011, Proceedings of the International Astronomical Union, 7, 261

Borucki, W. J., Giver, L. P., McKay, C. P., Scattergood, T., & Parris, J. E. 1988, Icarus, 76, 125

Borucki, W. J., & McKay, C. P. 1987, Nature, 328, 509

Bottke, W. F., Nesvornỳ, D., Grimm, R. E., Morbidelli, A., & O'Brien, D. P. 2006, Nature, 439, 821

Bourke, W. 1972, Monthly Weather Review, 100, 683

Brace, L., Hoegy, W., & Theis, R. 1988, Journal of Geophysical Research: Space Physics, 93, 7282

Briegleb, B. P. 1992, J. Geophys. Res., 97, 7603

Britt, D. T., & Consolmagno, G. 2003, Meteoritics & Planetary Science, 38, 1161

Bronshten, V. A. 1983, *Physics of Meteoric Phenomena* (D. Reidel Publishing Company)

Brown, R. H., Baines, K. H., Bellucci, G., et al. 2004, Space Sci. Rev., 115, 111

Buchwald, V. F. 1975, Arizona: State University

Busch, M. W., Ostro, S. J., Benner, L. A., et al. 2011, Icarus, 212, 649

Cabane, M., & Chassefière, E. 1995, Planet. Space Sci., 43, 47

Campbell-Brown, M. D., & Koschny, D. 2004, Astronomy & Astrophysics, 418, 751

Cassini Collaboration. 2019, Cassini Final Mission Report, Vol. 1 (NASA Jet Propulsion Laboratory California Institute of Technology), 97–108

Chameides, W. L. 1979, Nature, 277, 123

Chameides, W. L., & Walker, J. C. G. 1981, Origins of Life, 11, 291

Chyba, C., & Sagan, C. 1992, Nature, 355, 125

Chyba, C. F., Thomas, P. J., & Zahnle, K. J. 1993, Nature, 361, 40

Civiš, S., Knížek, A., Ivanek, O., et al. 2017, Nature Astronomy, 1, 721

Clark, R. N., Curchin, J. M., Barnes, J. W., et al. 2010, Journal of Geophysical Research (Planets), 115, E10005

Cleaves, H. J., Neish, C., Callahan, M. P., et al. 2014, Icarus, 237, 182

Coates, A. J., Crary, F. J., Lewis, G. R., et al. 2007, Geophys. Res. Lett., 34, L22103

Cochran, A. L., Levasseur-Regourd, A.-C., Cordiner, M., et al. 2015, Space Science Reviews, 197, 9

Collins, W., Rasch, P., Boville, B., et al. 2004, NCAR Technical Note, TN-464+STR

Collins, W. D., Rasch, P. J., Boville, B. A., et al. 2006, Journal of Climate, 19, 2144

Colwell, J. 1994, Planetary and Space Science, 42, 1139

Cordiner, M., Garcia, E., Cosentino, R., Teanby, N., & Nixon, C. 2020a, in European Planetary Science Congress, EPSC2020–424

Cordiner, M. A., Garcia-Berrios, E., Cosentino, R. G., et al. 2020b, ApJ, 904, L12

Cordiner, M. A., Teanby, N. A., Nixon, C. A., et al. 2019, AJ, 158, 76

Corlies, P., Hayes, A. G., Birch, S. P. D., et al. 2017, Geophys. Res. Lett., 44, 11,754

Courrech du Pont, S., Narteau, C., & Gao, X. 2014, Geology, 42, 743

Courtin, R., Kim, S. J., & Bar-Nun, A. 2015, A&A, 573, A21

Coustenis, A., & Bezard, B. 1995, Icarus, 115, 126

Coustenis, A., Jennings, D. E., Nixon, C. A., et al. 2010, Icarus, 207, 461

Coy, B., Nixon, C., Rowe-Gurney, N., et al. 2021, in AAS/Division for Planetary Sciences Meeting Abstracts, Vol. 53, AAS/Division for Planetary Sciences Meeting Abstracts, 402.01

Crary, F. J., Magee, B. A., Mandt, K., et al. 2009, Planet. Space Sci., 57, 1847

Cui, J., Yelle, R. V., Vuitton, V., et al. 2009, Icarus, 200, 581

Cuzzi, J. N., & Durisen, R. H. 1990, Icarus, 84, 467

Daley, R., Girard, C., Henderson, J., & Simmonds, I. 1976, Atmosphere, 14, 98

Davies, M. E., Abalakin, V. K., Brahic, A., et al. 1992, Celestial Mechanics and Dynamical Astronomy, 53, 377

Dean, A. J., Hanson, R. K., & Bowman, C. T. 1991, Symposium on Combustion, Vol. 23 (Elsevier), 259–265

Deitrick, R., Heng, K., Schroffenegger, U., et al. 2022, MNRAS, 512, 3759

Dell'Aglio, M., De Giacomo, A., Gaudiuso, R., et al. 2010, Geochimica et Cosmochimica Acta, 74, 7329

Divine, N. 1993, J. Geophys. Res., 98, 17029

Dougherty, M. K., Kellock, S., Southwood, D. J., et al. 2004, Space Sci. Rev., 114, 331

Elachi, C., Allison, M. D., Borgarelli, L., et al. 2004, Space Sci. Rev., 115, 71

Elachi, C., Wall, S., Allison, M., et al. 2005, Science, 308, 970

Elachi, C., Wall, S., Janssen, M., et al. 2006, Nature, 441, 709

Eliasen, E., Machenhauer, B., & Rasmussen, E. 1970, On a numerical method for integration of the hydrodynamical equations with a spectral representation of the horizontal fields (Kobenhavns Universitet, Institut for Teoretisk Meteorologi)

Elkins-Tanton, L., Asphaug, E., Bell III, J., et al. 2020, Journal of Geophysical Research: Planets, 125, e2019JE006296

Emonts, B., Raba, R., Montesino Pouzols, F., et al. 2019, in Astronomical Society of the Pacific Conference Series, Vol. 523, Astronomical Data Analysis Software and Systems XXVII, ed. P. J. Teuben, M. W. Pound, B. A. Thomas, & E. M. Warner, 265

English, M. A., Lara, L. M., Lorenz, R. D., Ratcliff, P. R., & Rodrigo, R. 1996, Advances in Space Research, 17, 157

Esposito, L. W., Barth, C. A., Colwell, J. E., et al. 2004, Space Sci. Rev., 115, 299

Fauchez, T. J., Turbet, M., Villanueva, G. L., et al. 2019, ApJ, 887, 194

Fauchez, T. J., Villanueva, G. L., Sergeev, D. E., et al. 2022, PSJ, 3, 213

Ferus, M., Kubelík, P., Knížek, A., et al. 2017, Scientific Reports, 7, 6275

Ferus, M., Petera, L., Koukal, J., et al. 2020, Icarus, 341, 113670

Fink, U. 2009, Icarus, 201, 311

Flasar, F. M., Samuelson, R. E., & Conrath, B. J. 1981, Nature, 292, 693

Flasar, F. M., Kunde, V. G., Abbas, M. M., et al. 2004, Space Sci. Rev., 115, 169

Flowers, E., Brogi, M., Rauscher, E., Kempton, E. M. R., & Chiavassa, A. 2019, AJ, 157, 209

Flowers, E., & Chyba, C. in final review, AJ

Flowers, E., Newman, C., Chyba, C., Lee, C., & Toigo, A. in prep. 2023c

Flowers, E., Newman, C., Lian, Y., Lee, C., & Toigo, A. in prep. 2023a

—. in prep. 2023b

Flynn, G. J. 2004, Earth Moon and Planets, 95, 361

Folkner, W. M., Asmar, S. W., Border, J. S., et al. 2006, Journal of Geophysical Research: Planets, 111, https://agupubs.onlinelibrary.wiley.com/doi/pdf/10.1029/2005JE002649

Fridman, A. 2008, Plasma Chemistry (Cambridge University Press)

Friedson, A. J., West, R. A., Wilson, E. H., Oyafuso, F., & Orton, G. S. 2009, Planet. Space Sci., 57, 1931

Frierson, D. M. W. 2007, Journal of Atmospheric Sciences, 64, 1959

Fryberger, S. G., et al. 1979

Fulchignoni, M., Ferri, F., Angrilli, F., et al. 2002, Space Sci. Rev., 104, 395

—. 2005, Nature, 438, 785

Gainsforth, Z., Butterworth, A. L., Stodolna, J., et al. 2015, M&PS, 50, 976

Galimov, E., Kolotov, V., Nazarov, M., et al. 2013, Geochemistry International, 51, 522

Gibbard, S. G., Macintosh, B., Gavel, D., et al. 1999, Icarus, 139, 189

Gierasch, P. J. 1975, Journal of Atmospheric Sciences, 32, 1038

Gordon, C. T., & Stern, W. F. 1982, Monthly Weather Review, 110, 625

Grebowsky, J. M. 1981, J. Geophys. Res., 86, 1537

Griffith, C. A., Doose, L., Tomasko, M. G., Penteado, P. F., & See, C. 2012, Icarus, 218, 975

Grigorieva, A., Thébault, P., Artymowicz, P., & Brandeker, A. 2007, A&A, 475, 755

Grün, E., Zook, H. A., Fechtig, H., & Giese, R. H. 1985, Icarus, 62, 244

Gurnett, D. A., Ansher, J. A., Kurth, W. S., & Granroth, L. J. 1997, Geophys. Res. Lett., 24, 3125

Gurnett, D. A., Kurth, W. S., Kirchner, D. L., et al. 2004, Space Sci. Rev., 114, 395

Hahn, J. M., Zook, H. A., Cooper, B., & Sunkara, B. 2002, Icarus, 158, 360

Han, D., Poppe, A. R., Piquette, M., Grün, E., & Horányi, M. 2011, Geophysical research letters, 38

Hanel, R., Conrath, B., Flasar, F. M., et al. 1981, Science, 212, 192

Hansen, C. J., Esposito, L., Stewart, A. I. F., et al. 2006, Science, 311, 1422

Hartle, R. E., Sittler, E. C., Neubauer, F. M., et al. 2006, Geophys. Res. Lett., 33, L08201

Hauser, M. G., Gillett, F. C., Low, F. J., et al. 1984, ApJ, 278, L15

Hayes, A. G., Aharonson, O., Lunine, J. I., et al. 2011, Icarus, 211, 655

Hayne, P. O., McCord, T. B., & Sotin, C. 2014, Icarus, 243, 158

Hill, K. A., Rogers, L. A., & Hawkes, R. L. 2004, Earth Moon and Planets, 95, 403

Hillier, J. K., Green, S. F., McBride, N., et al. 2007, Icarus, 190, 643

Hills, J. 1981, Astronomical Journal, vol. 86, Nov. 1981, p. 1730-1740., 86, 1730

Hong, S.-Y., & Pan, H.-L. 1996, Monthly Weather Review, 124, 2322

Horanyi, M., Hoxie, V., James, D., et al. 2009, New Horizons: Reconnaissance of the Pluto-Charon System and the Kuiper Belt, 387

Hörst, S. M. 2017, Journal of Geophysical Research (Planets), 122, 432

Hörst, S. M., Vuitton, V., & Yelle, R. V. 2008, Journal of Geophysical Research (Planets), 113, E10006

Hörst, S. M., Yoon, Y. H., Ugelow, M. S., et al. 2018, Icarus, 301, 136

Hourdin, F., Le van, P., Forget, F., & Talagrand, O. 1993, Journal of Atmospheric Sciences, 50, 3625

Hourdin, F., & Talagrand, O. 1992, in AAS/Division for Planetary Sciences Meeting Abstracts, Vol. 24, AAS/Division for Planetary Sciences Meeting Abstracts #24, 32.09

Hourdin, F., Talagrand, O., Sadourny, R., et al. 1995, Icarus, 117, 358

Hourdin, F., Musat, I., Bony, S., et al. 2006, Climate Dynamics, 27, 787

Hubbard, W. B., Sicardy, B., Miles, R., et al. 1993, A&A, 269, 541

Hui, M.-T., Jewitt, D., Yu, L.-L., & Mutchler, M. J. 2022, The Astrophysical Journal Letters, 929, L12

Humes, D. H. 1980, J. Geophys. Res., 85, 5841

Hutzell, W. T., McKay, C. P., Toon, O. B., & Hourdin, F. 1996, Icarus, 119, 112

Huygens, C. 1659, Cristiani Hugenii... Systema Saturnium sive de causis mirandorum Saturni phaenomenon et comite ejus planeta novo (The Hague : Adriaan Vlacq), doi:10.3931/e-rara-3178

Huygens, C. 1684, Christiani Hugenii ... Astroscopia compendiaria, tubi optici molimine liberata (Leers)

Ip, W. H. 1990, Nature, 345, 511

Irwin, P. G. J., Teanby, N. A., de Kok, R., et al. 2008, J. Quant. Spec. Radiat. Transf., 109, 1136

Israel, G., Cabane, M., Brun, J. F., et al. 2002, Space Sci. Rev., 104, 433

Izawa, M., Nesbitt, H., MacRae, N., & Hoffman, E. 2010, Earth and Planetary Science Letters, 298, 443

Janches, D., Heinselman, C. J., Chau, J. L., Chandran, A., & Woodman, R. 2006, Journal of Geophysical Research (Space Physics), 111, A07317

Janssen, M. A., Le Gall, A., Lopes, R. M., et al. 2016, Icarus, 270, 443

Karkoschka, E., & Lorenz, R. D. 1997, Icarus, 125, 369

Kim, S. J., & Courtin, R. 2013, A&A, 557, L6

Kim, S. J., Jung, A., Sim, C. K., et al. 2011, Planet. Space Sci., 59, 699

Kliore, A. J., Anderson, J. D., Armstrong, J. W., et al. 2004, Space Sci. Rev., 115, 1

Kok, J. F., Parteli, E. J. R., Michaels, T. I., & Karam, D. B. 2012, Reports on Progress in Physics, 75, 106901

Koschny, D., & Borovicka, J. 2017, WGN, Journal of the International Meteor Organization, 45, 91

Koskinen, T. T., Yelle, R. V., Snowden, D. S., et al. 2011, Icarus, 216, 507

Kostiuk, T., Fast, K. E., Livengood, T. A., et al. 2001, Geophysical Research Letters, 28, 2361

Krasnopolsky, V. A. 2009, Icarus, 201, 226

Krimigis, S. M., Mitchell, D. G., Hamilton, D. C., et al. 2004a, Space Sci. Rev., 114, 233

—. 2004b, Space Sci. Rev., 114, 233

Kuiper, G. P. 1944, ApJ, 100, 378

Kunde, V. G., Aikin, A. C., Hanel, R. A., et al. 1981, Nature, 292, 686

Landgraf, M., Liou, J. C., Zook, H. A., & Grün, E. 2002, AJ, 123, 2857

Larson, E. J. L., Toon, O. B., & Friedson, A. J. 2014, Icarus, 243, 400

Le Gall, A., Janssen, M. A., Wye, L. C., et al. 2011, Icarus, 213, 608

Lebedinets, V. N., Manochina, A. V., & Shushkova, V. B. 1973, Planet. Space Sci., 21, 1317

Lebonnois, S., Burgalat, J., Rannou, P., & Charnay, B. 2012, Icarus, 218, 707

Lebonnois, S., Hourdin, F., Eymet, V., et al. 2010, Journal of Geophysical Research (Planets), 115, E06006

Lebonnois, S., Toublanc, D., Hourdin, F., & Rannou, P. 2001, Icarus, 152, 384

Lebonnois, S. é., Bakes, E. L. O., & McKay, C. P. 2003, Icarus, 161, 474

Lellouch, E., Gurwell, M. A., Moreno, R., et al. 2019, Nature Astronomy, 3, 614

Letourneur, B., & Coustenis, A. 1993, Planet. Space Sci., 41, 593

Levison, H. F., & Duncan, M. J. 1997, Icarus, 127, 13

Levison, H. F., Duncan, M. J., Dones, L., & Gladman, B. J. 2006a, Icarus, 184, 619

—. 2006b, Icarus, 184, 619

Lewis, J. S. 1971, Icarus, 15, 174

Lin, S.-C. 1954, Journal of Applied Physics, 25, 54

Lin, S.-J. 2004, Monthly Weather Review, 132, 2293

Lindackers, D., Burmeister, M., & Roth, P. 1991, Symposium on Combustion, Vol. 23 (Elsevier), 251–257

Lindal, G. F., Wood, G. E., Hotz, H. B., et al. 1983, Icarus, 53, 348

Lora, J. M., Lunine, J. I., & Russell, J. L. 2015, Icarus, 250, 516

Lorenz, R., Turtle, E., Barnes, J., et al. 2018, Johns Hopkins APL Technical Digest (Applied Physics Laboratory), 34, 374

Lorenz, R. D. 2006, Icarus, 182, 559

Lorenz, R. D., Lemmon, M. T., & Smith, P. H. 2006a, MNRAS, 369, 1683

Lorenz, R. D., Lunine, J. I., Grier, J. A., & Fisher, M. A. 1995, J. Geophys. Res., 100, 26377

Lorenz, R. D., & Radebaugh, J. 2009, Geophys. Res. Lett., 36, L03202

Lorenz, R. D., Smith, P. H., Lemmon, M. T., et al. 1997, Icarus, 127, 173

Lorenz, R. D., Wall, S., Radebaugh, J., et al. 2006b, Science, 312, 724

Lorenz, R. D., Wood, C. A., Lunine, J. I., et al. 2007, Geophys. Res. Lett., 34, L07204

Lorenz, R. D., Stiles, B. W., Aharonson, O., et al. 2013, Icarus, 225, 367

Lorenz, R. D., Leese, M. R., Hathi, B., et al. 2014, Planetary and Space Science, 90, 72

Lorenz, R. D., MacKenzie, S. M., Neish, C. D., et al. 2021, The Planetary Science Journal, 2, 24

Love, S. G., & Brownlee, D. E. 1993, Science, 262, 550

Luz, D., Civeit, T., Courtin, R., et al. 2006, Journal of Geophysical Research: Planets, 111, https://agupubs.onlinelibrary.wiley.com/doi/pdf/10.1029/2005JE002617

Macke, R. J., Consolmagno, G. J., & Britt, D. T. 2011, M&PS, 46, 1842

Magri, C., Ostro, S. J., Scheeres, D. J., et al. 2007, Icarus, 186, 152

Maguire, W. C., Hanel, R. A., Jennings, D. E., Kunde, V. G., & Samuelson, R. E. 1981, Nature, 292, 683

May, E. M., Taylor, J., Komacek, T. D., Line, M. R., & Parmentier, V. 2021, ApJ, 911, L30

McCord, T. B., Hansen, G. B., Buratti, B. J., et al. 2006, Planet. Space Sci., 54, 1524

McCord, T. B., Hayne, P., Combe, J.-P., et al. 2008, Icarus, 194, 212

McKay, C. P., Pollack, J. B., & Courtin, R. 1989, Icarus, 80, 23

—. 1991, Science, 253, 1118

Medhurst, L. J., Garland, N. L., & Nelson, H. 1993, The Journal of Physical Chemistry, 97, 12275

Michalakes, J., Dudhia, J., Gill, D., et al. 2005, in Use of high performance computing in meteorology (World Scientific), 156–168

Molina-Cuberos, G. J., Lammer, H., Stumptner, W., et al. 2001a, Planet. Space Sci., 49, 143

—. 2001b, Planet. Space Sci., 49, 143

Moreno, R., Marten, A., & Hidayat, T. 2005, A&A, 437, 319

Moreno-Ibáñez, M., Silber, E. A., Gritsevich, M., & Trigo-Rodríguez, J. M. 2018, ApJ, 863, 174

Mousis, O., Lunine, J. I., Hayes, A. G., & Hofgartner, J. D. 2016, Icarus, 270, 37

Müller-Wodarg, I. C. F., Yelle, R. V., Mendillo, M., Young, L. A., & Aylward, A. D. 2000, J. Geophys. Res., 105, 20833

Neish, C. D., Somogyi, Á., & Smith, M. A. 2010, Astrobiology, 10, 337

Nesvorný, D., Jenniskens, P., Levison, H. F., et al. 2010, ApJ, 713, 816

Newman, C. E., Lee, C., Lian, Y., Richardson, M. I., & Toigo, A. D. 2011, Icarus, 213, 636

Newman, C. E., Richardson, M. I., & Lian, Y. 2013, in European Planetary Science Congress, EPSC2013–964

Newman, C. E., Richardson, M. I., Lian, Y., & Lee, C. 2016, Icarus, 267, 106

Niemann, H. B., Atreya, S. K., Bauer, S. J., et al. 2002, Space Sci. Rev., 104, 553

—. 2005, Nature, 438, 779

Niemann, H. B., Atreya, S. K., Demick, J. E., et al. 2010, Journal of Geophysical Research (Planets), 115, E12006

Nixon, C., Irwin, P., Sung, K., & Teanby, N. 2021, Trace gases in Titan's Atmosphere with JWST MIRI, JWST Proposal. Cycle 1, ID. #2524

Nixon, C. A., Jennings, D. E., Bézard, B., et al. 2013, ApJ, 776, L14

Nixon, C. A., Achterberg, R. K., Ádámkovics, M., et al. 2016, PASP, 128, 018007

O'Gorman, P. A., & Schneider, T. 2008, Journal of Climate, 21, 3815

Olson, D. W., Doescher, R. L., & Gallmeier, J. 1995, S&T, 89, 92

Orszag, S. A. 1970, Journal of Atmospheric Sciences, 27, 890

—. 1971, Studies in applied mathematics, 50, 293

Ostro, S. J., Scott, R., Nolan, M. C., et al. 2000, Science, 288, 836

Pál, A., Szakáts, R., Kiss, C., et al. 2020, The Astrophysical Journal Supplement Series, 247, 26

Pandya, B. M., & Haider, S. A. 2014, Journal of Geophysical Research (Space Physics), 119, 9228

Pesnell, W. D., & Grebowsky, J. 2000, J. Geophys. Res., 105, 1695

Petit, J. M., Kavelaars, J. J., Gladman, B. J., et al. 2011, AJ, 142, 131

Pollack, J. B., Leovy, C. B., Greiman, P. W., & Mintz, Y. 1981, Journal of the Atmospheric Sciences, 38, 3

Pollack, J. B., Rages, K., Toon, O. B., & Yung, Y. L. 1980, Geophys. Res. Lett., 7, 829

Popova, O., Borovička, J., & Campbell-Brown, M. D. 2019, *Meteoroids: Sources of Meteors on Earth and Beyond* (Cambridge University Press), 9

Popova, O. P., Strelkov, A. S., & Sidneva, S. N. 2004, in 35th COSPAR Scientific Assembly, Vol. 35, 3422

Poppe, A., James, D., & Horányi, M. 2011, Planet. Space Sci., 59, 319

Poppe, A., James, D., Jacobsmeyer, B., & Horányi, M. 2010, Geophys. Res. Lett., 37, L11101

Poppe, A. R. 2016, Icarus, 264, 369

Poppe, A. R., & Horányi, M. 2012, Geophys. Res. Lett., 39, L15104

Poppe, A. R., Lisse, C. M., Piquette, M., et al. 2019, ApJ, 881, L12

Porco, C. C., West, R. A., Squyres, S., et al. 2004a, Space Sci. Rev., 115, 363

—. 2004b, Space Sci. Rev., 115, 363

Radebaugh, J., Lorenz, R. D., Kirk, R. L., et al. 2007, Icarus, 192, 77

Radebaugh, J., Lorenz, R. D., Lunine, J. I., et al. 2008, Icarus, 194, 690

Ramírez, S. I., Coll, P., Buch, A., et al. 2010, Faraday Discussions, 147, 419

Rannou, P., Hourdin, F., & McKay, C. P. 2002, Nature, 418, 853

Rannou, P., Hourdin, F., McKay, C. P., & Luz, D. 2004a, Icarus, 170, 443

—. 2004b, Icarus, 170, 443

Rannou, P., Toledo, D., Lavvas, P., et al. 2016, Icarus, 270, 291

Rao, V. V. 1966, A shock tube study of the high temperature reactions of nitrogen with hydrocarbons (The University of Toronto)

Rao, V. V. 1967, The Canadian Journal of Chemical Engineering, 45, 61

Revelle, D. O. 1976, J. Geophys. Res., 81, 1217

Richardson, M. I., Toigo, A. D., & Newman, C. E. 2007, Journal of Geophysical Research (Planets), 112, E09001

Rodriguez, S., Le Mouélic, S., Sotin, C., et al. 2006, Planetary and Space Science, 54, 1510

Rodriguez, S., Le Mouélic, S., Rannou, P., et al. 2009, Nature, 459, 678

Rodriguez, S., Garcia, A., Lucas, A., et al. 2014, Icarus, 230, 168

Rossow, W. B., & Williams, G. P. 1979, Journal of Atmospheric Sciences, 36, 377

Rothman, L. S., Gordon, I. E., Barbe, A., et al. 2009, J. Quant. Spec. Radiat. Transf., 110, 533

Rubin, D. M., & Hesp, P. A. 2009, Nature Geoscience, 2, 653

Rubin, D. M., & Hunter, R. E. 1987, Science, 237, 276

Ryan, E. L., Sharkey, B. N., & Woodward, C. E. 2017, The Astronomical Journal, 153, 116

Sadourny, R., & Laval, K. 1982, Eos., 63

Sagan, C., & Thompson, W. R. 1984, Icarus, 59, 133

Scattergood, T. W., McKay, C. P., Borucki, W. J., et al. 1989, Icarus, 81, 413

Serigano, J., Nixon, C. A., Cordiner, M. A., et al. 2016, ApJ, 821, L8

Shepard, M. K., Richardson, J., Taylor, P. A., et al. 2017, Icarus, 281, 388

Silber, E. A. 2014, Observational and theoretical investigation of cylindrical line source blast theory using meteors (The University of Western Ontario (Canada))

Silber, E. A., Boslough, M., Hocking, W. K., Gritsevich, M., & Whitaker, R. W. 2018, Advances in Space Research, 62, 489

Silber, E. A., & Brown, P. G. 2014, Journal of Atmospheric and Solar-Terrestrial Physics, 119, 116

Silber, E. A., Hocking, W. K., Niculescu, M. L., Gritsevich, M., & Silber, R. E. 2017, MNRAS, 469, 1869

Sim, C. K., Kim, S. J., Courtin, R., Sohn, M., & Lee, D.-H. 2013, Planet. Space Sci., 88, 93

Skamarock, W. C., Klemp, J. B., Dudhia, J., et al. 2005, A description of the advanced research WRF version 2, Tech. rep., National Center For Atmospheric Research Boulder Co Mesoscale and Microscale ...

Smith, B. A., Soderblom, L., Beebe, R. F., et al. 1981, Science, 212, 163

Smith, B. A., Soderblom, L., Batson, R. M., et al. 1982, Science, 215, 504

Smith, H. T., Mitchell, D. G., Johnson, R. E., & Paranicas, C. P. 2009, Planet. Space Sci., 57, 1538

Smith, P. H. 1980, J. Geophys. Res., 85, 5943

Snowden, D., & Yelle, R. 2014, Icarus, 228, 64

Soderblom, L. A., Kirk, R. L., Lunine, J. I., et al. 2007, Planetary and Space Science, 55, 2025

Somerville, R. C. J., Stone, P. H., Halem, M., et al. 1974, Journal of Atmospheric Sciences, 31, 84

Sotin, C., Jaumann, R., Buratti, B., et al. 2005, Nature, 435, 786

Sotin, C., Lawrence, K. J., Reinhardt, B., et al. 2012, Icarus, 221, 768

Spencer, J. R., Pearl, J. C., Segura, M., et al. 2006, Science, 311, 1401

Spoto, F., Tanga, P., Mignard, F., et al. 2018, Astronomy & astrophysics, 616, A13

Srama, R., Ahrens, T. J., Altobelli, N., et al. 2004, Space Sci. Rev., 114, 465

Srama, R., Kempf, S., Moragas-Klostermeyer, G., et al. 2006, Planet. Space Sci., 54, 967

—. 2011, CEAS Space Journal, 2, 3

Stephan, K., Jaumann, R., Brown, R. H., et al. 2010, Geophys. Res. Lett., 37, L07104

Stern, S. A. 2003, Nature, 424, 639

Stiles, B. W., Kirk, R. L., Lorenz, R. D., et al. 2008, AJ, 135, 1669

Stiles, B. W., Hensley, S., Gim, Y., et al. 2009, Icarus, 202, 584

Stofan, E. R., Elachi, C., Lunine, J. I., et al. 2007, Nature, 445, 61

Stone, P. H., Chow, S., & Quirr, W. J. 1977, Monthly Weather Review, 105, 170

Storrs, A., Weiss, B., Zellner, B., et al. 1999, Icarus, 137, 260

Strobel, D. F. 2008, Icarus, 193, 588

—. 2010, Icarus, 208, 878

Stull, R. B. 1993, Boundary-Layer Meteorology, 62, 21

Suarez, M. J., & Takacs, L. L. 1995, Technical report series on global modeling and data assimilation. volume 5: Documentation of the AIRES/GEOS dynamical core, version 2, Tech. rep., NASA Goddard Space Flight Center, Greenbelt, MD

Szalay, J., Pokornỳ, P., Bale, S., et al. 2020, The Astrophysical Journal Supplement Series, 246, 27

Tiscareno, M. S., Mitchell, C. J., Murray, C. D., et al. 2013, Science, 340, 460

Tokano, T. 2005, Icarus, 173, 222

Tokano, T. 2008, Icarus, 194, 243

Tokano, T. 2010, Aeolian Research, 2, 113

Tokano, T., Ferri, F., Colombatti, G., Mäkinen, T., & Fulchignoni, M. 2006, Journal of Geophysical Research (Planets), 111, E08007

Tokano, T., & Neubauer, F. M. 2002, Icarus, 158, 499

Tokano, T., Neubauer, F. M., Laube, M., & McKay, C. P. 1999, Planet. Space Sci., 47, 493

Tomasko, M. G. 1980, J. Geophys. Res., 85, 5937

Tomasko, M. G., Doose, L., Engel, S., et al. 2008, Planet. Space Sci., 56, 669

Tomasko, M. G., Buchhauser, D., Bushroe, M., et al. 2002, Space Sci. Rev., 104, 469

Tomasko, M. G., Archinal, B., Becker, T., et al. 2005, Nature, 438, 765

Toon, O. B., McKay, C. P., Ackerman, T. P., & Santhanam, K. 1989, J. Geophys. Res., 94, 16287

Toon, O. B., McKay, C. P., Griffith, C. A., & Turco, R. P. 1992, Icarus, 95, 24

Trafton, L. 1981, Reviews of Geophysics and Space Physics, 19, 43

Troen, I. B., & Mahrt, L. 1986, Boundary-Layer Meteorology, 37, 129

Turtle, E. P., Perry, J. E., McEwen, A. S., et al. 2009, Geophys. Res. Lett., 36, L02204

Turtle, E. P., Perry, J. E., Hayes, A. G., et al. 2011, Science, 331, 1414

US Standard Atmosphere. 1976, US standard atmosphere (National Oceanic and Atmospheric Administration)

Vida, D., Brown, P. G., Devillepoix, H. A. R., et al. 2023, Nature Astronomy, 7, 318

Vuitton, V., Yelle, R. V., & McEwan, M. J. 2007, Icarus, 191, 722

Waite, J. H., J., Lewis, W. S., Magee, B. A., et al. 2009, Nature, 460, 487

Waite, J. H., Young, D. T., Cravens, T. E., et al. 2007, Science, 316, 870

Waite, J. H., Lewis, W. S., Kasprzak, W. T., et al. 2004, Space Sci. Rev., 114, 113

Waite, J. H., Combi, M. R., Ip, W.-H., et al. 2006, Science, 311, 1419

Wardenier, J. P., Parmentier, V., Lee, E. K. H., Line, M. R., & Gharib-Nezhad, E. 2021, MNRAS, 506, 1258

West, R. A., Balloch, J., Dumont, P., et al. 2011, Geophysical Research Letters, 38, https://agupubs.onlinelibrary.wiley.com/doi/pdf/10.1029/2011GL046843

Wilson, E. H., & Atreya, S. K. 2004, Journal of Geophysical Research (Planets), 109, E06002

Wood, C. A., Lorenz, R., Kirk, R., et al. 2010, Icarus, 206, 334

Wyngaard, J. C., & Brost, R. A. 1984, Journal of Atmospheric Sciences, 41, 102

Yelle, R. V., Cui, J., & Müller-Wodarg, I. C. F. 2008, Journal of Geophysical Research (Planets), 113, E10003

Young, D. T., Berthelier, J. J., Blanc, M., et al. 2004, Space Sci. Rev., 114, 1

—. 2005, Science, 307, 1262

Young, R. E., & Pollack, J. B. 1977, Journal of Atmospheric Sciences, 34, 1315

Yung, Y. L., Allen, M., & Pinto, J. P. 1984a, ApJS, 55, 465

—. 1984b, ApJS, 55, 465

Zarnecki, J. C., Leese, M. R., Garry, J. R. C., Ghafoor, N., & Hathi, B. 2002, Space Sci. Rev., 104, 593

Zarnecki, J. C., Leese, M. R., Hathi, B., et al. 2005, Nature, 438, 792

Zeldovich, Y. B., & Raizer, Y. P. 2002, Physics of Shock Waves and High-Temperature Hydrodynamic Phenomena. (Dover Publications)

Zucrow, M. J., & Hoffman, J. D. 1976, Gas dynamics. Volume 1 (John Wiley and Sons, Inc.)